Chemical control of single-molecule fluorescence

Kirill Vasilev

UNIVERSITÉ DE STRASBOURG

ECOLE DOCTORALE pcp

ÉCOLE DOCTORALE Physique et Chimie-Physique (ED182)

Institut de Physique et Chimie de Matériaux de Strasbourg

THÈSE présentée par :

Kirill VASILEV

soutenue le : **9 Décembre 2022**

pour obtenir le grade de : **Docteur de l'université de Strasbourg**

Discipline/ Spécialité : Nano-Physique

Chemical control of single-molecule fluorescence

THÈSE dirigée par :

M. SCHULL Guillaume	Directeur de Recherche, IPCMS-CNRS, Université de Strasbourg

RAPPORTEURS :

Mme. BELLEC Amandine	Chargée de Recherche, MPQ-CNRS, Université de Paris
M. ŠVEC Martin	Senior scientist, Institute of Physics, Czech Academy of Sciences

---

AUTRES MEMBRES DU JURY :

M. BORISSOV Andrey	Directeur de Recherche, ISMO-CNRS, Université Paris-Sud
M. CHERIOUX Frédéric	Directeur de Recherche, CNRS, FEMTO-ST
M. HERVIEUX Paul-Antoine	Professeur, IPCMS-CNRS, Université de Strasbourg

Acknowledgements

When I was just starting my academic path 12 years ago, back in Altai State University, I was sure that I want to do research and I was confident that I will get my PhD. Well, many things have happened since then, many plans and dreams have changed. However, here I am.

This PhD was quite a journey. It started in parallel with a few COVID lockdowns and many relatable restrictions, making everyone stressed and annoyed, and ended with a Russian-Ukrainian conflict, that was accompanied by huge stress for me during the 3rd year of PhD. After all of that, finishing the manuscript on time and making a good defense was a pleasant surprise. Good ending, huh.

I am not a big talker (my colleagues would agree), so perhaps my acknowledgements may sound dry. Nevertheless, I am sincerely grateful to everyone mentioned here.

I would like to start by thanking people who kindly agreed to be the jury members during my defense. Thank you to Paul-Antoine Hervieux, Andrey Borissov and Frederic Cherioux for your time and effort, and for the discussion during the defense. Thank you to Martin Svec and Amandine Bellec for taking the additional work to review my manuscript in details and for your remarks and corrections.

I would like to continue by thanking the IPCMS personnel that I was lucky to work with.

Thank you, Guillaume Schull, director of my thesis, for giving me an opportunity to conduct my research in your team and for supervising my work. We may had our misunderstandings, but the journey was fun and the result is here.

Thank you, Fabrice Scheurer, my "second supervisor", for your constant support and assistance, and for keeping the STM cold when I was too lazy to arrive to the lab on time. It was a pleasure to work with you and talk to you, whether it was about physics or wine.

Thank you, Virginie Speisser, for your help with literally everything. You are one of a kind, and STM team is very lucky to have you.

Thank you, Benjamin Doppagne, for teaching me almost everything I know about STM and helping me to become autonomous in the lab.

Thank you, Michelangelo Romeo, for your assistance and explanations for the software and hardware. And additional thank you for your beautiful sense of humor.

Thank you, Herve Bulou and Alex Boeglin, for your help with understanding of the experimental results and for your patience, when I had problems to understand what you

say.

Thank you, my office neighbours, Song Jiang and Alex Fetida. It was fun and cozy to share the office with you. I wish you both the best in your academic endeavours.

Thank you, Katharina Kaiser, for the amount of fun and help that I received from you in this short period of time we were able to work in the same team. I am confident that your career will skyrocket very soon, all the best.

Thank you, Laurent Limot, for those few times we talked in 3 years. But those times were the toughest for me, when I was writing the manuscript. And, probably without knowing, you gave so much support. Thank you for that.

Thank you, Luis Enrique Parra Lopez. It was crazy fun to make .pptx with diplomacy maps, to align the laser in the junction and to make memes. And I am still sorry for the Moire ruined by Nickelback.

Thank you, Tomas Neuman, for your dark humor and your brilliant mind (in that order). I am happy for you in your current position in Prague, and I am sure it will get only better further on.

Thank you, Anna Roslawska, for your help and discussions. When the boss was not there, I always saw you as a second boss, and went to you with questions or looking for an advice. I wish you all the best in Germany, you are a great researcher. And thank you for the coffee vodka, it was gone fast, but it was smooth.

I would also like to thank the team of Stephane Berciaud: Loïc, Joanna, Aditi, Leo, Etienne, Arnaud and, of course, Stephane himself.

Thank you, Catherine Bonnin and Celine Guillet, for your fast and valuable help with all administrative procedures.

Thank you, Emmanuel Sternitzky, Nicolas Beyer, Xavier Ledoux, Arnaud Boulard, Rene Baehr and Halit Sumar for your help and assistance with the electronics, cryogenics, IT and workshop.

Now a bit more personal part.

I would like to thank Jean-Claude Weeber, supervisor of my master internship. Thank you for your support, for always welcoming me, whenever I was in Dijon, and for being an example.

I would like to thank my dear friends, Yuri, Vladimir, Ivan, Mikhail. Our rare interactions always brought joy, I am grateful to you all for being present in my life.

I would like to thank my family. Thank you, mom and dad, for doing everything you could for me. Thank you for letting me go far away from home for my bachelor degree, and much further away for my master and doctor degrees. Thank you, my dear grandparents, for constant support and encouragement. You are the examples for me, both in personal and professional way. Being able to brighten your mood and make you proud is my biggest reward. Thank you all.

Finally, I would like to thank Anastasiia Sheveleva. Thank you for your support and care from the very beginning of my academic path 10 years ago to the day of my defense. Thank you for just always being there for me. You have a bright scientific future, and you will succeed. 143

Contents

Résumé

Le microscope à effet tunnel (STM) est un outil puissant inventé en 1982 par Binnig et Rohrer [1]. En raison de sa résolution sub-nanométrique, le STM a trouvé des applications majeures dans divers domaines de recherche, tels que la physique, la chimie et les sciences des matériaux. Avec le STM, il est possible d'enregistrer des images topographiques détaillées de surfaces, de molécules et d'atomes. Les techniques de spectroscopie à effet tunnel (STS) permettent d'accéder et d'enregistrer la structure électronique de l'échantillon sondé. Le contrôle précis de la pointe STM permet de manipuler des molécules et des atomes uniques. Associé à un dispositif de détection optique, le STM permet d'étudier les propriétés optiques des matériaux à la plus petite échelle grâce à une technique appelée luminescence induite par le STM (STML). Du point de vue de la physique et de la chimie, les expériences STM et STML menées sur des molécules uniques constituent la limite ultime en termes d'analyse chimique. Les études STML de la fluorescence de molécules uniques sont au cœur du présent manuscrit.

La STML a éte utilisée avec succès pour la premiere fois en 2003 par Qiu *et al* pour mettre en évidence la luminescence intrensique d'une molécule unique. Les auteurs ont détecté le spectre optique d'une seule molécule de porphyrine excitée par le courant tunnel, découplée par une couche d'oxyde sur une surface d'aluminium. [2]. Depuis lors, le domaine a connu un développement incroyable. Plusieurs stratégies ont été proposées pour découpler électroniquement les molécules du métal (condition nécessaire àl'observation de luminescence), comme des couches de molécules [3], la suspension de la molécule entre la pointe et l'échantillon [4] jusqu'à ce qu'en 2016 Zhang *et al* introduisent la stratégie la plus pratique de découplage de la molécule du métal en utilisant une couche isolante de NaCl. À ce stade, la haute résolution et l'intensité des spectres enregistrés ainsi que la possibilité de sonder et de contrôler l'environnement local ont ouvert la voie à l'étude par STML de diverses propriétés de molécules uniques, telles que la distribution spatiale des intensités de fluorescence [5, 6], le transfert d'énergie entre molécules uniques [7, 8], l'influence du champ externe sur les propriétés fluorescentes [9, 10], le contrôle des états chargés et de leur fluorescence [11–13] et bien d'autres.

C'est à ce moment-là que les molécules de phtalocyanine sont devenues largement utilisées dans les expériences de STML. Cependant, il y a une certaine limite à ce que l'on peut comprendre à partir d'un système modèle aussi simple. Certains sujets, comme par exemple les mécanismes d'excitation sous-jacents, sont encore débattus à ce jour. Une étude approfondie et fondamentale d'un système plus complexe, tout en restant dans une configuration mono-moléculaire, pourrait améliorer notre compréhension de ces mécan-

ismes. Afin d'atteindre un contrôle systématique de la complexité du système, nous nous appuyons sur les vastes possibilités de la chimie. Le manuscrit présente des expériences de STML réalisées sur des molécules uniques de phtalocyanine dihydrogéne (H_2Pc) et de zinc (ZnPc) chimiquement modifiées. Nous rapportons l'impact de ces changements systématiques (*in situ* et *ex situ*) de la structure moléculaire sur les propriétés électroniques et optiques de ces molécules. Cette étude permet de mieux comprendre l'influence de l'environnement électrostatique, le mécanisme d'excitation d'une molécule unique et les caractéristiques d'émission vibronique des molécules uniques.

Le manuscrit est organisé de la manière suivante

Le **chapitre 1** présente les principes de base du STM et la configuration utilisée dans nos expériences. Nous décrivons le courant tunnel dans la jonction STM, les régimes d'imagerie et la technique de spectroscopie à effet tunnel à balayage (STS). En ce qui concerne l'appareillage, un STM OMICRON sous ultravide à basse température est décrit ainsi que la configuration d'acquisition de la lumière mise en œuvre.

Le **chapitre 2** traite de la génération et de l'émission de lumière dans une jonction STM. Le chapitre commence par une introduction générale des plasmons de surface. Nous décrivons ensuite le cas spécifique d'une jonction STM, où les plasmons de surface sont localisés dans la cavité formée par la pointe et l'échantillon. Les concepts de nano-cavité et de pico-cavité sont introduits. Le chapitre se poursuit en expliquant comment l'émission de lumière par une molécule unique est obtenue avec la pico-cavité et quelles mesures il faut prendre pour découpler suffisamment les molécules des échantillons et des pointes pour obtenir une emission intrinsèque. Le chapitre se termine par une discussion sur les mécanismes d'excitation conduisant à la fluorescence moléculaire dans les expériences STML.

Le **chapitre 3** présente une première série de résultats expérimentaux réalisés sur une série de molécules de H_2Pc modifiées chimiquement *in situ* et adsorbées sur un échantillon NaCl/Ag(111). Tout d'abord, les résultats des tracés temporels de STML, STS et tautomérisation d'une molécule de H_2Pc non modifiée sont présentés. Le chapitre continue avec une description de la procédure utilisée pour enlever un (puis deux) des protons centraux de la molécule H_2Pc. Les sous-espèces moléculaires résultantes (HPc^- pour une molécule simplement déprotonée et Pc^{2-} pour une molécule doublement déprotonée) sont étudiées en détail. L'étude révèle des changements particuliers dans la tautomérisation, les positions des résonances ioniques et le comportement d'émission de lumière qui sont bien reproduits par les calculs. Nous démontrons que les décalages d'énergie observés dans les spectres STML des molécules reflètent l'influence du champ électrique généré par les électrons en excès qui restent dans la molécule après la déprotonation. Le chapitre se termine par des calculs de la signature vibronique des molécules, montrant un bon accord avec les résultats expérimentaux et démontrant que les petits décalages dans l'énergie de certains des modes vibrationnels sont également dus au champ électronique local généré

par l'excès de charge, un phénomène discuté en termes d'effet Stark vibrationnel interne. Les travaux présentés dans ce chapitre ont été publiés dans Nature Comminucations [14].

Le **chapitre 4** présente un modèle multi-électronique décrivant le mécanisme d'excitation dans les expériences STML avec des molécules uniques. Le chapitre commence par souligner les inexactitudes des modèle à une particule, généralement utilisé pour décrire le mécanisme d'excitation, en prenant l'exemple de H_2Pc/NaCl/Ag(111). Le même système est ensuite considéré dans le cadre du modèle multi-électronique et discuté plus en détail pour HPc^- et Pc^{2-}. Ce modèle permet de mieux comprendre les données expérimentales et explique même le comportement STML "sombre" de HPc^-. Le chapitre se termine par l'examen de deux autres exemples tirés de la littérature ZnPc/NaCl/Ag(111) et NaCl/Au(111). Les deux substrats ont des travaux de sortie différents, ce qui entraîne des décalages de leurs énergies de résonance ionique. Notre approche multi-électronique permet d'identifier les différents chemins d'excitation d'injection de porteurs, fournissant une compréhension cohérente et systématique du mécanisme d'excitation dans ce cas également.

Le **chapitre 5** présente une autre série de résultats expérimentaux réalisés sur une série de molécules chimiquement modifiées et adsorbées sur un échantillon NaCl/Ag(111). Elles sont constituées de molécules de ZnPc avec des cycles benzéniques supplémentaires, constituant une série d'espèces intermédiaires entre ZnPc et la naphtalocyanine de zinc (ZnNc). Le chapitre décrit d'abord les expériences STS et STML menées sur chacune des molécules de la série. Une comparaison des résultats démontre que, avec l'ajout de cycles benzéniques, l'écart entre les résonances ioniques dans les spectres $\frac{dI}{dV}$ diminue et l'énergie de fluorescence se déplace vers le rouge. Une étude détaillée des spectres STML permet de séparer les molécules en deux groupes basés sur la symétrie des dipôles moléculaires. La dégénérescence des états excités est levée pour les molécules asymétriques, comme en témoigne l'observation de deux pics excitoniques dans les spectres STML. Le chapitre se poursuit par une description des cartes de fluorescence hyper résolues (HRFM) d'une seule molécule de ZnPc+2 ($D2_h$). Les cartes montrent des distributions spatiales différentes pour les diverses contributions. Le chapitre se termine par une comparaison des spectres vibroniques expérimentaux des deux dipôles de ZnPc+2 ($D2_h$) avec les calculs théoriques. La comparaison donne un très bon accord entre théorie et expérience.

0.1 Microscopie à effet tunnel (STM)

Le courant tunnel dans la jonction STM

Peu après l'invention du STM, Tersoff et Hamann ont établi une équation décrivant le courant tunnel dans une jonction [15, 16]. Les auteurs ont fait quelques approximations, en supposant une température basse et une petite tension de polarisation, mais surtout,

ils ont modélisé la pointe comme une sphère qui se comporte comme une barriére de potentiel localement sphérique lorsqu'elle s'approche de la surface de l'échantillon. Ces approximations ont permis d'établir une expression simplifiée pour le courant tunnel qui permet une bonne comparaison quantitative avec l'expérience :

$$I \propto \int_0^{eV} \rho_s(E)T(E,V,z)\,dE = \int_0^{eV} \rho_s(E)\exp^{(-2z\sqrt{\frac{m}{\hbar^2}(2\Phi_{eff}+eV-2E))}}\,dE. \tag{1}$$

où I est le courant tunnel, T est le coefficient de transmission, $\rho_s(E)$ est la densité locale d'états (LDOS) de l'échantillon à l'énergie E, z est la distance pointe-échantillon, Φ_{eff} est le travail de sortie moyen de la jonction pointe-échantillon et V est la tension appliquée à la jonction.

Spectroscopie à effet tunnel (STS)

La dérivée du courant tunnel I par rapport à la tension V est [17]:

$$\frac{dI}{dV}(V) \propto \rho_s(eV)T(eV,V,z) + \int_0^{eV} \rho_s(E)\frac{dT(E,V,z)}{dV}\,dE. \tag{2}$$

Généralement le second terme peut être négligé, car la trasnmission varie peu avec la tension de polarisation, ce qui conduit à

$$\frac{dI}{dV}(V) \propto \rho_s(eV). \tag{3}$$

Cette équation démontre que la valeur de la conductance différentielle $\frac{dI}{dV}(V)$ est directement proportionnelle à la valeur de la densité locale d'états de l'échantillon sondé. Cette proportionnalité est à la base de la spectroscopie à effet tunnel (STS).

Expérimentalement, l'obtention d'informations sur la LDOS de l'échantillon étudié peut être réalisée de la manière suivante : la boucle de rétroaction étant désactivée, la valeur du courant tunnel I est enregistrée dans une plage sélectionnée de la polarisation pointe-échantillon V. Pour obtenir la partie dérivée dans la mesure expérimentale, la polarisation est modulée par une petite tension sinusoïdale, δV_{mod} à une fréquence donnée pendant de balayage. Une détection synchrone donne accès au terme dérivé et permet de filtrer le signal du bruit.

Microscope à effet tunnel à balayage LT-UHV d'OMICRON et système de collecte et d'analyse de la lumière

Toutes les mesures expérimentales réalisées dans ce manuscrit ont été effectuées avec un STM OMICRON commercial à basse température et ultravide. Le système cryogénique est composé de deux cryostats : le cryostat externe est rempli d'azote liquide (LN_2) et le cryostat interne d'azote liquide ou d'hélium liquide (LHe). La tête du STM est fixée sous

le cryostat d'hélium et en contact thermique avec lui. Cette conception permet au STM d'atteindre les basses températures souhaitées de 4.7K° et de conserver ces conditions pendant une longue période.

Pour pouvoir enregistrer et analyser l'émission de lumière, un système optique de collecte et de détection est mis en place. Une partie du système de collecte est située directement dans la chambre à vide, sur la tête STM, tandis que l'autre partie est située à l'extérieur pour diriger la lumière collectée dans un spectromètre. Le système de collecte est composé de deux lentilles. La première est située directement à l'intérieur du STM pour collecter la lumière à la jonction, la transformer en un faisceau collimaté et l'envoyer à l'extérieur de la chambre. Le faisceau collimaté sortant de la lentille passe par deux fenêtres des écrans thermiques du cryostat, puis par la fenêtre de la chambre à vide. La lumière est ensuite collectée par la lentille de focalisation puis injectée via la fibre dans le spectromètre Acton SP2300 de Princeton Instruments.

0.2 L'émission de lumière induite par les STM (STML)

Les STML dans une jonction métal-métal

L'émission de lumière induite par un courant tunnel a été observée pour la première fois en 1976 par Lambe *et al.* dans une jonction tunnel métal-isolant-métal [18]. Les résultats de l'expérience démontrent que dans une telle jonction, un processus d'émission de lumière a lieu, l'énergie $h\nu$ des photons émis étant inférieure à l'énergie des électrons $|eV|$ avec V la tension de polarization et e la charge de electron. Cette observation, connue sous le nom de coupure quantique, montre que l'énergie des photons est limitée par l'énergie maximale des électrons tunnel. L'énergie transportée et perdue par les électrons tunnel (processus inélastiques) sert à exciter un mode électromagnétique qui induit des oscillations collectives des électrons de conduction, qui se propagent à la surface du métal. Ces ondes de propagation sont connues sous le nom de polaritons plasmoniques de surface (SPP).

Dans la jonction STM, les sources de l'excitation plasmonique sont des électrons inélastiques provenant du processus d'effet tunnel entre un échantillon et une pointe. Dans le cas de l'interface entre un substrat métallique plat et un diélectrique, les SPP possèdent une nature propagative. Cependant, dans le cas d'une pointe de taille nanométrique de ~ 100 nm, la propagation est géométriquement limitée et les SPP sont confinés dans toutes les directions. En raison de ce confinement, ces plasmons sont appelés plasmons de surface localisés (LSP). Par définition, les SPP et les LSP sont différents: les plasmons de surface sont propagatifs et ne peuvent pas se désintégrer radiativement sans compensation de moment, mais ce n'est pas le cas des LSP en raison de leur nature confinée [19]. Les SPP et les LSP s'hybrident, créant ainsi de nouveaux modes hybridés connus sous le

nom de modes plasmons de nano-cavité (NCP). En plus des NCP, nous supposons que le dernier atome de l'apex de la pointe génère une seconde cavité appelée pico-cavité qui contient des modes plasmoniques de pico-cavité (PCP).

Le mécanisme d'excitaion en STML repose sur la combinaison d'électrons inélastiques par effet tunnel et de plasmons de pico-cavité. Cette combinaison peut être exprimée en termes de règle d'or de Fermi : le taux d'émission à la fréquence ν est égal à [20] :

$$\Gamma(\nu) = \frac{2\pi}{\hbar^2}|\langle i|\hat{\mu}|f\rangle|^2\rho_{pcp}(\nu, M), \tag{4}$$

où $\langle i|\hat{\mu}|f\rangle$ est le moment dipolaire de transition associé à la transition inélastique d'un électron de l'état initial $|i\rangle$ à un état final $|f\rangle$ et $\rho_{pcp}(\nu, M)$ est la LDOS disponible à la fréquence ν et à la position M. La première partie de l'équation reflète la contribution du courant tunnel inélastique et la seconde partie décrit la contribution plasmonique.

STML sur une molécule unique

Les toutes premières expériences de STML ont été menées de la manière suivante : les molécules étaient déposées sur une surface métallique en petite quantité, formant ainsi des amas ou des monocouches . Cependant, les spectres optiques observés n'étaient pas caractéristiques d'une luminescence intrinsèque de des molécules, mais ne révélaient que la modification de l'emission plasmonique par la présence des molécules. En fait, lorsque des molécules sont en contact direct avec un métal, l'exciton moléculaire, au lieu de se désexciter en un mode PCP de la pico-cavité, a une voie de désexcitation plus probable par transfert de charge vers le métal en raison d'une forte hybridation des états électroniques. Ce processus est incomparablement plus rapide que la décroissance vers un mode PCP, ce qui réduit fortement la probabilité de l'émission de lumière de la molécule et provoque donc une extinction de la luminescence. Pour éviter cela, la molécule doit être découplée du métal.

Le premier mécanisme d'excitation d'une molécule qui a été proposé est appelé **mécanisme d'injection de porteurs**. [2, 5, 21]. Le mécanisme consiste en une excitation directe de la molécule par une injection séquentielle d'un électron dans l'orbitale moléculaire inoccupée la plus basse (LUMO) et d'un trou dans orbitale moléculaire occupée la plus élevée (HOMO). La formation de cette paire electron-trou (exciton) est ensuite suivie d'une recombinaison et de l'émission d'un photon.

Le deuxième mécanisme est appelé **mécanisme de transfert d'énergie** [4, 22, 23]. Comme pour la STML de la pico-cavité plasmonique, l'excitation moléculaire est générée par un transfert d'énergie à partir d'électrons tunnel inélastiques. Dans ce schéma, l'alignement de l'état HOMO/LUMO avec le niveau de Fermi n'est pas requis. La seule condition est que les électrons portent une énergie suffisamment élevée pour exciter la molécule ($|eV| \geq h\nu$). Si cette condition est satisfaite, l'exciton moléculaire

peut être généré et se désexciter en un mode PCP. Le mécanisme de transfert d'énergie s'applique également au cas de l'excitation d'une molécule parune molécule voisine : [7, 8]. Dans ce cas l'énergie de l'exciton des molécules donneuses et accepteuses doit vérifier $h\nu_{donor} \geq h\nu_{acceptor}$.

0.3 Effet Stark interne de la fluorescence d'une molécule unique

Ce chapitre décrit une expérience d'effet Stark interne réalisée avec des molécules de phtalocyanine H_2Pc déposées sur un échantillon d'argent Ag(111) recouvert de NaCl. Une approche systématique basée sur la déprotonation séquentielle des hydrogènes centraux de la molécule est proposée ici. La déprotonation laisse un électron en excès dans la molécule, qui génère un champ électrique, déplaçant l'énergie d'émission du chromophore. Le chapitre commence par l'étude d'une molécule de H_2Pc. Ensuite, la procédure de déprotonation est mise en œuvre afin d'éliminer successivement les deux protons centraux d'une molécule de H_2Pc. Des images STM et des traces temporelles topographiques sont utilisées pour identifier la nature des espèces déprotonées et leur structure électronique. Les résultats montrent de forts changements dans la dynamique du mouvement de l'hydrogène central (processus connu sous le nom de tautomérisation). Les spectres $\frac{dI}{dV}$ révèlent un déplacement rigide du gap électronique à chaque étape de déprotonation, indiquant (I) la préservation de la structure orbitale π de H_2Pc et (II) un déplacement Stark des états électroniques de la molécule. On montre que pour H_2Pc les composés neutre et déprotonés sont iso-électroniques, contrairement à d'autres expériences de sonde à balayage dans lesquelles charger une molécule modifie profondément ses orbitales π[11, 12, 24–27].

Localisation des charges après déprotonation

Des simulations de théorie de la fonctionnelle de la densité (DFT) ont été réalisées pour les trois espéces (H_2Pc, HPc^- et Pc^{2-}) afin de calculer la structure électronique des orbitales frontières ainsi que leurs représentations iso-surfaciques. Pour la HPc^-, le proton a été artificiellement retiré de l'atome d'hydrogène, tandis que l'électron associé est laissé dans la molécule. Les calculs montrent que l'écart entre les orbitales frontières (π-HOMO et π-LUMO) ne change pas lors de la déprotonation, ce qui signifie que le système d'orbitales π reste essentiellement inchangé. Cependant, la simulation révèle un comportement intéressant pour l'orbitale σ située à 1,7 eV en dessous de la π-HOMO pour la molécule H_2Pc neutre. Cette orbitale subit un déplacement important vers une énergie plus élevée lors de la première déprotonation et un déplacement encore plus important après la deuxième déprotonation. Ces observations confirment que l'électron restant n'est pas situé dans les orbitales π et a une forte influence sur l'énergie de l'orbitale σ.

Les calculs du potentiel électrostatique des molécules généré conjointement par les noyaux et la densité électronique distribuée de l'état fondamental singulet confirment cette hypothèse. Pour le H_2Pc, le potentiel est très proche de zéro, comme attendu pour une molécule neutre. La molécule déprotonée une fois, HPc^-, présente un potentiel négatif beaucoup plus fort dans la molécule, avec un minimum localisé au centre de la molécule, près du site de déprotonation. Lors de la seconde déprotonation, le potentiel négatif devient encore plus fort, s'étendant vers l'extérieur de la molécule.

Propriétés électroniques et de fluorescence de séries de molécules

Les spectres STML enregistrés sur les composés simplement et doublement déprotonés révèlent un déplacement vers le bleu de l'énergie d'émission de fluorescence par rapport au chromophore H_2Pc original. Une comparaison avec les simulations de la théorie fonctionnelle de la densité en fonction du temps (TD-DFT) révèle une dépendance parabolique des énergies d'émission en fonction de la charge intrinsèque de la molécule. La présence d'un terme linéaire non-nul permet d'identifier le rôle joué par la proximité entre un chromophore et une source de champ électrostatique ponctuelle. La procédure de déprotonation affecte également l'émission vibronique de la molécule, en induisant des décalages de fréquence mesurables pour plusieurs modes, un effet qui est discuté en termes d'un effet Stark vibrationnel [28].

Origines possibles du décalage vers le bleu

Plusieurs études ont montré que la pointe STM génère des champs électriques externes statiques et dynamiques qui induisent des décalages des lignes d'émission dus à deux effets connus sous le nom d'effets Stark et Lamb photonique [10, 29–32]. Cependant, les valeurs de ces décalages sont de l'ordre de quelques meV pour H_2Pc, ce qui est un ordre de grandeur inférieur aux décalages observés ici. Dans l'expérience de STML sur HPc^-, la la présence voisine de la molécule de ZnPc peut également provoquer un petit décalage de l'énergie d'émission, comme cela a été montré dans des études précédentes sur le transfert d'énergie entre les molécules simples [8]. Mais de même, ces décalages sont beaucoup plus petits que les décalages observés lors de la déprotonation.

Dans l'expérience, la molécule peut être adsorbée sur l'un ou l'autre des atomes du réseau cristallin de NaCl. La comparaison qualitative des images expérimentales démontre que le site d'adsorption reste le même pour les trois molécules, ce qui permet d'exclure l'influence du site d'adsorption. Les calculs combinés DFT et TD-DFT effectués par nos collaborateurs théoriciens permettent d'exclure l'influence de l'écrantage statique du substrat NaCl, ainsi que les réorganisations structurelles qui se produisent lors de la déprotonation.

Conclusion

Ce chapitre decrit une modification chimique *in situ* de la structure H_2Pc/NaCl/Ag(111). La procédure proposée permet de déprotoner une molécule de H_2Pc de manière contrôlable en préservant simultanément la structure orbitale π de H_2Pc et en laissant un électron σ en excès dans le chromophore. L'énergie d'émission observée dans les spectres STML des molécules subit un décalage vers le bleu non linéaire avec la charge. Les énergies d'absorption correspondantes calculées présentent un bon accord avec les observations expérimentales. L'environnement et d'éventuelles réorganisations structurales ont été exclus comme source possible des décalages en énergie. Les calculs DFT effectués sur une molécule Pc^{2-} relaxée à géométrie fixe donnent une dépendance parabolique avec le nombre de charges supplémentaires localisées en son centre. Le terme quadratique, caractéristique d'un effet Stark dans un champ électrique externe homogène, est accompagné par un terme linéaire. la molécule H_2Pc ne possèdant pas de moment dipolaire permanent, la présence de ce terme linéaire provient de la non-homogénéité du champ électrique généré par les charges supplémentaires localisées au centre de la molécule. Les décalages d'énergie observés sont dus à un effet Stark interne (ISE). La même origine est également mise en évidence et confirmée par des calculs TD-DFT pour certains pics vibratoires.

0.4 Mécanisme d'excitation par STML de molécules uniques

Le chapitre commence par une description du système lorsque la pointe STM est placée au dessus au-dessus de la molécule de H_2Pc, c'est à dire lorsqu'il y a injection de charge dans la molécule. Une première interprétation de l'émission en termes d'injection de porteurs dans le cadre d'une modèle à une particulene permet pas de décrire complètement les données expérimentales. Il faut faire appel à une description multi-électronique. Un tel modèle permet de décrire précisément le transport à travers les résonances ioniques de la molécule, conduisant à la charge moléculaire. Plus important encore, ce modèle explique parfaitement l'excitation de la molécule H_2Pc ainsi que la raison du comportement non-luminescent de HPc^-. Le chapitre se termine par une révision de l'interprétation de deux expériences STML de la literature sur des molécules ZnPc.

Mécanisme d'excitation de H_2Pc et de sa sous-espèce déprotonée

Pour traiter correctement le mécanisme d'excitation, le modèle prend en compte les états moléculaires dans une vision multi-électronique. Dans ce cadre, nous interprétons les pics de $\frac{dI}{dV}$ enregistrés sur la molécule de H_2Pc comme des résonances ioniques positives et négatives (PIR et NIR). Pour la polarisation positive, la résonance est située autour de

0.9 V ; cet état de charge D_0^- est négatif en raison de l'excès d'électron qui passe par effet tunnel de la pointe à la LUMO de la molécule. Pour la polarisation négative, la résonance est située autour de -2.4 V et correspond à un état chargé positivement de la molécule D_0^+. Connaissant l'énergie de l'état excité, S_1=1.81 eV, donné par le spectre optique, la seule voie de neutralisation vers cet état excité est via un état chargé positivement de plus haute énergie (ici D_0^+). Cela explique l'emission lumineuse observée à polarisation négative et l'absence de fluorescence à polarisation positive.

Un modèle multi-électronique de la molécule HPc^- "sombre" montre que ces deux états chargés ont des énergies proches en valeur absolue (-1.5 et 1.8 V). Cependant, les deux états chargés n'ont pas de chemin de neutralisation vers S_1, qui est situé à une énergie plus élevée (1.86 eV) que les états chargés . Cette absence de voie de neutralisation dans l'état excité S_1, maintenant évidente dans ce modèle multi-électronique, explique le comportement "sombre" de HPc^-.

La dernière molécule de la série, Pc^{2-}, a une énergie d'émission $S_1 \rightarrow S_0$ égale à 1.88 eV. L'état chargé positivement est situé à 1.3 eV et ne peut manifestement pas être neutralisé en un état excité de la molécule (d'où l'absence de fluorescence à une polarisation négative). Cependant, l'état chargé négativement est situé à une énergie plus élevée (à 2 eV) que l'état excité de la molécule neutre. Cela conduit à la possibilité d'exciter la molécule par neutralisation de l'état chargé négativement.

Grâce à ce modèle, il est possible de décrire de manière précise les processus d'injection de porteurs qui amènent les molécules dans différents états de charge. Plus important encore, le modèle multi-électronique permet d'identifier les transitions possibles qui conduiront à une décroissance radiative, donc à la fluorescence. Dans le cas de H_2Pc, HPc^- et Pc^{2-} le modèle établi permet de confirmer que, pour que la fluorescence se produise par injection de porteurs, la position relative de l'état excité dans l'échelle d'énergie doit être inférieure à la position des états chargés ($h\nu \leq |E_{resonance}|$). En d'autres termes, l'état excité de la molécule doit pouvoir être atteint par un processus de neutralisation à partir de l'état chargé.

Mécanisme d'excitation de ZnPc

Il est intéressant d'utiliser le même modèle pour expliquer les données de STML obtenues sur différentes molécules et d'aborder l'influence du choix du substrat pour les expériences STML. Pour cela, deux exemples distincts de la littérature sont choisis. L'explication de ces deux résultats dans le cadre de notre modèle multi-électronique fournit un aperçu des processus d'émission chargés et neutres et du rôle du substrat métallique.

Le premier exemple qui est revisité est un travail de Doppagne *et al.* publié en 2018 [11]. Les auteurs présentent des résultats de STML obtenus sur ZnPc/NaCl/Au(111) et les ont interprétés dans le cadre d'un modèle à une particule. Le deuxième exemple que nous avons considéré est un travail de Dolezal *et al.* publié en 2021 [12]. Les auteurs étudient

le transport et la dynamique de fluorescence de molécules de ZnPc neutres et chargées sur le substrat NaCl/Ag(111). Ils proposent également un modèle multi-électronique basé sur un processus à deux électrons : d'abord, une molécule est amenée à un état chargé positivement qui se désintègre ensuite en un état excité d'une molécule neutre. Le deuxième électron amène ensuite cet état neutre excité dans un état chargé excité. Le modèle multi-électronique que nous proposons permet de visualiser et d'indiquer les états impliqués dans le processus STML d'émission neutre et chargée pour les deux exemples.

Conclusion

Une question ouverte laissée dans le chapitre précédent a permis de mieux comprendre le mécanisme d'excitation des molécules uniques dans les expériences de STML. Le modèle multi-électronique présenté ici permet de comprendre les changements dans le comportement d'excitation et de luminescence des molécules déprotonées. De plus, le modèle permet de revisiter différents cas de la littérature et de réinterpréter des caractéristiques de luminescence auparavant déroutantes, pour différents états chargés d'une molécule. L'utilisation de ce modèle multi-électronique permet de visualiser comment les états chargés se déplacent en énergie en fonction du substrat et comment ce déplacement affecte les expériences STML. La réinterprétation réussie de données de la littérature démontre que le modèle proposé peut être facilement appliqué à diverses expériences STML. Ce modèle a été récemment appliqué à d'autres molécules et à des systèmes plus complexes [13, 33, 34].

0.5 Relation entre la symétrie des molécules et l'émission vibronique

Dans le présent chapitre, nous présentons l'étude de molécules déposées à partir d'une poudre de ZnPc modifiée chimiquement *ex situ*. La poudre a été synthétisée par notre collaborateur chimiste Frédéric Cherioux de FEMTO-ST à Besançon. Elle est constituée de molécules de ZnPc avec des anneaux de benzène supplémentaires, ce qui donne une série systématique allant de la ZnPc originale à la ZnPc avec quatre anneaux supplémentaires, également connue sous le nom de zinc naphtalocyanine (ZnNc). La notation de la série est choisie comme étant ZnPc+n, n étant le nombre de cycles benzéniques supplémentaires. Pour l'expérience, les molécules ont été évaporées thermiquement sur le substrat 3ML NaCl/Ag(111). Une étude électronique et de fluorescence approfondie de la série complète de molécules est présentée ici. En prenant le système modèle de ZnPc comme référence, ces résultats montrent des changements dans la structure électronique et les énergies d'émission avec l'addition successive de cycles benzéniques. La levée de la dégénérescence des dipôles moléculaires pour les espèces asymétriques induit de forts changements dans le

spectre optique. Les résultats démontrent qu'avec l'aide de la précision sub-nanométrique du STM, il est possible d'exciter sélectivement un dipôle précis de la molécule, ouvrant la voie à l'étude de l'effet de la position de la pointe sur les spectres d'émission.

Propriétés électroniques et de fluorescence de séries de molécules

La comparaison des résultats expérimentaux montre clairement l'apparition d'anneaux benzéniques supplémentaires pour chaque molécule, la diminution de l'écart en énergie entre les résonances et les changements des énergies d'émission de la lumière dans un décalage rouge. Un phénomène important qui peut être observé est l'apparition d'un second pic d'émission plus élevé en énergie que le pic d'émission principal de la molécule. Il est observé pour les espèces modifiées où les deux axes de la molécule ne sont pas équivalents, à savoir ZnPc+1, ZnPc+2 ($D2_h$) et ZnPc+3. Cette "asymétrie" causée par les cycles benzéniques supplémentaires induit une levée de dégénérescence des états excités de la molécule.

Spectroscopie vibrationnelle de ZnPc+2 (D2h)

Pour étudier la dépendance spatiale des pics vibroniques des molécules "asymétriques", une carte de fluorescence hyper-résolue (HRFM) est enregistrée pour ZnPc+2(D2h)/NaCl/Ag(111). Les intensités normalisées de deux pics principaux, Q_x et Q_y, sont distribuées spatialement de manière différente. Q_x est distribué sur presque toute la molécule avec une diminution progressive vers le centre. Q_y présente un comportement similaire, mais décalé de 90°. L'étude de plusieurs pics vibroniques sélectionés montre des distribution différentes, indiquant une variation spatiale et une sensibilité à la position de la pointe. La comparaison entre les spectres vibroniques enregistrés expérimentalement et ceux calculés théoriquement donne un bon accord. Le spectre STML enregistré sur un axe "court" de la molécule est bien reproduit par les calculs théoriques du seul terme de Franck-Condon (FC) d'un moment dipolaire de transition, tandis que le spectre STML enregistré sur un axe "long" de la molécule est reproduit par les calculs du seul terme de Herzberg-Teller (HT).

Conclusion

Dans ce chapitre, une étude STML d'une série de molécules ZnPc chimiquement modifiées est présentée. Les propriétés électroniques et de fluorescence ont été étudiées pour la molécule de référence ZnPc et pour les molécules modifiées. Les résultats montrent une réduction du gap de $\frac{dI}{dV}$ et un décalage vers le rouge des pics STML avec l'ajout de cycles benzéniques. Une étude de STML approfondie a montré que la rupture de la symétrie de l'axe moléculaire (donc des dipôles moléculaires) permet de lever la dégénérescence des états excités et donc d'observer des contributions indépendantes de Q_x et Q_y. Grâce à la précision sub-nanométrique de la STML, il est possible de sélectionner précisément un

dipôle d'émission sans contribution d'un autre, de Franck-Condon et de Herzberg-Teller de l'émission vibrationnelle. Cette affirmation est étayée par les HRFM enregistrés sur la molécule ZnPc+2 ($D2_h$) et confirmée par des calculs mettant en evidence les différentes contributions.

0.6 Conclusion et perspectives

La motivation au cœur du présent manuscrit était de mieux comprendre les mécanismes qui sous-tendent les expériences STML. Pour ce faire, nous devons aller au-delà des systèmes modèles simples. Nous nous sommes appuyés sur la capacité de la chimie moléculaire à fournir des ensembles de molécules avec des modifications chimiques systématiques. À cette fin, nous avons effectué des modifications de la structure des molécules de phtalocyanine, *in situ* et *ex situ*. Ceci nous permet d'ajuster avec précision leurs propriétés électroniques et optiques.

Dans le chapitre 1, nous avons présenté les principes de base du STM et le dispositif utilisé dans nos expériences.

Dans le chapitre 2, nous avons introduit la génération et l'émission de lumière dans une jonction STM et discuté de la génération et de l'amplification de l'émission de lumière d'une molécule placée dans une pico-cavité. Les mesures à prendre pour découpler suffisamment les molécules des échantillons et des pointes ont été présentées et les explications des mécanismes d'excitation les plus récents ont été décrites.

Dans le chapitre 3, nous avons effectué une déprotonation séquentielle *in situ* des atomes d'hydrogène centraux d'une molécule de phtalocyanine H_2Pc évaporée thermiquement sur le substrat NaCl/Ag(111). Les propriétés électroniques et optiques de la molécule de référence H_2Pc et des espèces déprotonées ont été étudiées. L'excès d'électrons restant dans le centre dela molécule génère un champ électrique hautement localisé et inhomogéne qui influence l'énergie d'émission. L'émission subit un décalage vers le bleu non linéaire avec la charge, un phénomène attribué à l'effet Stark de ce champ électrique interne.

Le chapitre 4 traite du mécanisme d'excitation STML d'une molécule unique. Une tentative d'explication de ce comportement à révélé l'insuffisance du modèle à une particule. L'exemple de HPc^- nous a permis de présenter un modèlemulti-électronique d'une excitation d'une molécule quipermet également de comprendre les changements dans le comportement d'excitation et de luminescence pour des molécules déprotonées. De plus, ce modèle a permis de revisiter différents cas de la littérature et de réinterpréter des caractéristiques luminescentes auparavant déroutantesde de molécules chargées. Notre modèle multi-électronique a permis de réinterpréter les cas de la littérature d'expériences STML sur une molécule de ZnPc sur deux substrats différents (Au(111) et Ag(111)) et de décrire en détail le mécanisme d'excitation.

Le chapitre 5 présente une étude STML d'une série de sous-espèces de ZnPc qui ont été

chimiquement modifiées *ex situ* par l'ajout systématique de cycles benzéniques. Les propriétés électroniques et de fluorescence ont été étudiées pour la molécule de référence ZnPc et chaque sous-espéce. Une étude STML approfondie a démontré un décalage vers le rouge de l'émission des molécules, et donc la réduction du gap optique, avec l'augmentation du nombre de cycles benzéniques. Sur la base de la symétrie des dipôles, les molécules ont été divisées en deux groupes et les résultats des expériences STML ont été comparés plus en détail. Cette comparaison a confirmé que la rupture de symétrie de l'axe moléculaire (donc des dipôles moléculaires) induite par des anneaux de benzène supplémentaires lève la dégénérescence des états excités et génére des contributions indépendantes de Q_x et Q_y. Une carte de fluorescence hyper-résolue (HRFM) a été enregistrée sur une molécule de ZnPc ($D2_h$). La dépendance spatiale des vibrations enregistrées a été expliquée par le couplage des états excités, ce qui est confirmé par les calculs des contributions pures de Franck-Condon et de Herzberg-Teller.

Les résultats présentés dans le manuscrit démontrent les avantages d'un contrôle chimique systématique appliqué à des systèmes modèles. En plus des phénomènes très intéressants en soi, les résultats rapportés ici nous ont aidés à mieux comprendre les mécanismes d'excitation sous-jacents Cependant, certaines expériences seraient intéressantes à realiser sur les molécules modifiées. Par exemple, l'alignement de deux molécules ZnPc+2 ($D2_h$) dans un dimère et le couplage de différents dipôles de la molécule devrait augmenter la luminescence et pourrait révéler de nouvelles caractéristiques vibroniques. La représentation multi-électronique proposée pourrait être encore améliorée en tenant compte des vibrations moléculaires et des réorganisations du substrat et en s'intéressant aux positions exactes des résonances dans le spectre moléculaire $\frac{dI}{dV}$.

Introduction

The scanning tunnelling microscope (STM) is a powerful tool invented in 1982 by Binnig and Rohrer [1]. Due to its extremely high sub-nanometer resolution, the STM has found major applications in various research fields, such as physics, chemistry and materials sciences. With STM it is possible to record detailed topographic images of surfaces, molecules and atoms. Scanning tunneling spectroscopy (STS) techniques allow to access and record the electronic structure of the probed sample. Precise control of the STM tip allows to manipulate single molecules and atoms. Combined with an optical detection setup, STM allows to study the optical properties of materials at the smallest scale with a technique called STM-induced luminescence (STML). From the point of view of physics and chemistry, STS and STML experiments conducted on single molecules constitute the ultimate limit in terms of chemical analysis. STML studies of single molecules fluorescence are at the heart of the current manuscript.

The first time that STML was successfully used to report intrinsic emission from a single molecule was in 2003 by Qiu *et al.*. Here, the authors detected an optical spectrum of a single porphyrin molecule excited by the tunneling current and decoupled by an oxide layer from an aluminium surface. [2]. Since then, the STML field experienced an incredible development. Several strategies were proposed to decouple the molecules from metal, such as layers of molecules [3], suspension of the molecule between the tip and the sample [4] until in 2016 Zhang *et al* introduced the most convenient strategy of decoupling the molecule from metal by using a NaCl insulating layer. At this point, the high resolution and intensity of the recorded spectra together with the ability to probe and control the local environment opened a path for STML investigation of various properties of single molecules, such as spatial distribution of the fluorescence intensities [5, 6], energy transfer between single molecules [7, 8], influence of the external field on fluorescent properties [9, 10], control of the charged states and respective fluorescence [11–13] and many others.

At this point, phthalocyanine molecules became widely-used in STML experiments. However, there is a certain limit to what can be understood from such a simple model system. Some topics, for example, the excitation mechanism underlying STML experiments, are still debated up to date. Thorough and fundamental investigation of a more complex systems, while remaining in a single-molecule configuration, may improve our understanding of this mechanism. In order to reach systematic control over the complexity of the system we rely on the vast capabilities of chemistry. The manuscript presents STML experiments performed on chemically modified free-base (H_2Pc) and zinc (ZnPc)

phthalocyanine single molecules. We report on the impact of $in-situ$ and $ex-situ$ systematic minute changes of the detailed molecular structure on the electronic and the optical properties of these molecules. This study leads to a deeper insight on influence of an electrostatic environment, enhanced understanding of a single-molecule excitation mechanism and vibronic emission features of single molecules.

The manuscript is organized the following way

Chapter 1 presents the basic STM principles and the setup used in our experiments. The covered topics include the description of the tunneling current in STM junction, imaging regimes and scanning tunneling spectroscopy (STS) technique. For the setup, an OMICRON low-temperature ultra-high vacuum STM is described as well as the implemented light acquisition setup.

Chapter 2 discusses light generation and emission in an STM junction. The chapter starts with a general introduction of surface plasmons. The discussion is then shifted to the specific case of an STM junction, where the surface plasmons are localized in the cavity formed by the tip and the sample. Then the concepts of nano-cavity and pico-cavity are introduced. The chapter continues with an explanation of how single-molecule light emission is obtained with the pico-cavity and which measures one need to take to sufficiently decouple molecules from samples and tips. The chapter concludes with a discussion of the excitation mechanisms leading to molecular fluorescence in STML experiments.

Chapter 3 presents a first set of experimental results carried out on a series of $in-situ$ chemically modified H_2Pc molecules adsorbed on a NaCl/Ag(111) sample. First, the results of STML, STS and tautomerization time-traces of an unmodified H_2Pc are presented. The chapter continues with a description of the procedure used to remove one (and later two) of the central protons of the H_2Pc molecule. The resulting molecular subspecies (HPc^- for a singly deprotonated and Pc^{2-} for a doubly deprotonated molecules) are studied in details. The study reveals particular changes in tautomerization, ion resonances positions and light emission behaviour that are well reproduced by calculations. Based on the reported results, we demonstrate that the energy shifts observed in the STML spectra of the molecules reflect the influence of the electric field generated by the excess electrons that are left in the molecule after deprotonation. The chapter concludes with additional calculations of the vibronic signature of the molecules, showing a good agreement with the experimental results and demonstrating that the small shifts in the energy of some of the vibrational modes are also due to the local electronic field generated by the excess charge, a phenomenon discussed in terms of internal vibrational Stark effect. The work presented in this chapter has been published in Nature Comminucations [14].

In **Chapter 4** a many-body model describing the excitation mechanism in STML experiments with single molecules is presented. The chapter begins by pointing out the inaccuracies of the one-particle picture, generally used to describe the excitation mecha-

nism, by taking H_2Pc/NaCl/Ag(111) as an example. The same system is then considered in the framework of the many-body model and discussed further with HPc^- and Pc^{2-}. The many-body picture provide a much better understanding of the experimental data and even explains the "dark" STML behaviour of HPc^-. The chapter concludes by considering two other examples from the literature, where STML on ZnPc/NaCl/Ag(111) and NaCl/Au(111) is reported. The two substrates have different work-functions, which causes shifts of their ion resonance energies. Our many-body approach allows identifying the different carrier injection excitation paths, providing a consistent and systematic understanding of the excitation mechanism in this case too.

The **Chapter 5** presents another set of experimental results carried out on a series of chemically modified molecules adsorbed on a NaCl/Ag(111) sample. The molecular series consists of ZnPc molecules with "additional" benzene rings, constituting a series of intermediate species between ZnPc and zinc naphthalocyanine (ZnNc). The chapter first reports on STS and STML experiments conducted on each of the molecules of the series. A side-by-side comparison of the results demonstrates that, with the "addition" of benzene rings, the gap between the ion resonances in $\frac{dI}{dV}$ spectra decreases and fluorescence energy red shifts. A detailed study of the STML spectra allows to separate the molecules in two groups based on the symmetry of the molecular dipoles. The degeneracy of the excited states of the "asymmetric" molecules is lifted, an effect that is deduced from the observation of the two excitonic peaks in the STML spectra. The chapter continues with a description of hyper resolved fluorescence maps (HRFM) of a single ZnPc+2 ($D2_h$) molecule. The reported map display the different spatial distribution of certain emission peaks. The chapter concludes with a comparison of experimental vibronic spectra of the two dipoles of ZnPc+2 ($D2_h$) with theoretical calculations. The comparison returns a very good agreement.

Chapter 1

Scanning Tunneling Microscopy (STM)

1.1 Working principle

The STM was invented and announced to the world in 1982 by Binnig and Rohrer with their paper [1] where they achieved to image, for the very first time, the topography of the sample surface with at atomic scale.

The scheme of a typical STM is given in Fig.1.1a. The metallic tip is used as a probe to perform the microscopic measurements of a metallic sample. The controls are performed by continuous measurement of the tunneling current, which allows to precisely control the height of the tip with piezoelectric tube in all three dimensions. Due to the naturally small magnitude of the tunneling current (pA), the current needs to be amplified on the way to the controlling part. In Fig.1.1b,c the historically famous STM images are presented, revealing a relief of two complete 7x7 unit cells of Si(111).

The first chapter of the manuscript is dedicated to presentation of the basics of scanning tunneling microscopy, explanation of the scanning tunneling spectroscopy (STS) of a single molecule and the description of an actual STM setup used to conduct the measurements presented later in the manuscript.

1.1.1 Tunneling current

The first basic principle to be understood is the main physical phenomena STM is based on, which is the **tunneling current**. When two metallic electrodes are located in a close proximity ($\sim 1\ nm$) with respect to each other and a voltage bias V is applied between them, there is a probability of the electrons of one of the electrode to travel to another one. Even though, from a classical point of view the potential barrier acts as a forbidden zone for the electrons, from the point of view of quantum mechanics, such system can be pictured as a potential barrier of a height Φ (as in Fig.1.2a). In this case this height is given by the value of a work function of the electrode metal, the value of energy required for the electron to be extracted from this metal. To mathematically describe the tunneling process of an electron through a potential barrier, the following Schrodinger equation is

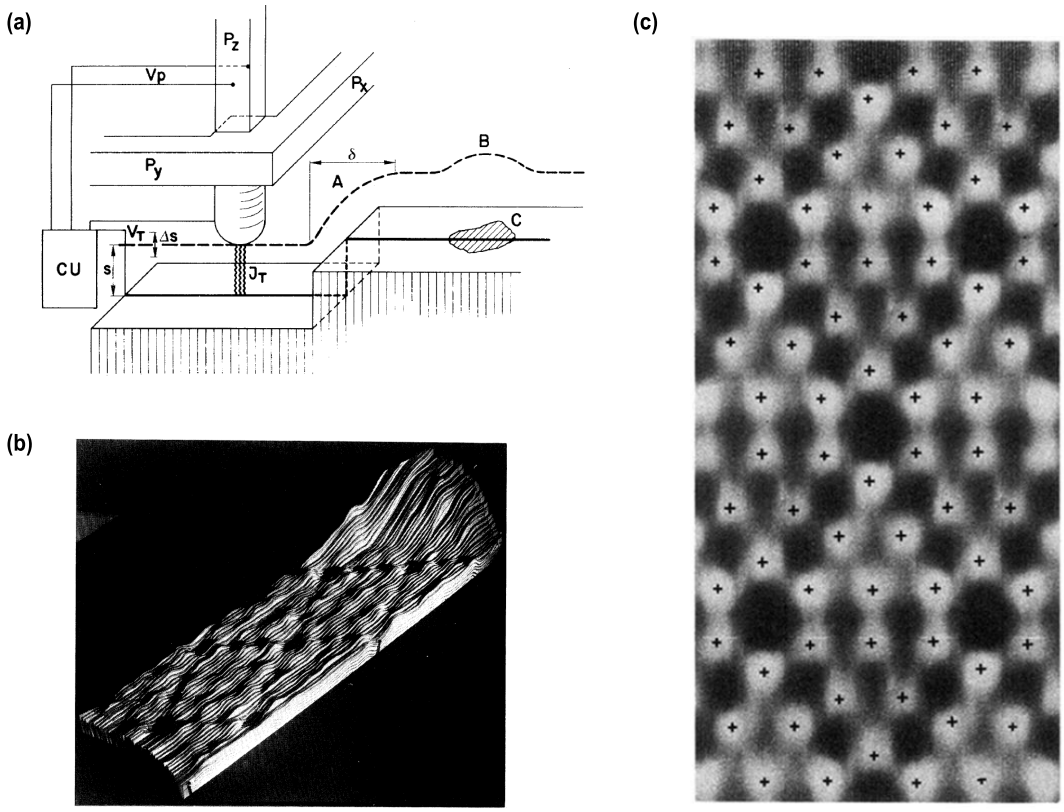

Figure 1.1: **Scanning tunneling microscope (STM). (a)** Scheme of a typical scanning tunneling microscope. The piezodrives P_x and P_y scan the metal tip M over the surface. The control unit (CU) applies the appropriate voltage V_p to the piezodrive P_z for constant tunnel current J_T at constant tunnel voltage V_T. For constant work function, the voltages applied to the piezodrives P_x, P_y, and P_z yield the topography of the surface directly, whereas modulation of the tunnel distance s by Δs gives a measure of the work function. The broken line indicates the z displacement in a y scan at (A) a surface step and (B) a contamination spot, C, with lower work function. Adapted from [1] **(b)** Famous STM image acquired by Binnig and Rohrer in 1983. The image shows the reconstruction of the relief of two complete 7x7 unit cells of Si(111) surface. **(c)** Top view of the relief. Adapted from [35].

used:

$$-\frac{\hbar^2}{2m}\frac{d^2\psi_{el}(z)}{dz^2} + V(z)\psi_{el}(z) - E\psi_{el}(z) = 0, \tag{1.1}$$

where $\hbar$ is the reduced Planck's constant, m is the mass of the electron, E is the energy of the electron, $\psi_{el}(z)$ is the wave function at a given value of a spatial coordinate z and $V(z)$ is the value of the potential barrier at the coordinate z.
In the gap region, where $V = \Phi$ and $E < V$, the solution of the Schrodinger equation is:

$$\psi_{gap}(z) = \psi(0)e^{\pm\kappa z} \tag{1.2}$$

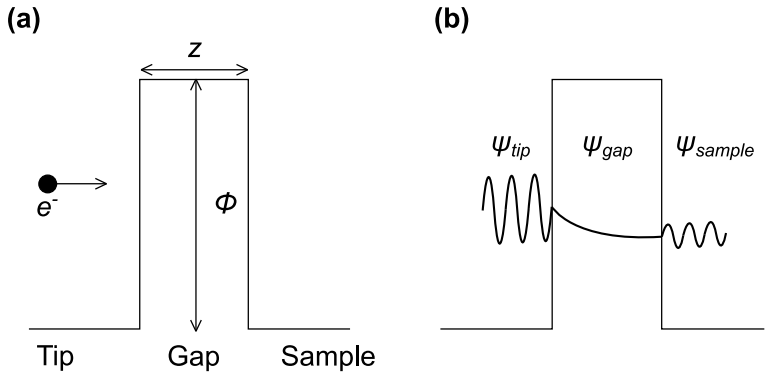

Figure 1.2: **Quantum tunneling phenomena. (a)** Sketch of the potential barrier at the classical limit. The potential barrier of height Φ is created by the gap between two electrodes. The electron e^- with energy $E < \Phi$ is travelling from the tip on the left to the sample on the right but is bounced back (reflected) at the barrier. **(b)** Sketch of the quantum mechanics interpretation where the electron is pictured as a wave.

with

$$\kappa = \sqrt{\frac{2m(\Phi - E)}{\hbar^2}} \tag{1.3}$$

The $\pm$ sign in the exponent comes from the value of $\Phi - E$ based on the applied bias, hence on the directionality of the electron flow.
In this region, the electron behaves as an evanescent wave that exponentially decays with propagation distance, but the probability to find an electron in this region is non-zero. Therefore, the electron can cross the barrier and tunneling process is taking place. This evanescent behaviour is schematically represented in Fig.1.2b. All of the above allows to define the transmission coefficient T of this process as a ratio of the tunneling current at the two sides of the barrier[36]:

$$T \propto \frac{I(z)}{I(0)} = \exp^{-2\kappa z} \tag{1.4}$$

This result demonstrates that even a small variation of the distance between the two electrodes, hence the size of the gap, will drastically influence the transmission. For the Ag(111) that was mostly used during the progress of this PhD, the work function value is approximately 4.74 eV [37]. With an electron of energy $E = 1eV$ the decay constant can be evaluated to be $\kappa = 10^{10}\ m^{-1}$ and the decay length is therefore $l_d = \frac{1}{\kappa} = 1$Å. This value gives the order of magnitude of the distance between two electrodes for the electrons to successfully tunnel. Since the size of a silver atom ($\sim 0.2\ nm$) is larger than the decay length, the tunneling process occurs dominantly between the metallic sample and the last atom of the tip. That fact explains the physical reason behind the extremely high resolution of STM.

1.1.2 Particular case of the tunneling in the STM junction

The tunneling process described in the previous section was presented in a general way of an electron tunneling from one electrode to another while crossing the potential barrier. In the scope of this manuscript, the tunneling process will take place in the nanometer-size gap called the **STM junction** (Fig. 1.3a), where the two electrodes are the sharp metallic tip and the flat metallic crystal, and the potential barrier in between is an ultra high vacuum. As mentioned before, the assumption in this case is that the tunneling process occurs between the crystal and the last single atom of the tip. It comes from the exponential dependence of the transmission on the size of the potential barrier 1.4 and the comparison between the size of a single metallic atom and the decay length.

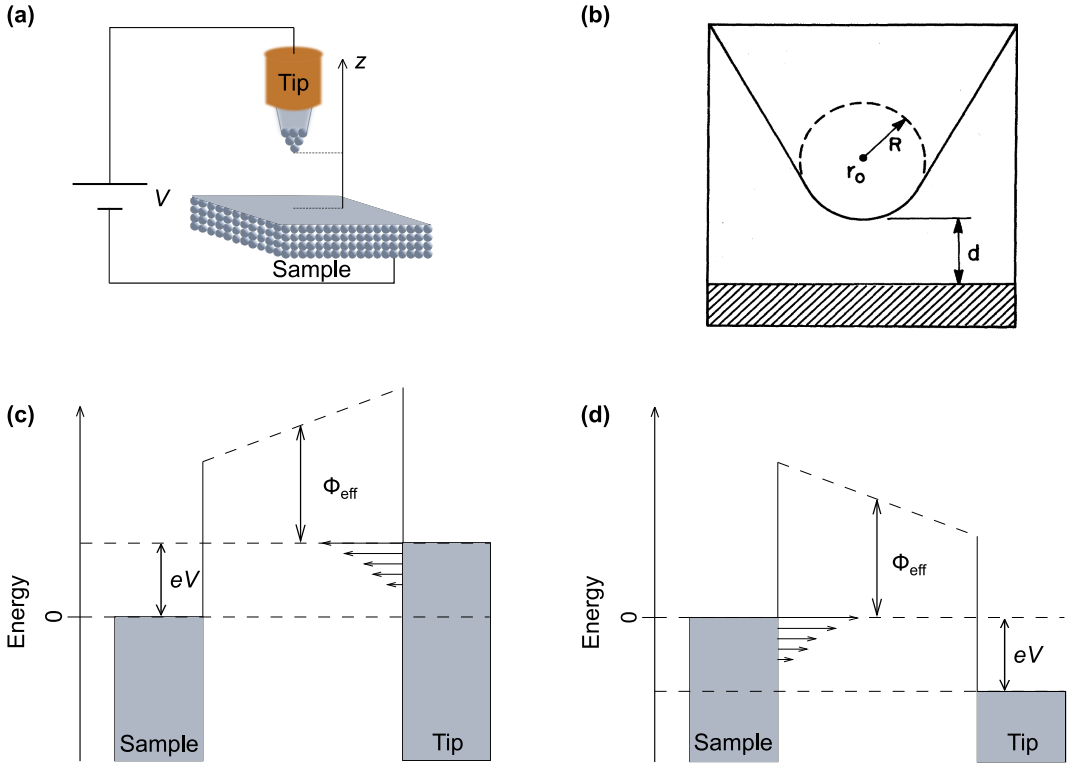

Figure 1.3: **Tunneling in the STM junction. (a)** A sketch of the STM junction. (b) A sketch of the tip geometry proposed by Tersoff and Hamman. The tip is assumed to be a sphere of radius R located at position r_0 at distance d from the sample. Figure adapted from [16] **(c)** A tunneling junction with an applied positive bias $V > 0$ in between the tip and the sample. The reference for a bias is taken with respect to the Fermi level of the sample. Since the Fermi level of the tip in such case is above the Fermi level of the sample, the electron flow direction proceeds from the occupied states of the tip to the unoccupied states of the sample. The trapezoidal potential barrier for the tunneling is depicted as a Φ_{eff}. **(d)** A tunneling junction with an applied negative bias $V < 0$ between the tip and the sample. The tunneling consequently takes place from the occupied states of the sample to unoccupied states of the tip. By convention, the electrical potential V is applied to the sample.

Soon after the STM was invented, Tersoff and Hamann have derived an equation for

the tunneling current in the junction [15, 16]. In this derivation the authors made certain approximations, such as low temperature and small voltage, but most importantly they modeled the tip as a sphere (Fig. 1.3b) that behaves like a locally spherical potential well when approaching the sample surface. This approximation made it possible to derive a simplified expression of the tunneling current that allows for a good quantitative comparison with experiment.

The derivation performed by Tersoff and Haman starts from the work of Bardeen and his expression of the tunneling current [38]:

$$I = \frac{2\pi e}{\hbar} \sum_{t,s} f(E_t)[1 - f(E_s + eV)]|M_{ts}|^2 \delta(E_t - E_s), \tag{1.5}$$

where $f(E)$ is the Fermi-Dirac distribution function, V is the applied voltage, M_{ts} is the tunneling matrix element between states ψ_t of the tip and ψ_s of the sample and $E_{t/s}$ is the energy of the state $\psi_{t/s}$ in the absence of tunneling. The biggest obstacle in this expression is the matrix element M_{ts}. In order to trivialize it, the authors expanded the wave functions of tip ψ_t and sample ψ_s simultaneously applying the spherical tip approximation:

$$\psi_t(r) = C \frac{e^{-\kappa|r-r_0|}}{|r - r_0|}, \tag{1.6}$$

where r_0 is the position of the spherical tip, r is the radius of spherical tip and κ is the decay constant defined in 1.3. Additionally applying a Wentzel-Kramers-Brillouin (WKB) approximation allows to obtain an expression of the tunneling current, which now includes the transmission coefficient T [39]:

$$I \propto \int_{-\infty}^{\infty} \rho_t(E - eV)\rho_s(E)[f_t(E - eV) - f_s(E)]T(E, V, z)\, dE, \tag{1.7}$$

where I is the tunneling current, $\rho_t(E)$ and $\rho_s(E)$ are the **Local Density Of States (LDOS)** of the tip and the sample respectively at the energy E, f_t and f_s are the Fermi-Dirac distribution functions of the electrons of the tip and the sample. The expression 1.7 shows the direct relation of the tunneling current on the LDOS of the tip and the sample. It allows to precise that the STM tip actually interacts with the density of states of the probed surface, rather than with topography.

The term $T(E, V, z)$ in 1.7 is the transmission coefficient for an electron that is dependent on the shape of the tunneling barrier. This dependence is schematically pictured in Fig.1.3(c,d). The sketches depict how the trapezoidal barrier is formed with application of bias in the junction. For such a barrier, the transmission coefficient T can be expressed

in the following way:

$$T(E, eV, z) \propto \exp^{(-2z\sqrt{\frac{m}{\hbar^2}(2\Phi_{eff}+eV-2E))}} \tag{1.8}$$

which is in a good agreement with previously introduced transmission coefficient in 1.4. In this expression, Φ_{eff} is the average work function of the tip-sample junction which represents the average height of the potential barrier of each electrode. Additionally, the presence of the E term in the equation indicates the dependence of the tunneling probability on the energy of the electron. This dependence is schematically indicated in the Fig. 1.3 (c) and (d) with longer directional arrows for the higher energy electrons. The tunneling direction is also given by the potential barrier: when $V > 0$ the electrons leave the occupied states of the tip and tunnel to populate the unoccupied states of the sample. When $V > 0$ the direction is opposite.

Finally, considering the low-temperature experimental conditions where the tunneling takes place through the single last atom of the tip, the density of state of the tip ρ_t can be considered constant and the Fermi-Dirac distribution functions verify $f_t(E-eV)-f_s(E) = 1$ [16]. This approximation gives the final tunneling current expression:

$$I \propto \int_0^{eV} \rho_s(E)T(E, V, z)\, dE = \int_0^{eV} \rho_s(E) \exp^{(-2z\sqrt{\frac{m}{\hbar^2}(2\Phi_{eff}+eV-2E))}}\, dE. \tag{1.9}$$

The above derivation is performed assuming the approximation of the spherical tip with $s-$waves, however it is possible to derive the tunneling current considering different configurations like $p-$ or $d-$waves [36, 40, 41].

1.1.3 STM imaging

In the previous section the role of the control electronics and the piezoelectric tube was introduced. Such system allows to precisely control the relative tip-sample distance and to perform the scanning procedure in two different regimes.
First regime consists of enabling the access of the control unit to the system by closing the respective circuit called the feedback loop. By doing that, the system will automatically react to slight changes of the current and modify the distance between the tip and the sample to keep the current at the constant value. During the scan, if the tip encounter any obstacle such as an atom, a molecule or a step of the substrate, the control unit will adjust the tip height to keep the current constant. Such scanning regime is called a 'constant current' regime. The recorded data in that case would be the value of the tip-sample distance z (Fig. 1.4(b)).

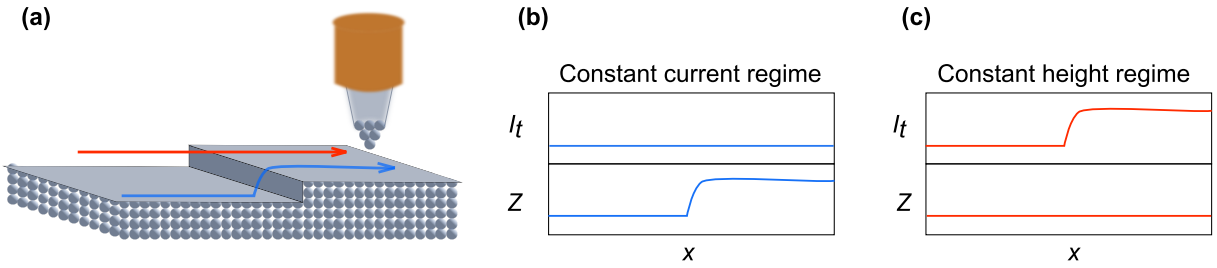

Figure 1.4: **Different scanning regimes. (a)** Sketch of the junction of the scanning tunneling microscope. Blue line represents the constant current regime and the red line represents the constant height regime. **(b)** Scanning in a constant current regime. **(c)** Scanning in a constant height regime.

Second regime is an alternative to the constant current regime. The feedback loop of the control electronics does not adjust the height based on the tunneling current, meaning that the tip height remains constant. The tip is then scanning the surface with this given height. Encountering any variations in topography along the scan will result in a change of the tunneling current based on the distance between the tip and the obstacle. (Fig. 1.4(c)) The topography of the surface is then deduced from such changes of the tunneling current. This regime is called the 'constant height' regime. Since the tip position is fixed, this approach is considered more dangerous for the tip, since encountering any object that is higher than the tip position will result in a crush of the tip.

1.1.4 Scanning tunneling spectroscopy

As one can see from expression (1.9), the value of the tunneling current strongly depends on the local density of states of the sample. This suggests that from the voltage dependency of the tunneling current it is possible to obtain the information on the LDOS of the sample. The derivative of the tunneling current I from expression (1.9) with respect to the voltage V verifies [17]:

$$\frac{dI}{dV}(V) \propto \rho_s(eV)T(eV,V,z) + \int_0^{eV} \rho_s(E)\frac{dT(E,V,z)}{dV}\,dE. \tag{1.10}$$

In case of small values of the voltage V, as well as constant tip height z from the open feedback loop of the STM, the transmission term $\frac{dT(E,V,z)}{dV}$ can be neglected, resulting into

$$\frac{dI}{dV}(V) \propto \rho_s(eV). \tag{1.11}$$

This equation demonstrates that the value of the differential conductance $\frac{dI}{dV}(V)$ is directly proportional to the value of the local density of states of the probed sample. This proportionality is the basis of the **scanning tunneling spectroscopy (STS)**.

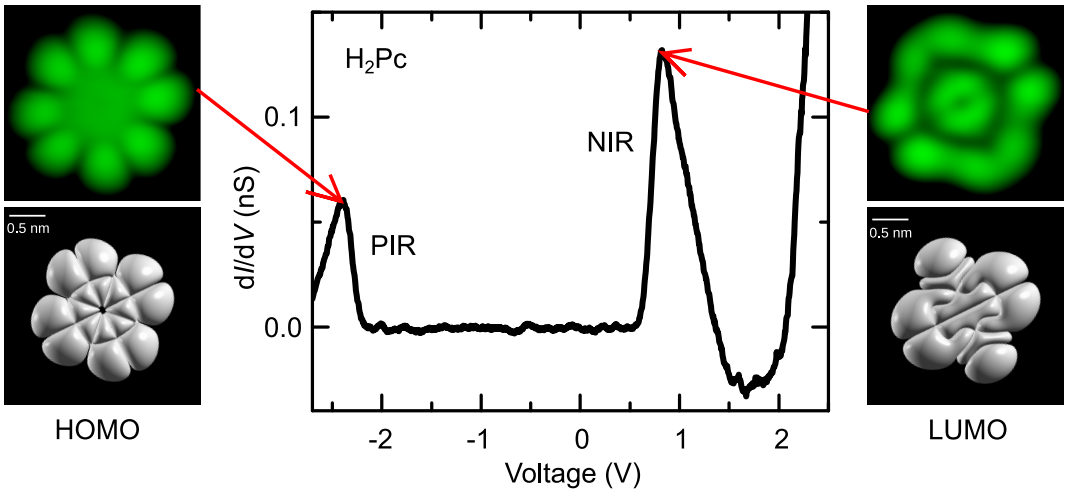

Figure 1.5: **Example of the result of the STS experiment on H_2Pc molecule.** Two peaks in the spectrum represent the positive ion resonance (PIR, left) and the negative ion resonance (NIR, right). On the sides of the plot the STM images acquired at the resonance voltages are presented. Image on the top left is acquired with $V = -2.5$ V and the image on the top right is recorded at $V = 0.5$ V. The resulting images are in a good agreement with the DFT calculations performed on H_2Pc molecule and resemble the HOMO (bottom left) and LUMO (bottom right) respectively.

Experimentally, obtaining the information about the LDOS of the studied sample can be performed in the following way: with the feedback loop turned off, the tunneling current value I is being recorded in a selected range of the tip-sample bias V. To introduce the derivative part into experimental measurement, the bias also experiences a small time-dependent sinusoidal modulation δV_{mod} along the sweep. This modulation is created by the lock-in amplifier at a given frequency. The frequency selection allows to filter out the signal from the noise. The amplitudes of modulation are set to be of the order of few tens of mV, and the modulation frequencies are chosen in a way to avoid the resonance with periodic noise, usually around several hundreds of Hz.
In the Fig. 1.5 a typical $\frac{dI}{dV}$ spectrum of a single free-base phthalocyanine molecule is presented. The two peaks in the spectrum correspond to the charged states of the molecule due to injection/extraction of the electron into/out of the molecule. The process of accessing those charged states of the molecule are known as the **negative ion resonance (NIR)** in case of electron injection and **positive ion resonance (PIR)** in case of electron extraction. A STM image of the molecule recorded with a bias that corresponds to either of the resonances allow to visualise the LDOS of those charged states. The images presented on the sides of the plot in Fig. 1.5 correspond to PIR on the top left and NIR on the top right. They are in a good agreement with DFT calculations of the **highest occupied molecular orbital (HOMO)** (bottom left) and the **lowest unoccupied molecular orbital (LUMO)** (bottom right) of the molecule. This agreement comes from the fact that the charging of the molecule during those particular ion resonance conditions happens by injection or extraction of an electron into LUMO or out of HOMO

respectively.

With STM it is possible to probe the LDOS of the sample not only at a constant position, but also over the area. If the voltage is modulated during the scan, it is possible to record a $\frac{dI}{dV}$ map of the sample. Unlike the scan at constant bias V, when all the states that are present at $\leq V$ are probed, the $\frac{dI}{dV}$ map allows to probe only the states present at $V \pm \delta V_{mod}$. This allows to visualize a specific orbital of the molecule or an interface state of the substrate.

1.2 Experiment details

The following part is dedicated to description of the experimental setup that was used during the PhD. Detailed description of the STM setup is provided. The light collection system is explained part by part with the numerical values for the collection efficiency estimates.

1.2.1 OMICRON LT-UHV scanning tunneling microscope

All the experiment measurements conducted during the course of the PhD and presented in this manuscript were conducted with a commercial low-temperature ultra-high vacuum OMICRON STM. The scheme of the main STM unit with the cryostats and the STM head (the shielded part where the tip and the sample are located) is shown in Fig. 1.6. The cryogenic system consists of two cryostats: the external one is filled with the liquid nitrogen (LN_2) and the internal cryostat with either liquid nitrogen or liquid helium (LHe). The external cryostat is designed to thermally shield the internal one and slow down the boiling and evaporation of the cryogenic liquid inside of the internal cryostat. The STM head is fixed below the cryostats in a thermal contact. Such design allows the STM to reach the desired low temperatures of $4.7°K$ as well as to keep this conditions for a long standing time. If the external cryostat is regularly refilled with LN_2 and temperature is kept constant, the standing time of the STM head at $4.7°K$ can be as long as 27 hours. The evaporation occurs constantly and the resulting He gas is being recovered from the top port to the recovery line to be compressed and reutilised later.
The ultra-high vacuum conditions are reached with a combination of a primary pump (up to 10^{-3} mbar), a turbomolecular pump (up to 10^{-8} mbar) and finally an ionic pump (up to 10^{-11} mbar). The usual working pressure in the scope of the manuscript was below $4*10^{-11}$ mbar. Such high vacuum allows for a very clean working conditions.
When the LT and UHV conditions are met, the STM head can be released from its fixed position and left hanging on the metallic springs. This allows to decouple the STM head from the rest of the chamber and drastically decrease the external vibrations' influence on the experiment. To avoid the oscillations of the released head on the springs, a magnetic

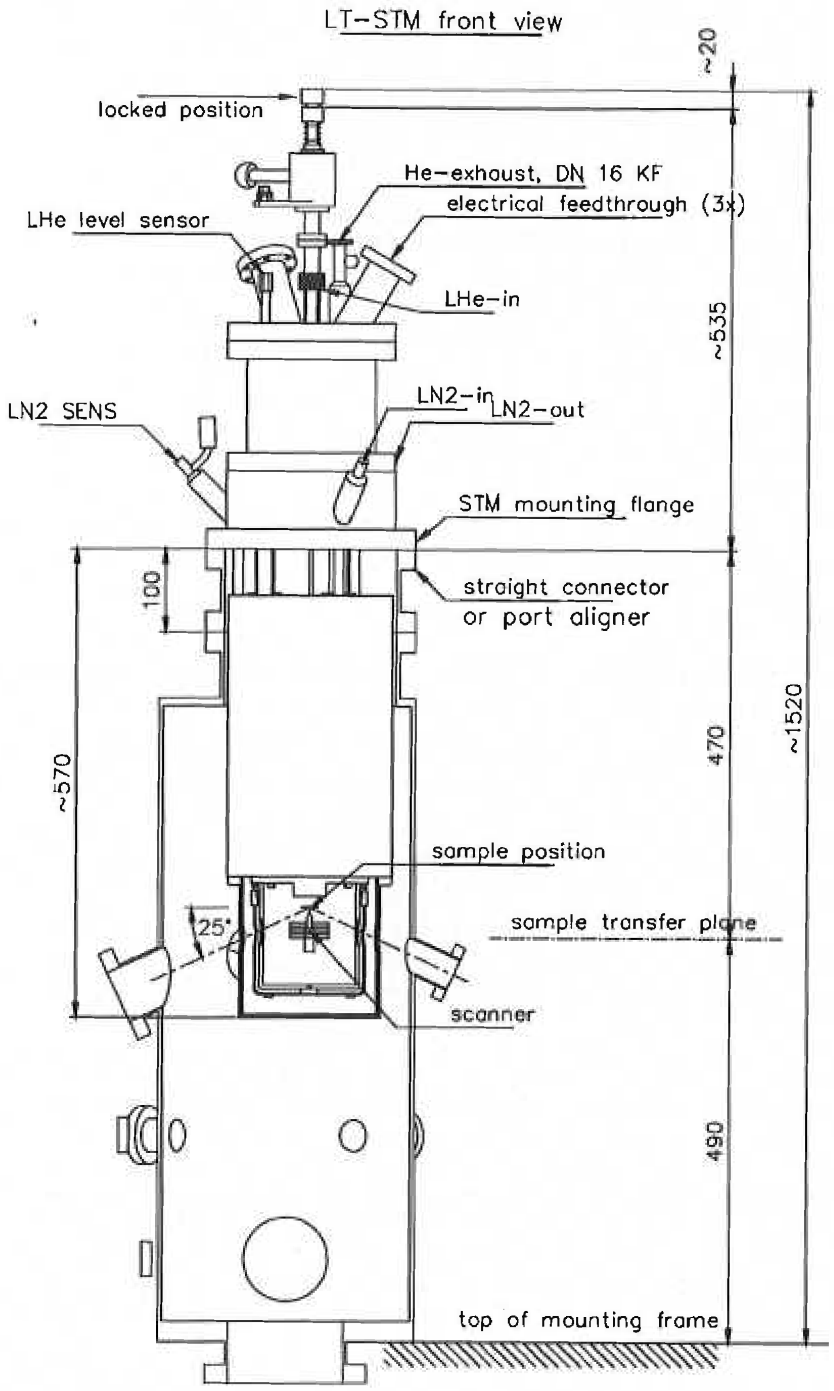

Figure 1.6: **Scheme of an OMICRON LT UHV STM** Sourced from an OMICRON manual.

damping system is used. In a combination with a pneumatic system that supports the whole STM chamber, the noise is brought to its minimum (no more than 10 pm peak-to-peak fluctuations of the z parameter).

1.2.2 Light collecting and analyzing system

The process of light emission of a single molecule happens in a nanometer-size tip-sample STM junction. To be able to record this emission and subsequently analyze it, the collection and detection optical system is implemented in the laboratory. Part of the collecting system is situated directly in the vacuum chamber, inside the STM head, while the other part is located outside to couple the collected light into a spectrometer.
In Fig. 1.7 the sketch of the implemented optical setup is presented. The collecting system consists of two lenses. The first one is directly located inside of STM. The purpose of this lens is to collect the light at the junction, transform it into a collimated beam and to send it outside of the chamber. The lens has the diameter of 9 mm, the numerical apperture $N.A. = 0.287$ and a focal length of $f = 15\ mm$ that aims exactly at the tip apex. The lens is mounted with an angle $\theta = 25°$ with respect to the sample. The reasoning behind the choice of this angle lies in the following points:

1. The amount of the collected light is dictated by the solid angle covered by the lens at a given distance from the junction. The efficiency of the angular collection is estimated to be $\approx 6\%$.

2. The influence of the metallic surface that is expected to impact the angular distribution of the emission. In his thesis [42], Berndt provided theoretical and experimental details indicating that the maximum intensity of a metal junction emission is collected at $\theta = 30°$ with respect to the plane of the metal surface. Such consideration allows to estimate the efficiency of the light collection to be $\approx 10\%$ [43].

3. The design limitations due to the implementation directly into the head of the microscope.

Those factors allow to consider the efficiency of the collection lens inside of the STM, therefore the amount of the total emission that can be collected, to be in the range from 6% to 10% of total emitted light.
Second part of the collection system is located outside of the STM. The collimated beam coming out of the lense passes through two windows of the shields of the cryostat and then through the UHV window of the vacuum chamber. The efficiency of the transmission through the windows is around 90% in the visible and the near-infrared range (400-1000 nm). The light is then being collected by the focusing lens, which in the case of the used setup is an achromatic doublet provided by Thorlabs (AC254-050-B), with a diameter of $d = 25\ mm$ and a focal length of $f = 50\ mm$. The lens is used to focus the light on the input of the fiber bundle that consists of 4 silicate fibers with diameter $d = 200\ \mu m$. The light then travels inside the fiber directly into the spectrometer Acton SP2300 from the Princeton Instruments. The fiber output is positioned directly in front of the spectrometer slit. Upon entering the spectrometer, the light is guided by

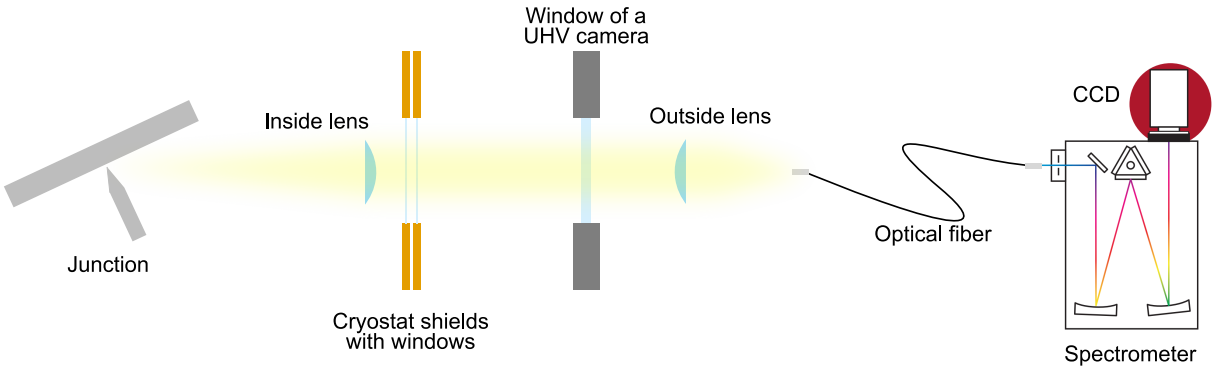

Figure 1.7: **Sketch of an implemented light collection system.** The light emitted at the tip-sample junction is collected by a first lens and directed outside of the vacuum chamber to be collected by the outside lens and coupled into optical fiber. The light is then guided by fiber into the spectrometer. The sketch of the spectrometer is obtained from the Princeton Instruments manual.

mirrors and hits the spectrometer gratings. In the current setup, there is a choice of three different gratings: low-resolution one with 100 grooves per millimeter, medium-resolution with 400 grooves per millimeter and a high-resolution with 1200 grooves per millimeter. The gratings are blazed at 750, 850 and 780 nm respectively and have a focal length of $f = 300\ mm$. Upon landing on the grating of choice, the light is being dispersed and projected on a rectangular CCD sensor of the camera. The transmission and efficiency percentages for the optical elements are provided in Fig.1.8.

The camera used in the setup is a Pylon Excelon 100BR from Princeton Instruments. The CCD consists of 100 columns x 1340 rows of pixels with each pixel being $20x20\ \mu m$ in size. For the spectroscopic measurements, every column is binned to build a spectrum. With a given constant size of a CCD equal to $W = 1340 * 20\ \mu m$ and for a given grating with dispersion d,it is possible to evaluate the range of detected wavelengths:

$$\Delta\Lambda = Wd, \tag{1.12}$$

where d is the dispersion of the grating. The dispersion can be calculated in the following way:

$$d = \frac{1}{f_s r_d}, \tag{1.13}$$

with the focal length of the grating $f_s = 300\ mm$ and the number of grooves per millimeter $r_d = 100/400/1200$. Those equations allow to calculate the effective range for each grating as well as the energy step between two points.

To find out the resolution of the camera, a Ne/Ar lamp was used to generate very narrow emission lines at particular energies. Since the light emitted from the lamp has a very narrow peak width, the resulting spectrum peak widths would be limited by the

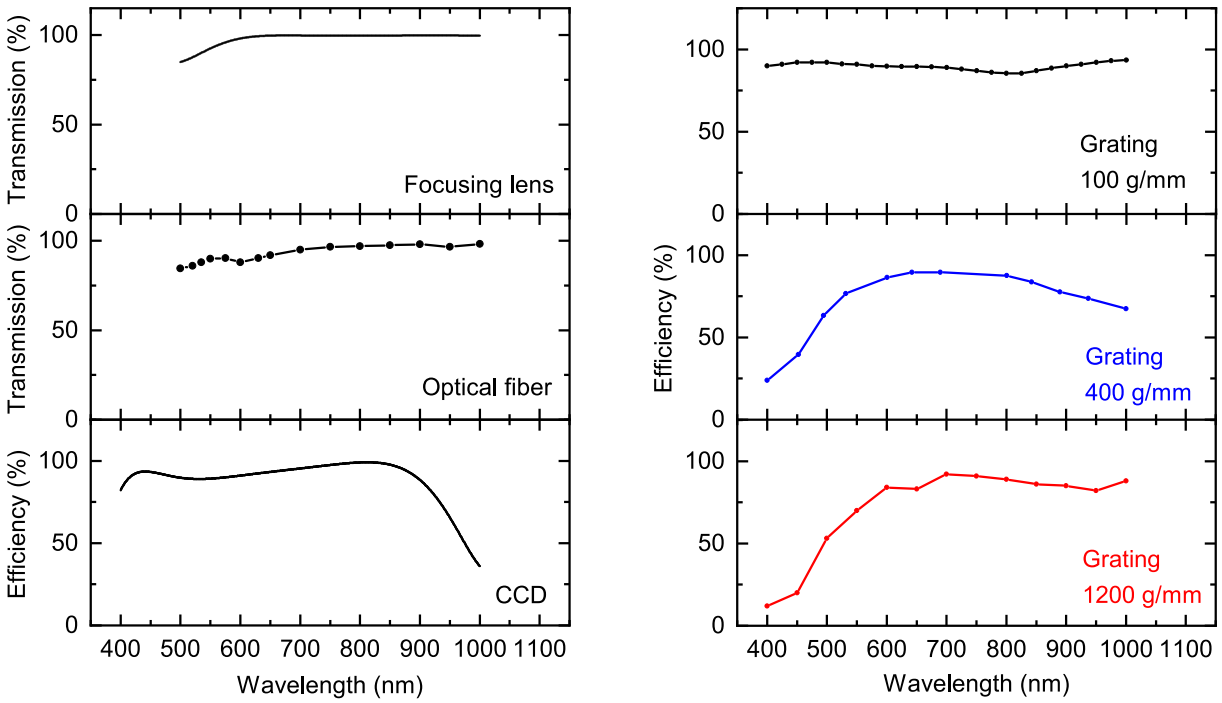

Figure 1.8: **Transmission and efficiency of the optical elements.** Left: transmission percentage for the AC254-050-B focusing lens and optical fiber SEDI ATI 4x200 μm and efficiency of the CCD. Right: efficiency of the three gratings of the spectrometer.

resolution. The Ne/Ar lamp was used to test all three gratings as well as to calibrate the spectrometer, the example of the calibration spectrum is given in Fig.1.9.

The summary of the characteristics of all three gratings is provided in a table 1.1. Based on the values, the use of a 100 grooves per millimeter grating is justified for a large wavelength span with a goal of recording the maximum intensity by sacrificing the resolution. The use of a 400 grooves per millimeter returns a more precise resolution, satisfactory enough to resolve narrow emission lines and vibronic features. The smallest grating of 1200 grooves per millimeter is used for very specific cases, for example to resolve some sensitive feature of the emission like a peak split. The gratings are easily exchangeable between each other during the experiment, which allows for a very rapid and detailed study. Taking into account the whole optical path from the junction to the

Table 1.1: **Numerical values of different gratings' characteristics.** The resolution is calculated at a central wavelength of 650 nm.

Grating	$\Delta\Lambda$ (nm)	$\delta\Lambda$ (nm)	Resolution (nm)	Resolution (meV)
100 g/mm	893	0.67	3	5.7
400 g/mm	223	0.17	0.94	1.4
1200 g/mm	74.5	0.06	0.24	0.38

CCD, the estimated efficiency of the light collection is in the range between 2% to 5% of total light emitted.

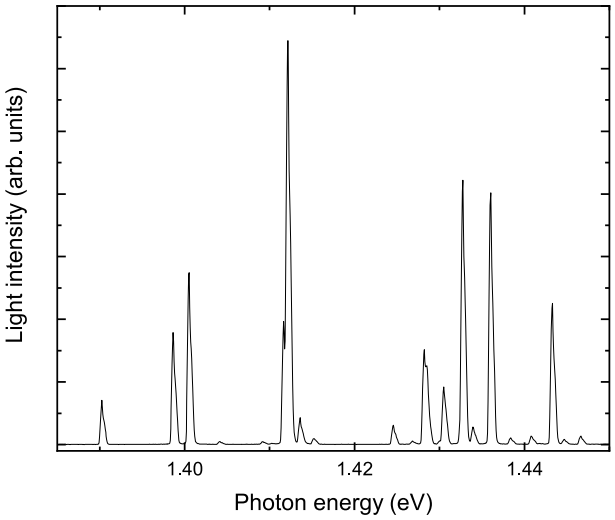

Figure 1.9: **Example of a test spectrum to determine the spectrometer resolution.** The example was acquired with 1200 grooves per millimeter grating using a Ne/Ar lamp as a source of light.

1.2.3 Software and electronics

All the STM manipulations and STM-related data acquisition are performed with the combination of NANONIS software and hardware. It allows for a user-friendly, detailed and precise control of imaging, STS and STML. The recorded data is easily convertable to a more general format that can be used for a further treatment and analysis.
The STML spectrum acquisition is performed with the Lightfield software. Direct connection and recognition of the Princetone Instruments hardware enables a live observation and recording of any light spectroscopy data. For photon-mapping procedure the Lightfield software is being used in a combination with a home-made LabView visual interface developed by the institute engineer Michelangelo Romeo.
For the post-treatment of all the spectroscopy data both Matlab and Origin are used on a regular basis, with some certain conversion calculations performed by home-made Python codes.
The treatment of the STM images is performed with the WSXM software [44], that was designed specifically to process the results of SPM imaging.

1.2.4 Tip preparation

The preparation of the tip for the STM experiments relies on an electrochemical etching approach. The mechanism of this etching process is the following: both the anode (metallic wire that would be etched to obtain the tip) and the cathode (a metallic ring, preferably of the same metal) are immersed into an electrolyte solution. The cathode is being shaped into a ring around the anode for a more uniform etching process, leading to a more symmetrical tip as the result, which might be a crucial point for some STML

experiments. The power supply is then turned on to begin the etching process. The anode is being dissolved at the solution-air interface, where a meniscus forms. At the same time, the cathode ring is covered by the metal of anode. As the process continues, the meniscus of the anode becomes thinner. At some point it is too thin to hold the weight of the immersed part. At that moment, the lower end of the anode falls off, simultaneously stretching the resulting apex of the anode. The etching process is manually or automatically stopped at that point and the resulting tip is removed from the electrolyte solution. The tip is then cut at a preferable size, rinsed with ethanol to remove the leftovers of the etching process and placed into a tip-holders compatible with the OMICRON STM. Any residuals that are not cleaned might affect the imaging and the plasmonic properties of the tip.

In the scope of the PhD, two types of metallic tips were used. First ones were tungsten tips, very convenient in terms of electroetching and highly durable in terms of STM experiments. Even though tungsten does not have a plasmonic response by itself, its stiffness makes it possible to cover the apex of the tip with the metal from the silver Ag(111) or gold Au(111) substrate, resulting into a stable and intense plasmonic response. The solution used to etch tungsten tips is 2M (molar concentration) sodium hydroxide (NaOH), a concentration that is not too strong to ensure that the etching is not too "aggressive" for the tip.

Second metal used during the experiments was silver. It was chosen due to the high intensity of plasmonic response as well as the very convenient fit to the emission energies of the phthalocyanine molecules. The drawback of such tips lies in the high softness of silver, meaning that even a small crush of the tip with the sample bears a high risk of losing the sharp apex. The etching was performed using the 8M ammonium nitrate NH_4NO_3 solution as an electrolyte and on a slightly more complicated etching setup. Due to the more aggressive nature of the interaction between the electrolyte and silver, a manual opening of the circuit is not enough to stop the etching process on time. To avoid that, a three electrodes etching system is implemented, with the third electrode being a reference electrode. The control with respect to the reference electrode was performed using a potentiostat, and an automatic cut-off was performed with an electric circuit that was designed and mounted by an electrician of the institute Emmanuel Sternitzky and a ARDUINO-based controller programmed by the engineer of the institute Michelangelo Romeo.

1.2.5 Crystal preparation

The preparation of the crystal, which in the context of this manuscript means cleaning and flattening of the surface of the metal, is performed inside of the preparation chamber.

The cleaning is performed in repeated cycle of sputtering, which is a bombardment of the surface by Ar^+ ions with the use of the ion gun, and annealing, which is heating the sample up to temperatures high enough that the damaged bombarded surface reconstructs into flat areas.
The only metallic crystal used during the PhD experimental time is a silver crystal, further noted as Ag(111). To clean it in between the two consecutive experiments, at least three cycles of sputtering/annealing were performed each time. The sputtering duration was adjusted each time depending on the status of the crystal, the annealing was always performed to the temperatures $\approx 600K$. Such preparation allows to get a clean surface of the crystal and have large flat areas between the crystalline steps for a more convenient work.

1.2.6 NaCl and molecule evaporation

The preparation of the sample for the experiment takes place in-situ, under the ultra-high vacuum conditions. It takes place in two steps: deposition and formation of the decoupling layer (NaCl in the scope of the current thesis) and subsequent deposition of the molecules of interest.
The deposition of NaCl takes place at room temperature in the preparation chamber. The salt is introduced into small quartz crucibles which are then inserted into a Knudsen cell evaporator. Controllable evaporation process is performed by increase of the current that passes through a filament wrapped around the quartz crucible. The process is controlled with the use of a quartz balance, which provides a sub-monolayer precision of a deposition rate. Once the conditions for evaporation are reached, the quartz balance is moved away and the evaporator output is open to the preparation chamber.
The thickness of the decoupling layer is an important point in STML experiment. The usual STML experiments are performed with the decoupling layer of NaCl being between 3 to 4 monolayers (ML). Such thickness is known to be sufficient to decouple the molecule from the metal and allow for a long enough life time of molecular excited state. Thickness of NaCl larger than 4 ML induces unstable experimental conditions. Depending on the sample metal, the initial growth of NaCl happens in a form of a crystalline islands of height corresponding to 1 or 2 single molecular layers, however it is possible to increase this height by thermal annealing of the sample.
The subsequent deposition of single molecules on the sample is performed with the similar Knudsen cell evaporators inside the vacuum chamber of STM at low temperature. The low temperature conditions are chosen in order to ensure that the isolated molecules adsorbed on the surface will not diffuse.

Chapter 2

STM-induced light emission (STML)

2.1 Basics of STML

2.1.1 STML in a metal-metal junction

In the first part of this section we will address the mechanism leading to an emission of light in a metal-metal junction. First time the light emission induced by tunneling current was observed in 1976 by Lambe *et al.* in a metal-insulator-metal tunneling junction [18]. The results of the experiment demonstrate that in such junction, a light emission process takes place with the energy of emitted photons being lower than the energy of the tunneling electrons at a given bias $h\nu < eV$. This observation, known as a quantum cut-off, shows that the photon energy is limited by the maximum energy of tunneling electrons, hence the emission occurs due to tunneling electrons. The energy carried by the electrons excites an electromagnetic mode that sequentially decays into far-field by a photon emission.

The similar behaviour was later observed in the STM junction [45]. While in the experiment of Lambe the insulating layer between electrodes was a layer of aluminium oxide, in the general case of STM-induced light emission the role of insulator is played by the vacuum between the tip and the sample.The energy diagram of STM junction, where this process takes place, is given in Fig. 2.1a. In Fig. 2.1b the typical STML spectrum is presented. The emitted light is observed in the range of the energies of the electrons and is almost abruptly cut at $V \approx 2.25$V - an energy cut off.

Further investigations of the STML of metal-metal junction were conducted by Berndt *et al.* [46]. The adaptation of the results is provided in Fig.2.1c. Authors conducted an STML experiment on different metallic substrates (silver Ag(111), gold Au(110) and copper Cu(111)) using a tungsten tip in order to observe the difference in optical response. From the acquired spectra it can be seen that the maximum of the emission peak is shifted for different substrates: around 550 nm for silver, 600 nm for gold and 650 nm for copper. The results of Berndt *et al.* demonstrate that the STML of the metal-metal junction depends on the substrate metal.

One more investigation of STML of metal-metal junction was conducted in 2002 by Meguro *et al.*. The adaptation of the results is provided in Fig.2.1d. In their work, the authors report the experimental results on the study of the tip shape dependence on STML. For that, they use two different gold tips that were preliminarily characterized

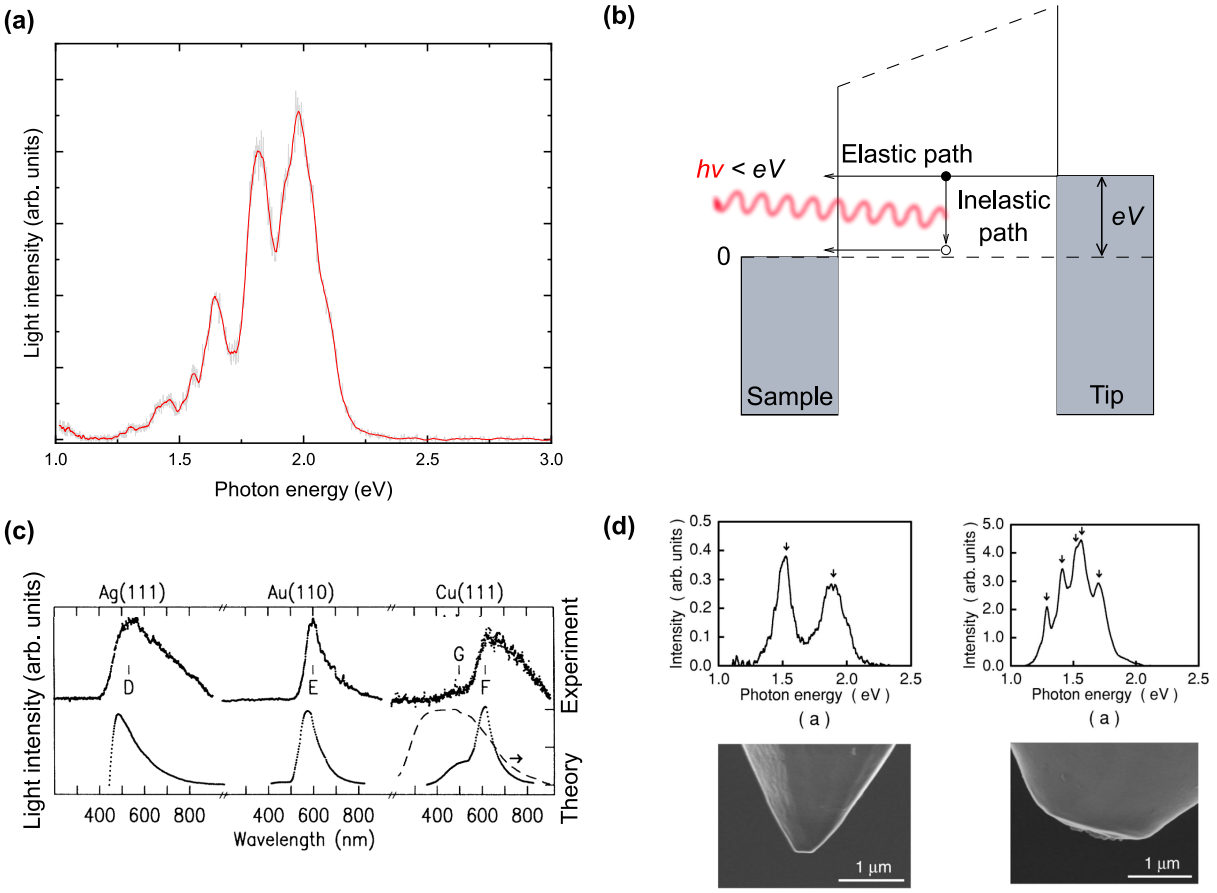

Figure 2.1: **Light emission process in the STM junction.** **a** Typical STML spectrum of a gold tip and silver Ag(111) STM junction. The spectrum of the tunneling current was recorded at $I_t = 1$ nA and tip-sample bias $V = 2.5$ V. **b** Energy diagram of an STM junction illustrating a light emission process caused by inelastic tunneling electrons. **c** Several examples of STML induced by the tungsten tip on different metallic substrates. Metals of the substrate left to right: silver Ag(111), gold Au(110) and copper Cu(111). Top row shows the experimental results of the STML process, bottom row demonstrates the theoretical calculations for the same metals. Adapted from [46]. **d** Results of experiment demonstrating the tip shape dependence of the STML. Top row: STML spectra recorded for different gold tips. Bottom row: scanning electron microscope images of the respective tips. Adapted from [47]

with scanning electron microscope. The recorded emission reveal completely different spectra for the two tips, indicating a strong shape dependence of STML on the tip shape.

The above investigations allow to conclude that emission strongly depends on the material and the geometry of the STM junction. To further understand the physics behind this dependence, the electromagnetic description of the junction should be derived.

2.1.2 Plasmons in a metal-dielectric interface

Previously it was mentioned that the inelastic tunneling electrons excite an electromagnetic mode in the junction. When this mode is excited, it induces the collective oscillations

of the conduction electrons that consequently give rise to plasma waves. These oscillations

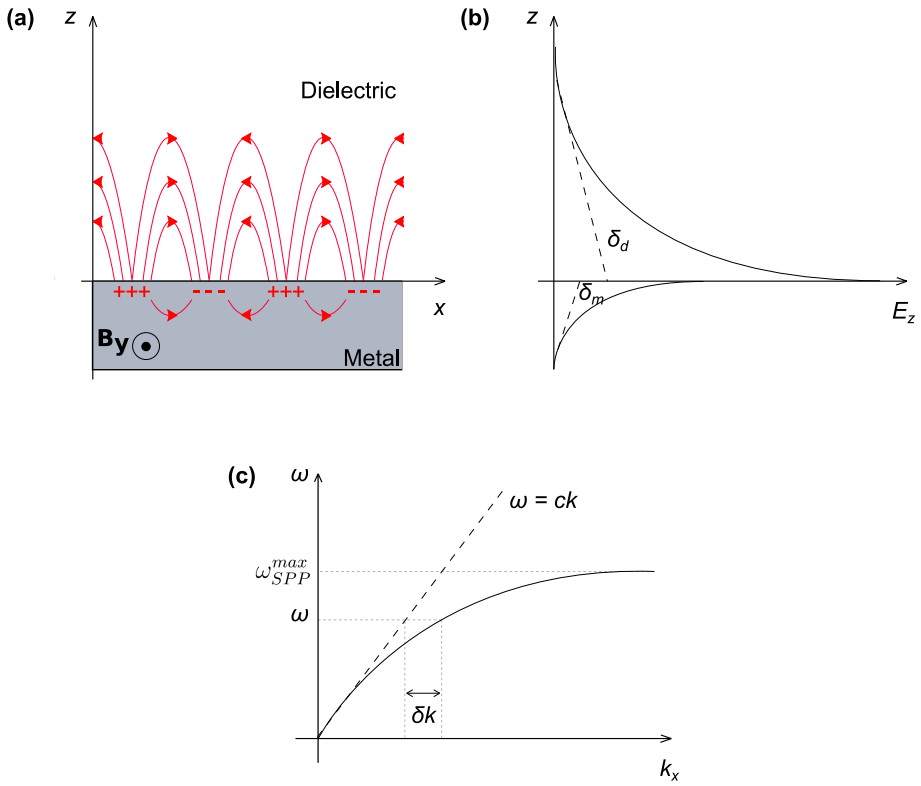

Figure 2.2: **Description of surface plasmons. a** Schematic representation of surface plasmons at the interface between dielectric and metal. Red arrows indicate the electric field. **b** Evanescence of the electric field with respect to the interface. δ_d and δ_m are the decay lengths for the vacuum and the metal respectively. **c** Dispersion relation of the surface plasmon polaritons (solid) and of a free propagating electromagnetic field (dashed). δk is a mismatch between the dispersions at a given frequency ω.

can propagate along the surface of the metal with an oscillation frequency given by the solution of the Maxwell equations:

$$\omega_p = \sqrt{\frac{ne^2}{\epsilon_0 m}}, \tag{2.1}$$

where where n is the density of free electrons in metal, e is the charge of the electron, m is the mass of the electron and ϵ_0 is the permittivity of the free space.
Due to the skin effect, these oscillations cannot propagate deep into the metal. The limitations are given by the skin depth parameter that will depend on the incident field and the properties of the metal in a following fashion:

$$\delta_{skin} = \sqrt{\frac{2}{\omega \mu_0 \mu_m \sigma}}, \tag{2.2}$$

where ω is the frequency of the conduction electrons oscillations, μ_0 the magnetic permeability of the free space, μ_m the relative metal permeability and σ the conductivity of the

metal. The fact that the propagation into metal is limited indicates that the plasmons are mostly localized at the interface between a metal and a dielectric. In such a case, the solutions of the Maxwell equations are known as **surface plasmons**. A schematic description of surface plasmons is given in Fig.2.2a. Upon excitation the electromagnetic field, the surface plasmons in return generate an electromagnetic field (red arrows). That field is evanescent in both metal and dielectric media in direction perpendicular to the interface, as shown in Fig.2.2b. The combination of the oscillations of the conduction electrons in the metal and generated electromagnetic field in the interface is a physical phenomena known as **surface plasmon polaritons (SPPs)**. They represent surface waves propagating along the interface between metal and dielectric.

The dispersion relation of SPPs can be obtained from the solution of Maxwell equations [19, 48]:

$$k_x = \frac{\omega}{c}\sqrt{\frac{\epsilon_d \epsilon_m}{\epsilon_d + \epsilon_m}}, \tag{2.3}$$

where $\epsilon_{m/d}$ is the permittivity of the metal/dielectric. This dispersion relation is plotted in Fig.2.2c as a solid line. The dashed line in the same figure represents the dispersion for a free propagating electromagnetic field. One can see that, in contrast with the free propagating field, the range of the SPPs frequency is limited by the dispersion relation. The maximum frequency of the SPP is given by:

$$\omega_{SPP}^{max} = \frac{\omega_p}{\sqrt{1+\epsilon_d}}, \tag{2.4}$$

One more important conclusion from the dispersion relation plot is the difference between the dispersions of SPPs and photons. For a given frequency, the plasmon has a larger momentum than a free space photon with a mismatch δk. This mismatch demonstrates that SPPs are non-radiative by nature and excitation of SPPs results only into propagation along the interface. If δk compensated, the energy of SPP can be converted into a far-field photon. It can be achieved by the implementation of a prism or a grating, or by irregularities or roughnesses of the surface. [49, 50]

2.1.3 Plasmonic cavity in STM junction

Confinement in a nano-cavity

Previous discussion was based on a metal-insulator interface, where SPPs were excited by an electromagnetic field. In STM junction, the sources of the plasmon excitation are inelastic electrons from the tunneling process between a sample and a tip. In case of the interface between a flat metallic substrate and a dielectric, SPPs possess a propagative nature. However, in case of a ~ 100 nanometer-size tip the propagation is geometrically

limited and SPPs are confined in all directions (as in Fig.2.3a). Due to this confinement, such plasmons are called **localized surface plasmons (LSPs)**. By definition, SPPs and LSPs are different: the surface plasmons are propagative and cannot radiatively decay without momentum compensation, however, it is not the case for LSPs due to their confined nature [19]. Tips made of noble metals, such as silver or gold, are known to provide a strong resonance in the visible wavelength range [51]. For a given metal, the modes of LSPs are defined by the geometry of the tip.

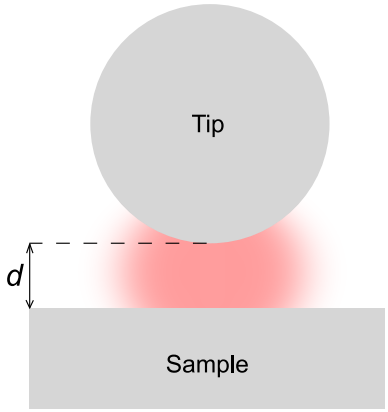

Figure 2.3: **Description of surface plasmons confined in tip-sample junction.** A sketch depicting a STM tip as a $\sim$ 100 nanometer-size sphere. The plasmons excited in such a system are confined in the junction, also called a nano-cavity. The respective modes are called nano-cavity plasmon modes (NCPs).

From electromagnetic point of view, due to the spatial size of the tip, STM junction can be modeled as a nanoparticle-on-mirror. In such a case, as reported in [52, 53], the SPPs and LSPs hybridize thus creating new modes. The hybridized modes of such confined nanometer-size geometry are known as **nano-cavity plasmon modes (NCPs)**.

Enhancement in a pico-cavity

Description of NCP was based on approximation of the tip as a $\sim$ 100 nm size sphere. By convention, the nano-cavity plasmonic structures can confine a volume of electromagntic field of the order of 10 nm^3 [54]. However, the real structure of the tip is much different and the atomic features of the tip apex were not considered in this approximation. Plasmonic confinement to atomic scales were predicted theoretically in 2015 by Barbry *et al.* [55]. Next year, in 2016 the predictions were confirmed experimentally by Benz *et al.* [56]. In their work, the authors investigate the influence of tiny atomic features formed in an interface between a gold nanoparticle and a gold film. It was shown that such features induce a highly localized plasmonic field, which strongly affect the Raman spectrum of a single molecule located inside the cavity. In Fig.2.4(a) the theoretical simulation used by the authors is presented. The top panel shows the near-field map calculated for a gold nanoparticle in front of a gold film. The presence of atomic protrusions of

a nanoparticle highly increases the electromagnetic field density in close proximity. In Fig.2.4(b) a comparison between the in-gap field enhancement in presence of the atomic features is shown. The field enhancement in the presence of the protrusion is 6 time higher than for the rest of the nano-cavity and takes place in a sub-nanometer range from the protrusions.

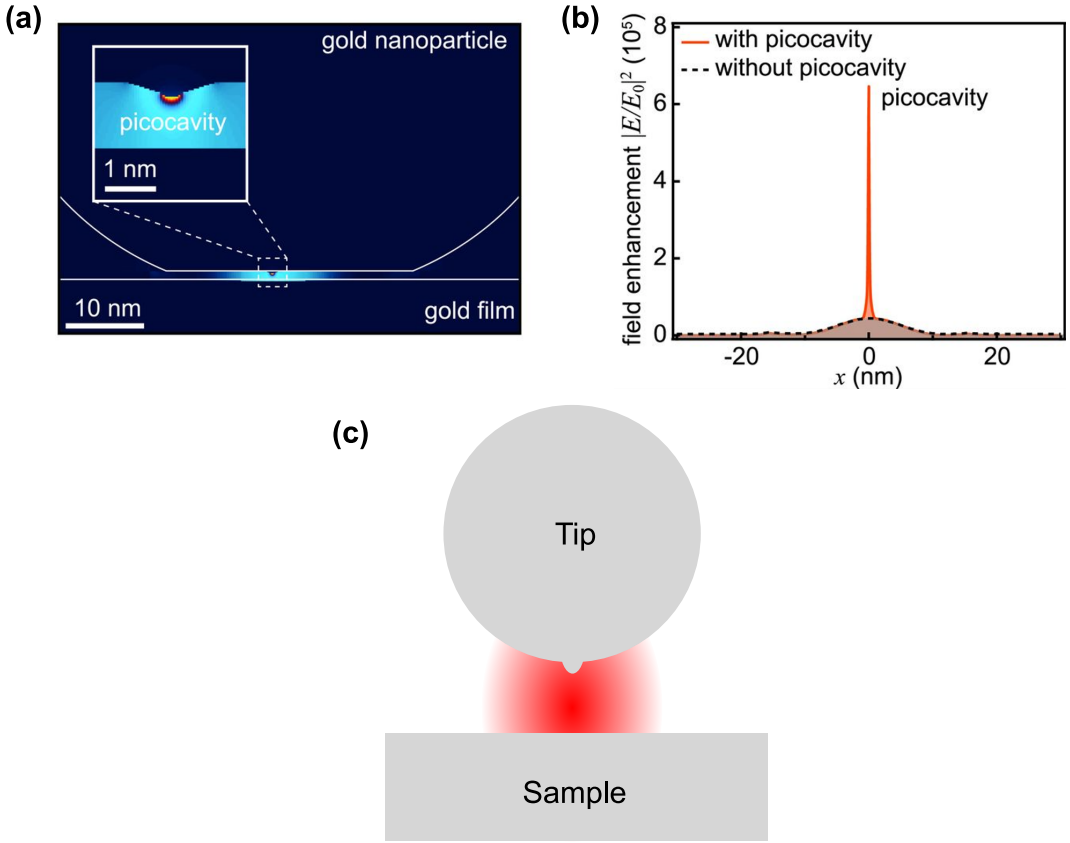

Figure 2.4: **Description of the emission process** Simulations of the system used by Benz *et al.* consisting of a gold nanoparticle and a gold film. **(a)** Near-field map of the system. An inset image shows enlarged view of the picocavity with strong enhancement of the field. **(b)** Comparison of the field enhancement with (red line) and without (dashed line) the picocavity. Adapted from [56]. **(c)** A sketch depicting an STM tip as a $\sim$ 100 nanometer size sphere with a last atom of the tip apex as a sub-nanometer size sphere. The enhancement of LSPs is spatially dependent, with the highest enhancement directly under the last atom. Such system is known as pico-cavity, the respective modes are pico-cavity plasmon modes (PCPs).

The results of Benz can be adapted to an STM junction. In addition to the NCP described previously, we assume that the last atom of the tip apex generates a second cavity called **pico-cavity** which hence contain the **pico-cavity plasmon modes (PCPs)**. The schematic representation of such cavity is given in Fig.2.4(c). In contrast to nano-cavity, the volume of the modes contained is of the order of 1 nm^3. This highly localized enhancement is crucial for a high-resolution vibrational spectroscopy [57] and plays an important role in the framework of this manuscript.

Light emission in STM junction

In a confined STM junction, the density of available eletromagnetic modes is very high. Excitation of such mode is possible at the event of an inelastic tunneling. Considering the energy of electron at the beginning E_i and at the end E_f of the tunneling process, the energy of the excited mode is:

$$h\omega_{pcp} = E_i - E_f, \tag{2.5}$$

and, after the radiative decay, the energy of a corresponding far-field photon is:

$$h\nu = h\omega_{pcp} \tag{2.6}$$

due to a quantum cutoff. Concluding all of the above, STML mechanism lies in the combination of inelastic tunneling electrons and pico-cavity plasmons. This combination can be expressed in the terms of the Fermi golden rule: the rate of emission at the frequency ν is equal to [20]:

$$\Gamma(\nu) = \frac{2\pi}{\hbar^2}|\langle i|\hat{\mu}|f\rangle|^2\rho_{pcp}(\nu, M), \tag{2.7}$$

where $\langle i|\hat{\mu}|f\rangle$ is the transition dipole moment associated to the inelastic transition of an electron from initial state $\langle i|$ to a final state $|f\rangle$ and $\rho_{pcp}(\nu, M)$ is the LDOS available at the frequency ν and the position M. The first part of the equation reflects the inelastic tunneling current contribution and the second part describes the plasmonic contribution.

The above description is based on the excitation of plasmon modes by inelastic tunneling electrons, however it is also possible with an external EM field, for example a laser focused on the tip-sample junction. This approach is commonly used nowadays and gave rise to such experimental techniques as tip-enhanced Raman spectroscopy (TERS) [58] and tip-enhanced photoinduced luminescence (TEPL) [31].

2.2 STML of a single molecule

Now that the origin of STML was described, it is possible to narrow the discussion to a specific case of single molecule emission in a junction. First of all, this section covers the interaction between an excited state of the molecule (also known as exciton) and a STM pico-cavity. Next, the luminescence quenching of emission of molecules adsorbed on metal is addressed and the strategies of decoupling of the molecule are introduced. Lastly, the state-of-art of the mechanisms of molecule excitation with STM is given.

2.2.1 Molecular exciton in STM pico-cavity

Let us consider a molecule in an excited state $|e\rangle$ located in a plasmonic pico-cavity. The sketch of such a system is given in Fig.2.5(a).

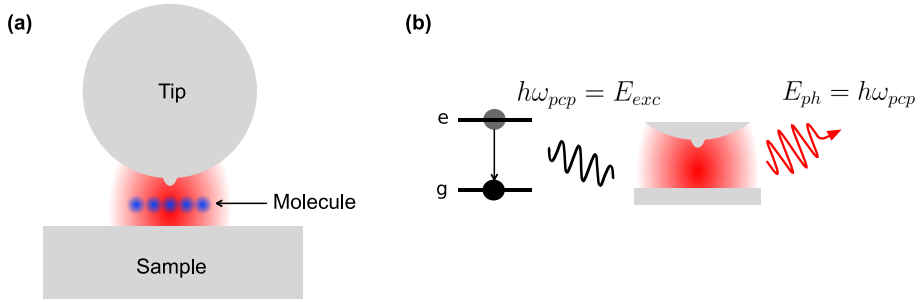

Figure 2.5: **Light emission of a single molecule in a pico-cavity. (a)** A sketch representing a molecule in the STM plasmonic pico-cavity. **(b)** A scheme of a light emission process. Molecular exciton decays into excitation of PCP mode available around energy of exciton. The excited mode sequentially radiatively decays into a far-field photon of an energy equal to the molecular exciton energy.

Since the molecule is located in pico-cavity, there is a high number of PCP modes the molecular exciton can interact with and, therefore, the exciton is likely to decay into the excitation of the available PCP mode of the pico-cavity. The population of the excited state of the molecule (exciton formation) exponentially depends on time:

$$\propto e^{-\Gamma t}, \tag{2.8}$$

where Γ is a decay rate of an exciton. According to Fermi golden rule, exciton decay rate equals to:

$$\Gamma(\omega_{eg}) = \frac{2\pi}{\hbar^2}|\langle i|\hat{\mu}|f\rangle|^2 \rho_{pcp}(\omega_{eg}, M), \tag{2.9}$$

where $\langle i|\hat{\mu}|f\rangle$ is a molecular transition dipole moment from ground to excited state and $\rho_{pcp}(\omega_{eg}, M)$ is the LDOS available around the frequency ω_{eg}. Increase in the number of available modes will increase the PCP excitation rate respectively, an effect known as a Purcell effect [59]. As was mentioned before, the density of PCP modes in pico-cavity is very high, thus the exciton decay rate is high as well. Upon excitation, a PCP mode might sequentially decay by radiation of a photon that can be detected in far-field. The energy of such a photon will be the same as of molecular exciton $E_{ph} = h\omega_{pcp} = E_{exc}$. It means that the far-field photon emitted from an STM pico-cavity is actually a fluorescence signal of the molecule. The rate of the pico-cavity emission is much faster than the decay rate of an exciton, therefore the total emission rate is limited by the decay rate of an exciton, or a lifetime of an excited state of the molecule. Due to this limitation, the total emission rate can be approximated by 2.9.

As mentioned before, the excited PCP mode might radiatively decay into a far-field photon, however there is also a non-radiative decay path. The quantum yield for this case is given by the ratio of the radiative decay events to a total number of decayed excitations:

$$\theta = \frac{\Gamma_{radiative}}{\Gamma_{total}}. \tag{2.10}$$

2.2.2 Decoupling from the metal

The historically first STML experiments were conducted in a following fashion: the molecules were deposited on a bare metal surface in small amounts and would form clusters or monolayers upon adsorption, as shown in Fig.2.6(a) [3, 60–63]. Such a system allowed to record a strong modification of a plasmonic response caused by the presence of molecules (see Fig.2.6(b)). However, reported spectra are far from the highly resolved emission spectra that are reported nowadays. In the end of the previous section we de-

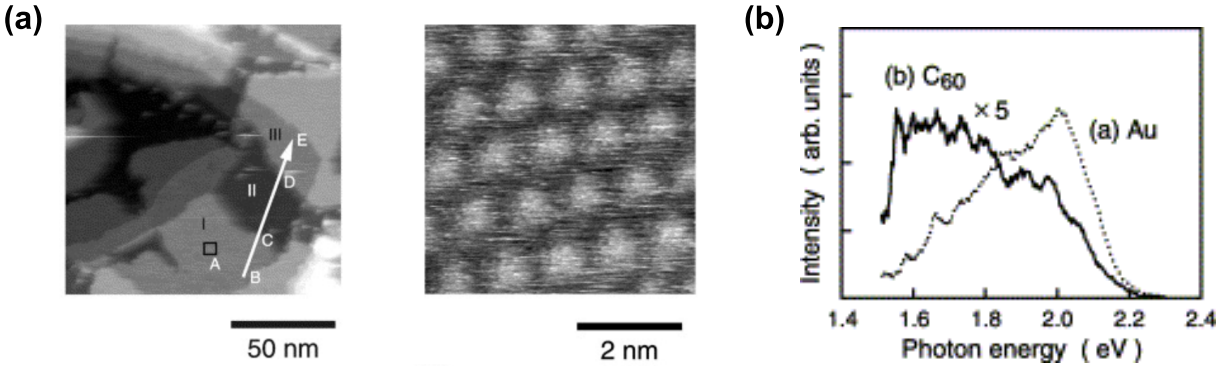

Figure 2.6: **One of the first STML experiments. (a)** STM image of the Au(111) surface covered with ≈0.7 monolayer of C_{60} molecules and a magnified STM image of area A of indicated by a small square. **(b)** STM-L spectra measured the bare Au surface area (dots) and over the C_{60} monolayer-island (solid). The spectrum for the C_{60} monolayer-island is magnified by a factor of 5. Adapted from [63].

scribed the process of radiative decay of a molecular exciton via NCP mode. However, the description was based on the assumption of an ideal system - a single molecule in the vacuum between the tip and the sample. This is not a real STM experiment configuration, where the molecule is adsorbed on the metallic sample. In this case, molecular exciton, instead of decaying into excitation of one of PCP modes of the pico-cavity, now has a much more preferable path of decay by charge transfer to the metallic sample due to strong electronic state hybridization. This process happens incomparably faster then the decay into excitation of a PCP mode, hence reducing the probability of the light emission of the molecule, causing a quenching of luminescence . To avoid this, the hybridization with metal surface has to be reduced. In other words, the molecule has to be decoupled from the metal, and there are several known strategies to do so.

Decoupling by molecular layers

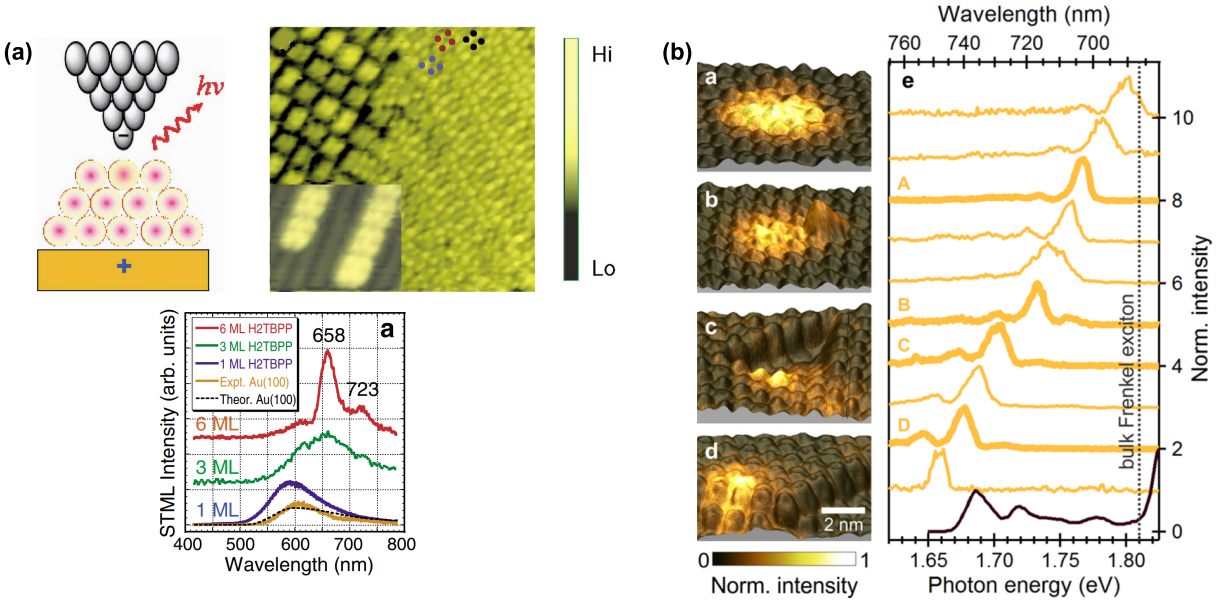

Figure 2.7: **Examples of decoupling from the metal surface by several molecular layers. (a)** Top: schematic junction geometry and STM image of a H_2TBPP molecular stacking at ≈2.5 ML thickness on Au(100) substrate. The inset image shows the adsorption conformation of the striped Au(100). Bottom: STML spectra recorded on the different thicknesses of H_2TBPP/Au(100). Adapted from [64].**(b)** Luminescence of defects in films of 6-10 ML of C_{60} molecules on Ag(111). Adapted from [65]

The first strategy of a molecular decoupling is to deposit a big amount of molecules. The deposition would occur in multilayers in such a way that the top layer is sufficiently decoupled from the metal [22, 64, 66]. A sketch and an STM image of such decoupling strategy are shown in Fig.2.7(a). The main drawback of the multilayer decoupling is the loss of the single-molecule configuration, since any molecule of the top layer can act as an emitter. However, experiments on multilayers of C_{60} with defects (see Fig.2.7(b)) show that the excitation on the defects allow to obtain a single-photon emitting behaviour [65].

Decoupling by suspension of the molecule

The second method of decoupling is applicable specifically to a molecular wires or ribbons (Fig. 2.8c). The idea of this method is based on a suspension of the molecule in the vacuum between a tip and a sample. It is achieved by "picking up" an adsorbed molecule with the tip and sequential retraction of the tip from the sample. Use of this strategy showed to provide the sufficient decoupling for the light emission [4, 67, 68]. The main advantage of this method is the ability to control the decoupling of the molecule by variation of tip-sample distance. However, there are few drawbacks, such as high difficulty of the experimental implementation of this method and a very broad emission lines due to

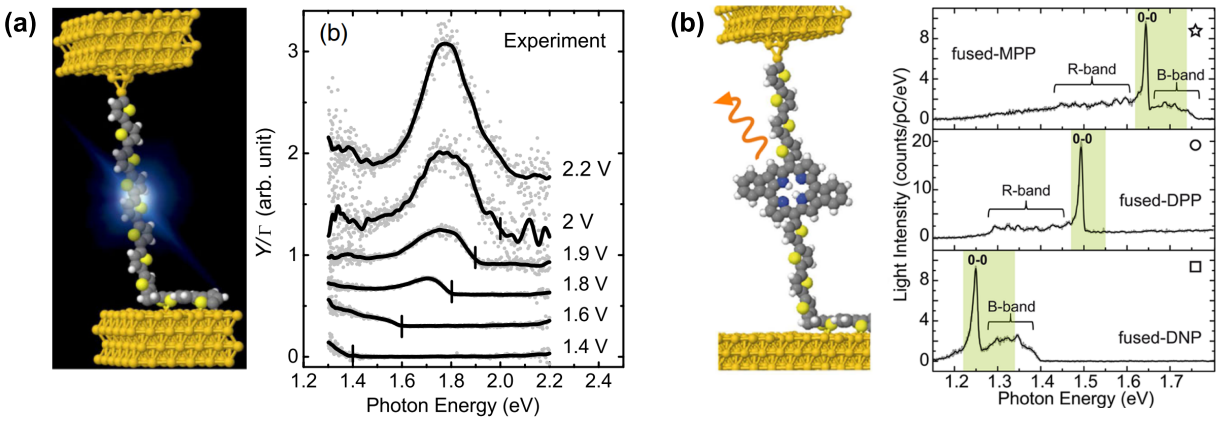

Figure 2.8: **Examples of decoupling from the metal surface by suspension. (a)** Light emission spectra obtained on suspended polythiophene molecule on Au(111) for different biases. Adapted from [67].**(b)** Light emission spectra obtained on different suspended porphyrin-based emitters on Au(111). Adapted from [4]

influence of a contact with both tip and sample. Additionally, any precise luminescence studies are not possible with such configuration due to a lack of access to a spatial resolution of the molecule.

Decoupling by insulating layers

The final method that would be discussed is based on use of the insulating layers such as oxides [2, 69–71] or sodium chloride (NaCl) [5, 7, 11, 12, 72]. Compared to previous examples, this strategy is by far the easiest in implementation and provides the most detailed view on the molecule. Such a system allows to sufficiently decouple a molecule from the metal by adsorption on top of the insulator and simultaneously achieve a single-molecule configuration. Weakening of the hybridization with the metallic surface allows to access the electronic structure of the molecule. STML experiments conducted on molecules adsorbed on insulating layers return an intense and sharp emission.

Out of two, the decoupling with sodium chloride, proposed by Zhang *et al.* in 2016 [5], is the most accessible and popular method at the moment. It was used in most of the recent state-of-art experiments:

- Imaging of dipole-dipole coupling. [5].
- Study of energy transfer process. [7, 8]
- High-resolution vibrational spectroscopy. [6]
- Interaction between an exciton and a plasmonic nanocavity. [29, 73]
- Use of single phthalocyanine molecules as a single-photon emitters. [11]

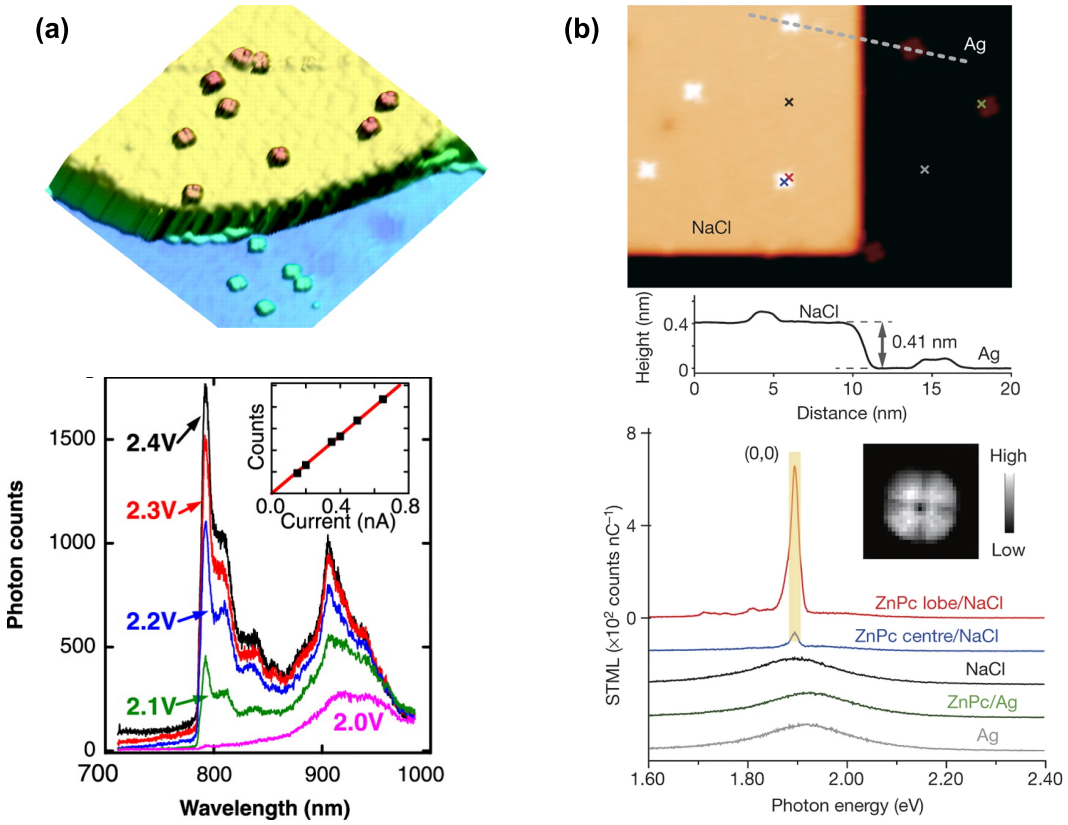

Figure 2.9: **Examples of decoupling from the metal surface by insulating layer. (a)** STM topography of a partially oxidized NiAl(110) surface with ZnEtioI molecules adsorbed on top and corresponding STML spectra recorded on these molecules. Adapted from [2]. **(b)** STM image showing isolated single ZnPc molecules adsorbed on a three-monolayer NaCl island on Ag(100) and STML spectra recorded on molecules and substrates. Adapted from [5].

- Investigation of a triplet state light emission. [12, 21]

- Study of the influence of a tip on the single-molecule fluorescence. [10]

In the scope of the current manuscript, decoupling of single molecules would be performed with an 3 ML insulating layer of NaCl.

2.2.3 Mechanism of excitation of a single molecule

Previously in this chapter we covered the origin of STML in plasmonic pico-cavity formed by a tip and a sample. The decay of an exciton into excitation of a PCP mode and a problem of a hybridization with substrate were covered and explained. However, the process of creation of the molecular exciton hasn't been discussed so far. Now, we will cover the two existing explanations of a mechanism of the molecule excitation.

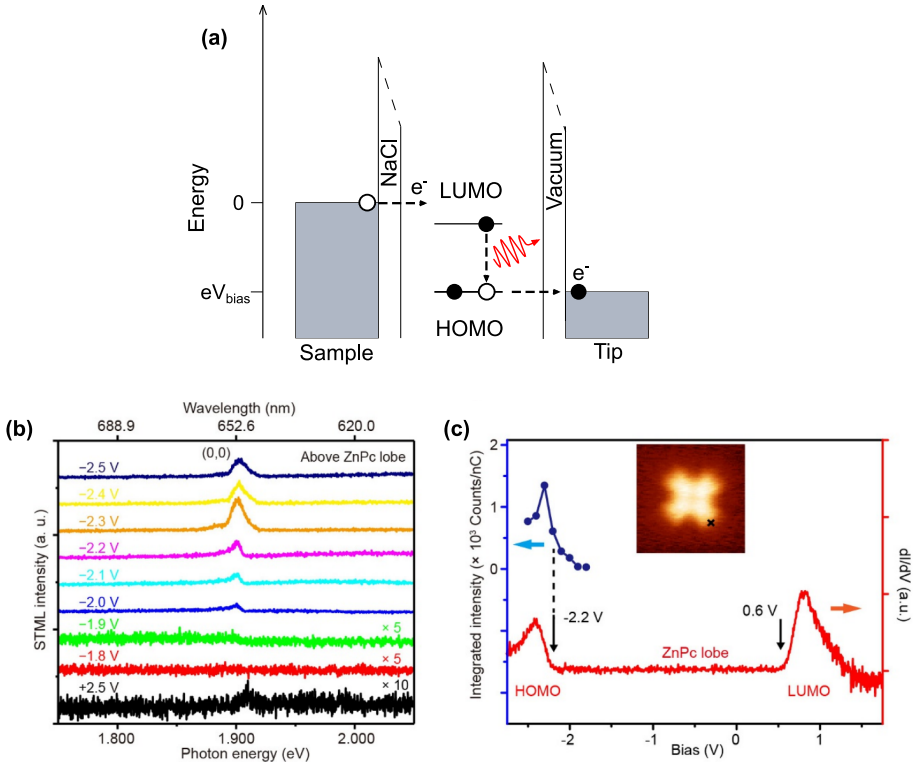

Figure 2.10: **Carrier injection mechanism. (a)** Energy sketch of the proposed carrier injection mechanism on example of a negative bias. An electron is injected from the sample in the LUMO and a hole is injected from the tip in the HOMO. **(b)** Bias dependency of the STML intensity of a single ZnPc molecule. **(c)** Visual comparison of the bias dependency of the STML intensity (in blue) with the $\frac{dI}{dV}$ spectra (in red) of a single ZnPc molecule. Adapted from [5].

Carrier injection mechanism

The first mechanism of a molecule excitation that was proposed is called **carrier injection mechanism** [2, 5, 21]. The explanation is based on the understanding of $\frac{dI}{dV}$ resonances at negative/positive bias as injection of the carrier into HOMO/LUMO respectively. The mechanism consists of a direct excitation of the molecule by a sequential injection of an electron in the LUMO state and a hole in the HOMO state (Fig.2.10(a)). The exciton formation is then followed by a recombination and a photon emission. As stated in the explanation, to allow the carrier injection, an alignment of the HOMO/LUMO state with the Fermi level of the tip/sample is required.

This mechanism is confirmed experimentally by the bias dependency of the STML intensity which is related to the position of ion resonance (here, HOMO and LUMO). Fig.2.10(b) presents the results of Zhang *et al.* where the authors report the STML bias dependency of ZnPc molecule [5]. While the energy of a molecular exciton is around 1.89 eV, the emission starts to increase significantly around -2.0 V (hence electron energy $\leq$ 2 eV), which correspond to the onset of PIR (or HOMO as reported by Zhang *et al.* and shown in Fig.2.10(c)).

One can already see the difference in interpretation of $\frac{dI}{dV}$ resonances in cited literature and in the present manuscript. This point is addressed in Chapter 4 of the manuscript.

Energy transfer mechanism

The second mechanism is called the **energy transfer mechanism**[4, 22, 23]. Similarly to the STML of plasmonic pico-cavity, the molecular excitation is generated by an energy transfer from an inelastic tunneling electrons. The sketch of such a process is given in Fig.2.11(a). In this picture the alignment of the HOMO/LUMO state with the Fermi level is not required. The only condition is for electrons to carry energy high enough to excite the molecule ($eV \geq h\nu$). If this condition is satisfied, the molecular exciton can be generated and sequentially can decay into PCP mode.

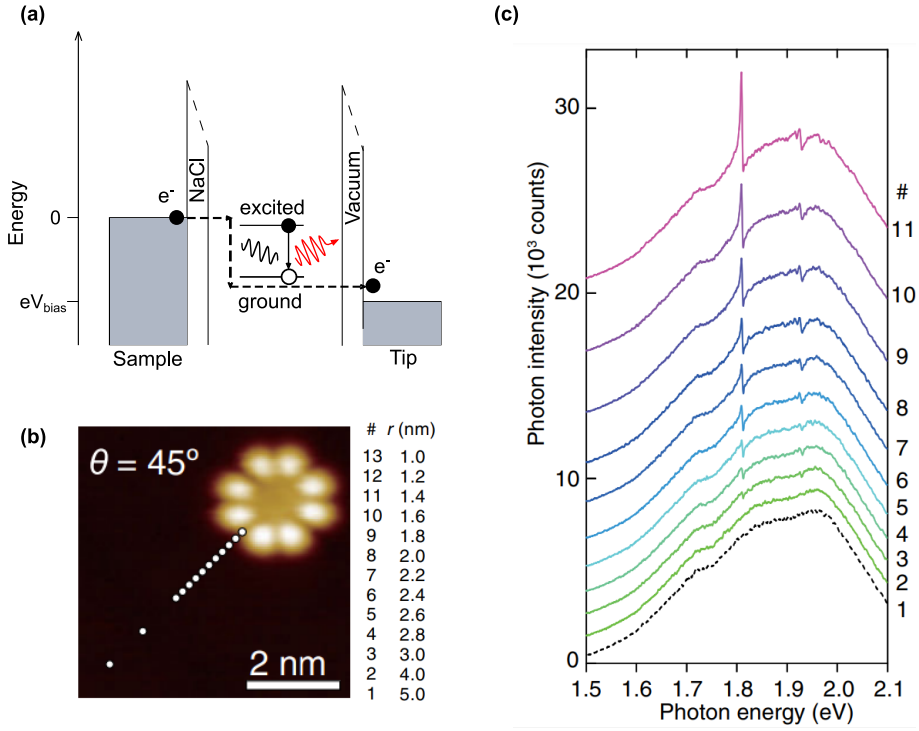

Figure 2.11: **Energy transfer mechanism. (a)** Energy sketch of the proposed energy transfer injection mechanism. An inelastic tunneling electron with energy $eV \geq h\nu$ is injected from the sample. The inelastic nature of the tunneling electron allows to transfer the energy of the electron into excitation of molecular exciton of energy $h\nu$ with consequential PCP mode excitation and luminescence. **(b)** The measurement tip positions for the STML spectra of H_2Pc shown in (c). The column on the right is the list of the distances r measured from the molecular center **(c)** A series of STML spectra measured near the H_2Pc/NaCl with different tip positions on the NaCl film. The Fano-shape dips in the plasmonic emission at 1.81 eV and 1.92 eV indicate the position on resonance with the molecular excited states. Adapted from [73].

The same mechanism works for the molecular exciton generation by the plasmonic modes radiation. If the energy conditions are satisfied, the molecule can be excited as soon as the molecule is exposed to the presence of the plasmonic cavity. The case of

such excitation is given in Fig.2.11(b) as adaptation of results of Imada *et al.* [73]. The authors conducted experiment on a single H_2Pc molecule by gradually approaching the tip to the molecule from the side. The STML spectra given in Fig.2.11(c) show that, at a distance of 3 nm from the center of the molecule, the STML generated by the cavity exhibits a Fano-shape features at the energies 1.81 eV and 1.92 eV, which corresponds to the energies of the two singlet excited states of H_2Pc.

Additionally, the energy transfer mechanism was expanded to the case of the excitation of single molecule by the neighbouring molecule [7, 8]. The exciton energy of a donor molecule therefore have to meet the energy conditions $h\nu_{donor} \geq h\nu_{acceptor}$.

Combination of the two mechanisms

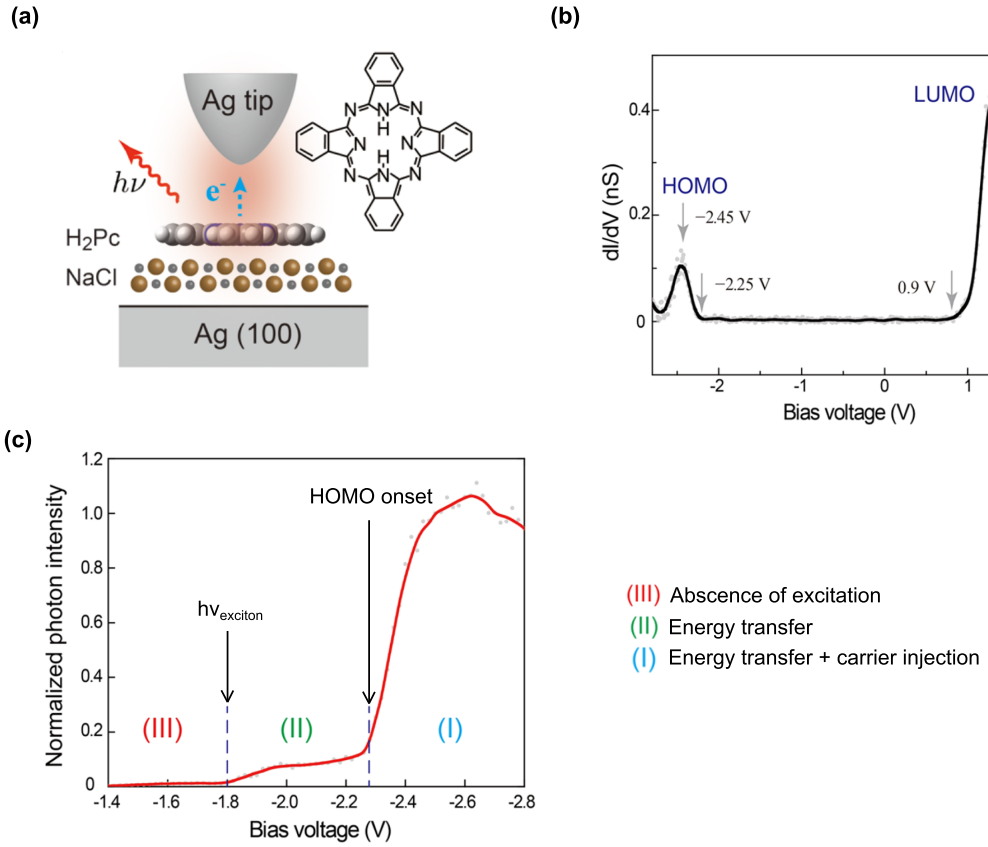

Figure 2.12: **Interplay between the carrier injection mechanism and the energy transfer mechanism.** **(a)** Sketch of the experiment performed by Chen *et al.*. The single H_2Pc molecules were deposited on NaCl/Ag(100) substrate. **(b)** $\frac{dI}{dV}$ spectra of a single H_2Pc molecule. The positive/negative ion resonances are indicated as HOMO/LUMO respectively. **(c)** Normalized bias-dependent intensity of the main peak of H_2Pc luminescence spectra recorded at a constant current of 100 pA. Adapted from [74].

The two previously discussed mechanisms of the molecule excitation were proposed separately. However, in the work by Imada *et al.*, that was shown earlier, the authors report a drastic change in STML intensity as soon as the tunneling takes place not nearby,

but on top of the molecule [73]. Additionally, in another work Imada *et al.* report two different voltage regimes in STML intensity recorded on top of the molecule [7]. Those two observations leaded the authors to assume an interplay between the two excitation mechanisms.

The detailed investigation of this interplay was experimentally conducted and reported by Chen *et al.* in 2019 [74]. The results reported by the authors are shown in Fig.2.12. The experiment was conducted on a single H_2Pc molecule adsorbed on NaCl/Ag(100) substrate (as shown in sketch in Fig.2.12(a)). The $\frac{dI}{dV}$ recorded on a molecule is shown in Fig.2.12(b). It reveals two ion resonances, one for negative bias (labeled as HOMO) and one for positive bias (labeled as LUMO). Fig.2.12(c) presents the bias-dependent study of a main emission peak of H_2Pc STML spectra (as mentioned earlier, the energy of this peak is 1.81 eV). The authors report three regimes of STML as a function of bias. The first regime (labeled as (III)), when the bias is increased from -1.4 to -1.8 V, shows no STML on the molecule. The second regime (labeled as (II)) starts when the bias reaches -1.81 V, a value that corresponds the electron energy of $\leq$ 1.81 eV. This energy is meeting the conditions for the energy transfer mechanism, hence the STML of H_2Pc starts to occur. The third regime (labeled as (I)) takes place at a bias equal to -2.25 V. That value corresponds to the position ion resonance of the molecule (labeled as HOMO in Fig.2.12(b)). It meets the conditions of the orbital alignment that were discussed earlier, hence enabling the carrier injection mechanism. At the same time, the conditions of the energy transfer mechanism are still respected. As a result, STML intensity has a drastic increase with bias at this regime, meaning that the photon yield is much higher. Such results hint that, even though the carrier injection mechanism is dominant, the energy transfer mechanism still occurs.

Chapter 3

Internal Stark Effect of a single molecule fluorescence

Introduction

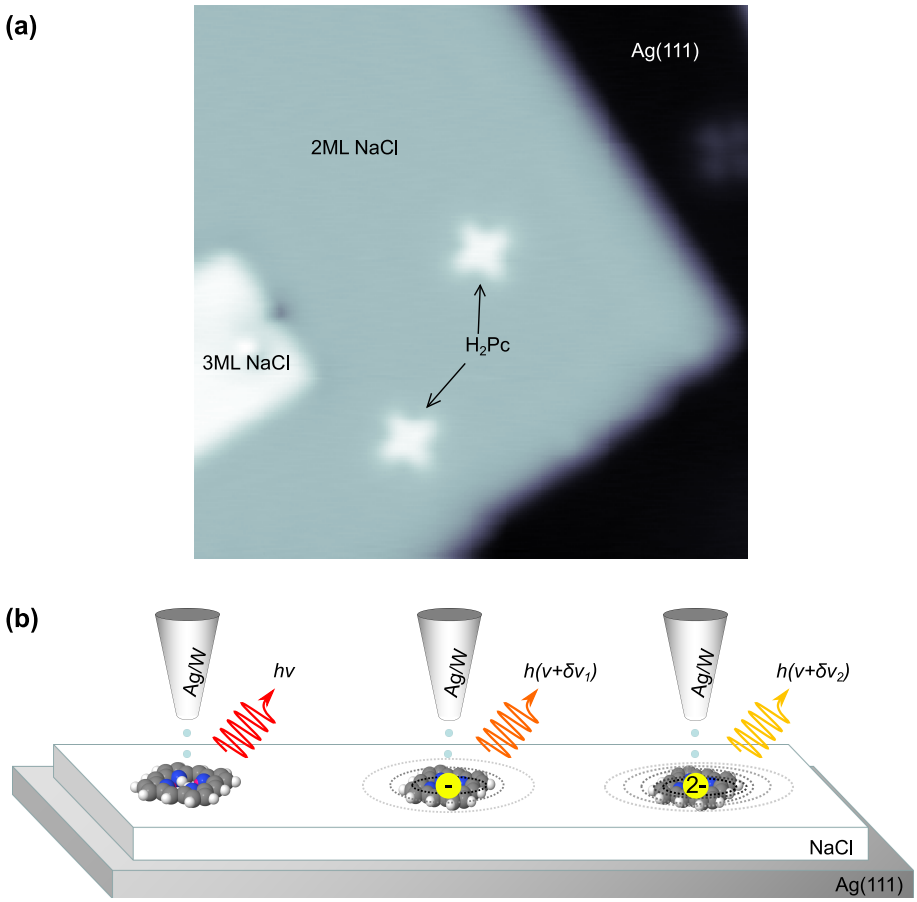

Figure 3.1: **Overview of the experiment. (a)** A 15×15 nm^2 in-gap topography STM image of the system of interest. Single H_2Pc molecules are thermally evaporated on 2-3ML NaCl/Ag(111) sample. **(b)** A sketch of the experiment. The central hydrogen atoms of a single H_2Pc molecule are deprotonated with the STM tip by a voltage ramp. The excess electrons remain in the molecule and generate an electric field, which in turn influences the fluorescent energy of the molecule.

In many chemical and biological systems, the electric fields generated by embedded electrostatic charges regulate the absorption or emission energies of chromophores. [75–

77]. This phenomenon, known as internal Stark effect (ISE), [77–79] contrasts with Stark shifts induced by external electric fields[80, 81]. ISE occurs in complex landscapes composed of a large number of interacting organic systems. In the field of STM, Stark effect experiments are limited to studies when molecular electronic states are influenced by the external electric fields generated at the tip-sample junction [10, 82–84]. In-depth STML study at a single-molecule scale would constitute an ultimate ISE investigation and would allow for the more improved understanding of the chromophore emission mechanism.

This chapter reports on an internal Stark effect experiment realised with free-base phthalocyanine (H_2Pc) molecules deposited on a NaCl-covered silver Ag(111) sample. An example image of the system is shown in Fig.3.1(a). Here, a systematic approach based on sequential deprotonation of the central hydrogens of the molecule is proposed. The deprotonation leaves an excess electron in the molecule, which in turn generates an electric field, shifting the energy of emission of the chromophore. The sketch of this experiment is shown in Fig.3.1(b). The chapter starts with a study of a single H_2Pc molecule. Then, the deprotonation procedure is proposed and implemented in order to successively remove the two central protons of a H_2Pc molecule. STM images and topographic time traces are used to identify the nature of the deprotonated species and their electronic structure. The results show strong changes in the dynamics of the central hydrogen movement (process known as tautomerization). $\frac{dI}{dV}$ spectra reveal a rigid shift of the electronic gap with each deprotonation step, indicating (I) the preservation of the π-orbital structure of H_2Pc and (II) a Stark shift of the electronic states of the molecule. As a consequence, the neutral and deprotonated compounds are iso-electronic, in contrast with scanning probe experiments in which charging a molecule alters its π-orbitals[11, 12, 24–27].

STML spectra recorded on the singly and doubly deprotonated compounds reveal a blue shift of fluorescence emission energy compared to the original H_2Pc chromophore. A comparison with time-dependent density functional theory (TD-DFT) simulations reveals a parabolic dependence of the emission energies based on the intrinsic charge of the molecule. The presence of non-vanishing linear term of the parabolic dependence allows to identify the role played by the proximity between a chromophore and a point-like electrostatic field source. The deprotonation procedure also affects the vibronic emission of the molecule, inducing measurable frequency shifts for several modes, an effect that is discussed in terms of a vibrational Stark effect [28].

3.1 Experimental results

3.1.1 Electronic and fluorescence properties of H_2Pc molecule

For the experiment, H_2Pc was thermally evaporated on the 3ML NaCl/Ag(111) substrate. In Fig.3.2(a) STM images of a H_2Pc molecule are shown.

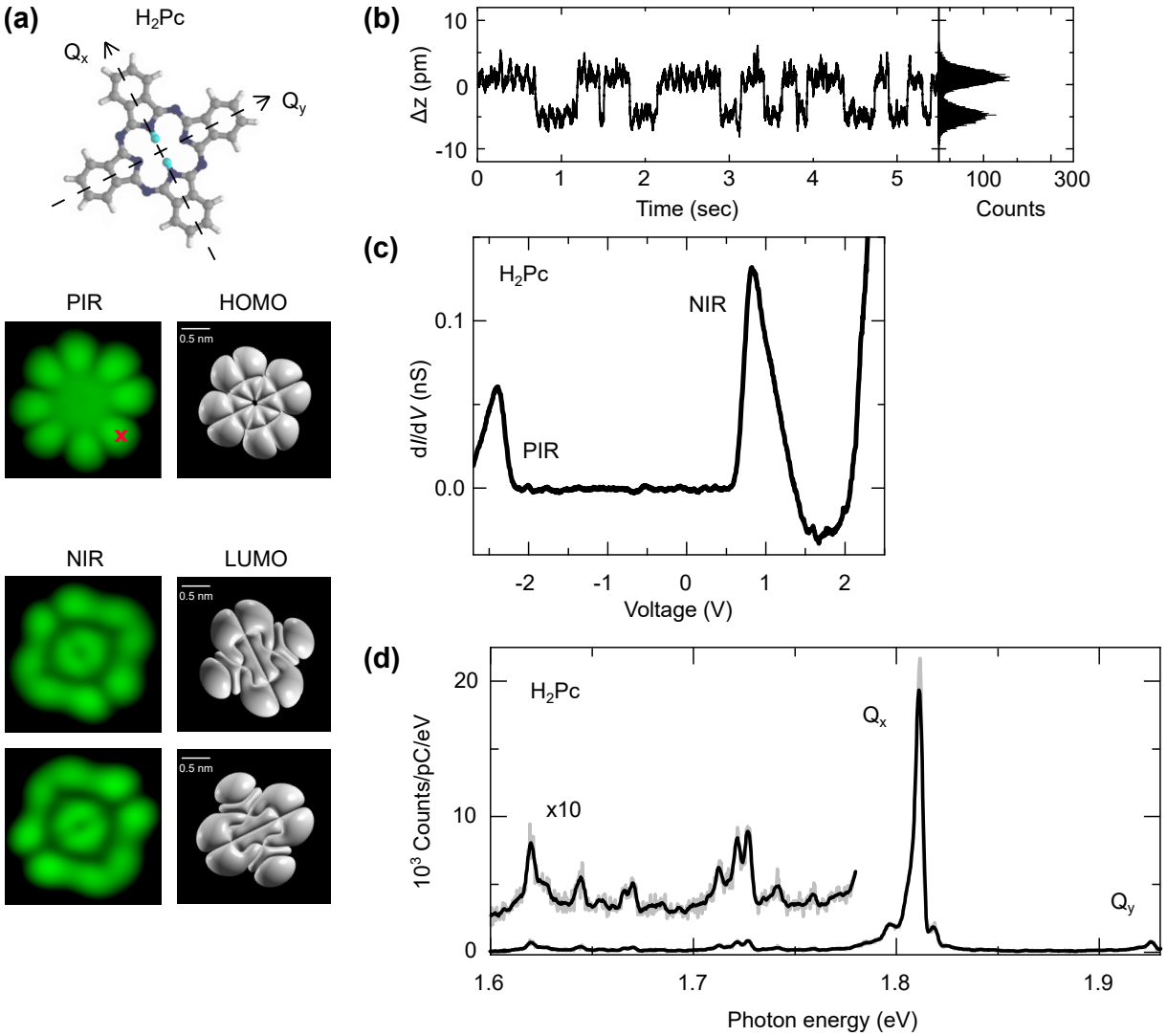

Figure 3.2: **Electronic and fluorescence properties of a free base phthalocyanine (H_2Pc) molecule. (a)** Ball-and-stick sketch of the molecule (white and light-blue - H, grey - C, blue - N atoms), STM images recorded with $I = 10$ pA and corresponding calculated orbitals. The PIR image was recorded at $V = -2.5$ V. The NIR images were recorded at $V = 0.5$ V. Right to the images the DFT calculations of HOMO and LUMO orbitals are shown. **(b)** Tip height time trace recorded at a constant current ($I = 5$ pA) revealing the tautomerization of the central hydrogens. **(c)** $\frac{dI}{dV}$ spectrum recorded on top of one of the axis of the molecule (marked with x in the PIR image). The bias is sweeped from -2.7 V to 2.5 V at constant height. The $\frac{dI}{dV}$ spectrum reveals two peaks, one at negative and one at positive bias. The peak at negative bias corresponds to the PIR of the molecule, the peak at positive bias corresponds to NIR. **(d)** STML spectrum obtained on the lobe of the molecule (marked with x in the PIR image). The light emission spectrum was recorded with $t = 120$ s, $I = 100$ pA and $V = -2.5$ V. The magnified inset spectra reveals vibronic peaks of the molecule.

The images are recorded at voltages corresponding to resonances in $\frac{dI}{dV}$ spectrum of the molecule. The top image is recorded at $I = 10$ pA and $V = -2.5$ V, at a bias that corresponds to the PIR of the molecule (the first peak in the $\frac{dI}{dV}$ at negative sample bias). The image reveals an 8 lobe structure that is in a good agreement with DFT calculations

of the HOMO of the molecule performed by theory collaborator Hervé Bulou. Images recorded at $I = 10$ pA and $V = 0.5$ V, i.e. the bias that corresponds to the NIR (the first peak in $\frac{dI}{dV}$ on the positive side of bias), are shown below, together with DFT simulations of the LUMO of the molecule. Here, two different structures can be recorded, that appear similar but rotated by 90° one from the other. This behaviour is explained by the current-induced rotation of the central hydrogen atoms between two equivalent positions. This process is known as tautomerization. To better characterize this process, we positioned the tip on top of one of the axis of the molecule (marked with x) at a constant current ($I = 5$ pA) and record the tip height time trace. The resulting dataset (Fig.3.2(b)) reveals two different values of the tip height, which are associated to two different positions of the hydrogen in the center. Summing up the points of this time trace into a histogram (right part of plot) demonstrates that the two positions are equally probable.

A $\frac{dI}{dV}$ spectrum recorded on top of one of the lobes of the molecule (marked with x) is shown in Fig.3.2(c). The spectrum reveals two peaks that correspond to the PIR and the NIR of the molecule at negative and positive bias respectively. The onset of the PIR is at $V = -2.25$ V and the one of the NIR is at $V = 0.45$ V.
Fig.3.2(d) show an STML spectra obtained on the molecule. The experiment was performed on top of one of the lobes of the molecule (marked with x) with $I = 100$ pA and $V = -2.5$ V over $t = 120$ seconds. The light emission spectrum contains two main emission peaks at 1.81 eV (labeled Q_x) and at 1.94 eV (labeled Q_y). The lower energy peak Q_x corresponds to an emission of the excited dipole oriented along the molecular axis with the two central H atoms (see also sketch in Fig.3.2(a)). The higher energy peak Q_y corresponds to the emission dipole oriented along the orthogonal molecular axis. The vibronic fingerprint is very low in intensity compared to the main emission peak, therefore it is additionally plotted with a 10 times magnification on top of the actual spectra for a better resolution.

3.1.2 Deprotonation procedure

To deprotonate one of the central hydrogen atoms of the molecule, the following procedure is performed. The tip is positioned on top of the center of the molecule. After that, the bias between the tip and the sample is continuously increased from $V = 0.5$ V to $V = 4$ V. By simultaneous recording the changes in tip height (Δz), it is possible to monitor changes of the chemical structure of the molecule at $V = 3.2$ V (marked by the red dashed line in Fig.3.3). The STM images of the molecule recorded before and after the voltage ramp reveal a strong change in the appearance of the HOMO pattern characteristic of the PIR. The previously "clear" STM image now appears "noisy", however the 8 lobe structure remains unchanged. The behaviour of the tip during the bias increase and drastic change of the molecular appearance indicate that one of the central hydrogens was modified. Later

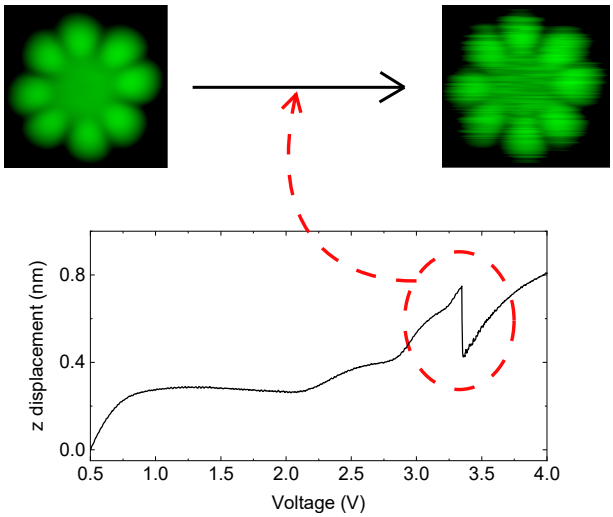

Figure 3.3: **Procedure to deprotonate the central hydrogen atom.**

in this chapter, detailed nature of this modification discussed in terms of deprotonation and dehydrogenation will be addressed. However, at this stage of the presentation we will assume that the H_2Pc molecule is deprotonated. From now on, we will refero to the singly deprotonated molecule as HPc^-.

3.1.3 Electronic and fluorescence properties of HPc^- molecule.

In Fig.3.4(a) STM images of a HPc^- molecule are shown. The PIR image is recorded at $I = 10$ pA and $V = -1.5$ V and is in a good agreement with TD-DFT calculations of the HOMO of the singly deprotonated H_2Pc. The imaging reveals an 8 lobe structure that strongly resembles the PIR image of H_2Pc but the image seems affected by a noise. The images recorded at $I = 2.3$ pA and bias $V = 1.43$ V that corresponds to NIR are shown below. The DFT calculations of the singly deprotonated H_2Pc LUMO are in good agreement with experimental images. In contrast with H_2Pc and its two equivalent tautomeric configurations, the modified molecule adopt four different configurations. By positioning the tip on top of one of the axis of the molecule (marked with x), it is possible to record the tip height time trace and visualize the tautomerization process for this molecule as well (Fig.3.4(b)). The plot shows four different values of the tip height that can be associated to the four different configurations of the molecule. Summing up the points of the plot into histogram (right to the plot) suggests that the four configurations are equally probable.

A $\frac{dI}{dV}$ spectrum recorded on top of one of the axis of the molecule (marked with x in the PIR image) is shown in Fig.3.4(c). The spectrum reveals two peaks that correspond to the PIR and the NIR of HPc^-. The onset of the PIR is at $V = -1.3$ V and of the NIR is at $V = 1.4$ V. Fig.3.4(d) shows an STML spectra obtained on the molecule. The experiment was performed on top of one of the axis of the molecule (marked with x) with

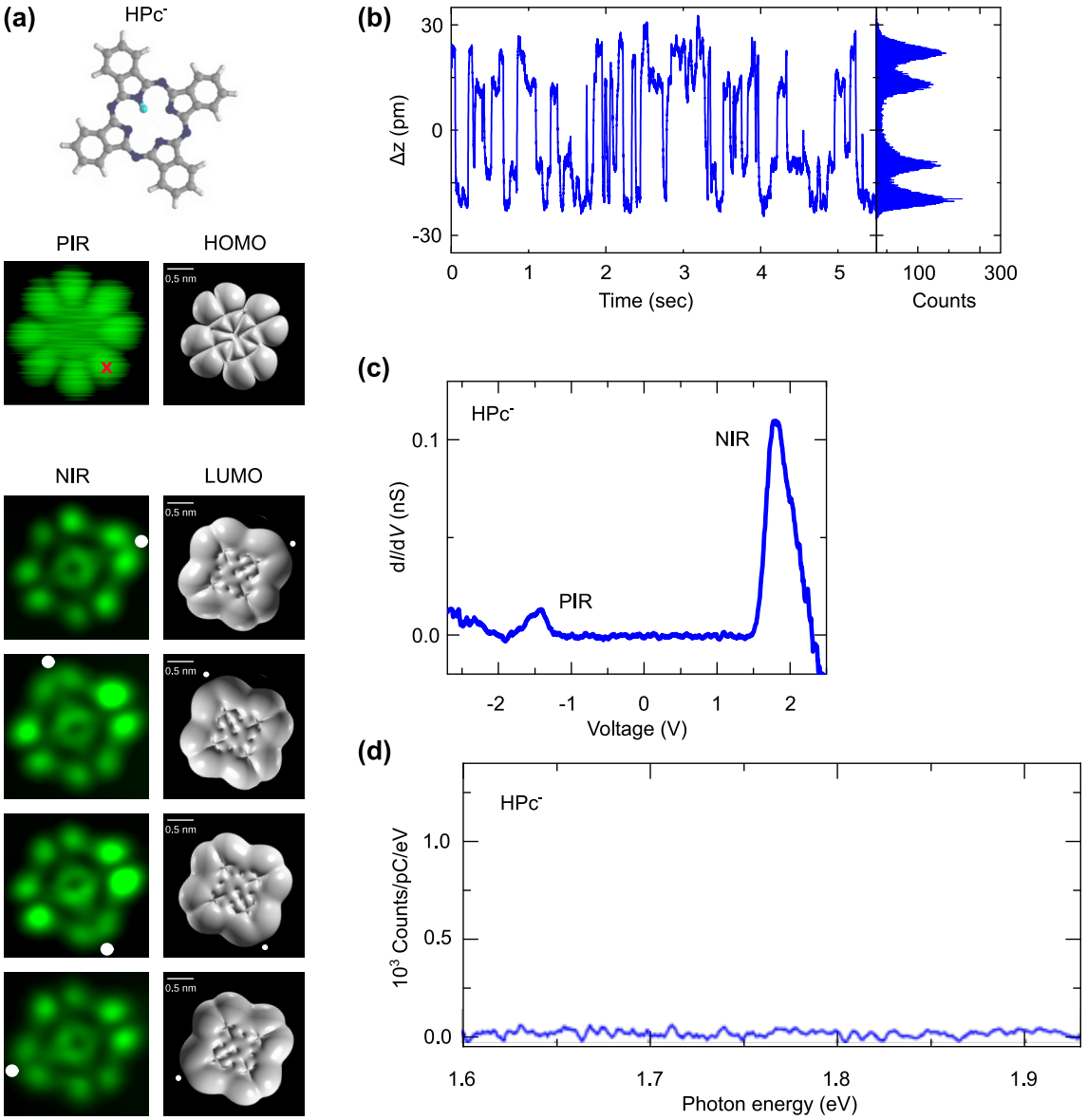

Figure 3.4: **Electronic and fluorescence properties of HPc^- molecule.** **(a)** Ball-and-stick sketch of the molecule (white - H, grey - C, blue - N atoms), STM images and corresponding calculated orbitals. The PIR image was recorded with current $I = 10$ pA at bias $V = -1.5$ V. The NIR images were recorded with current $I = 2.3$ pA at bias $V = 1.43$ V. Right to the images the DFT calculations of HOMO and LUMO orbitals are shown. **(b)** Tip height time trace recorded at a constant current ($I = 5$ pA) revealing the tautomerization of the central hydrogen. **(c)** $\frac{dI}{dV}$ spectrum recorded on top of one of the axis of the molecule (marked with x in PIR image). The bias is sweeped from -2.7 V to 2.5 V at constant height. The $\frac{dI}{dV}$ spectrum reveals two peaks, one at negative and one at positive bias. The peak at negative bias corresponds to the PIR of the molecule, the peak at positive bias corresponds to the NIR. **(d)** STML spectrum obtained on the lobe of the molecule (marked with x in the PIR image). The light emission spectrum was recorded with $t = 120$ s, $I = 100$ pA and $V = -2.5$ V.

$I = 100$ pA over $t = 120$ seconds for different values of both signs of the tip-sample bias. Here, no fluorescence was registered.

Additional STML experiments on HPc^-

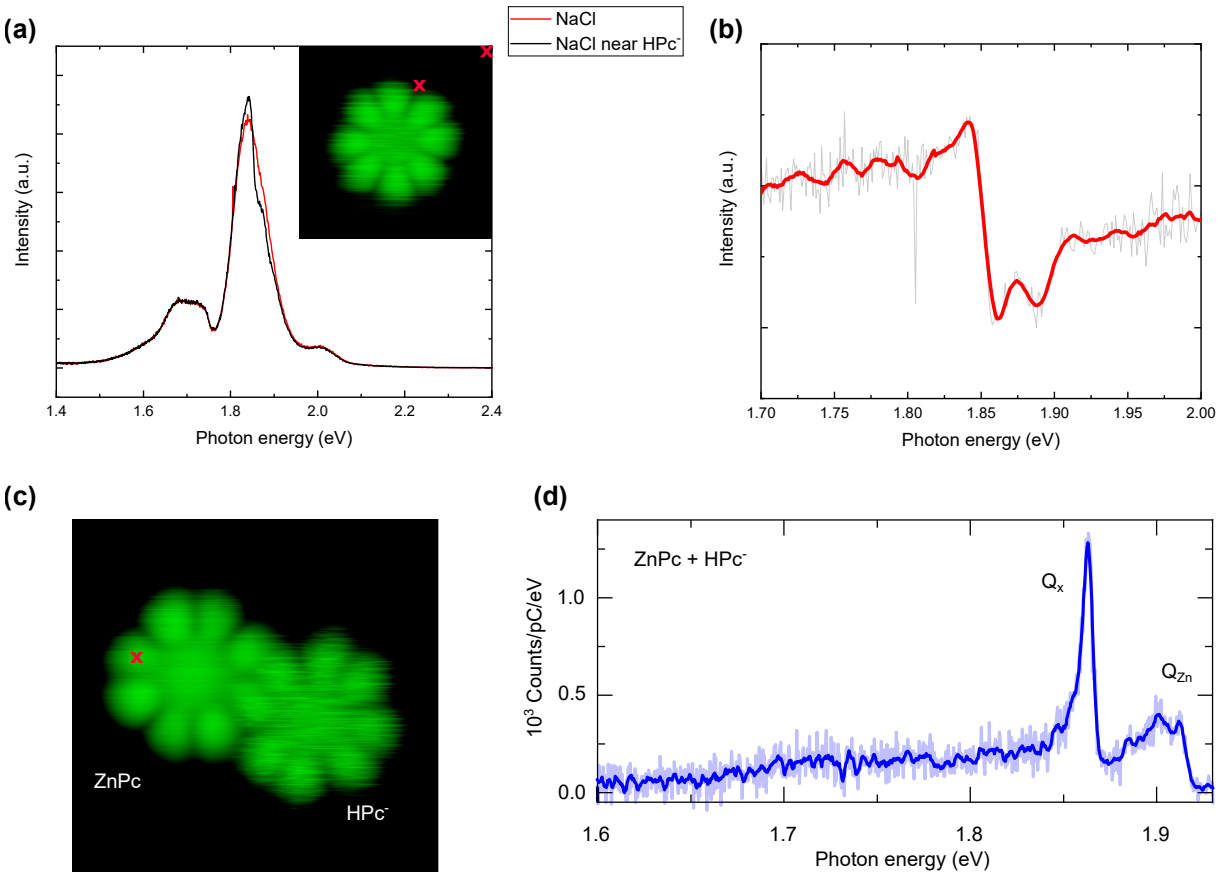

Figure 3.5: **Additional STML experiments in order to obtain the fluorescence of HPc^- molecule. (a)** Excitation of the molecule via energy transfer from the plasmonic cavity. STML spectra recorded on NaCl substrate away from any molecule (in red), and on NaCl in close proximity to the molecule (in black). Both spectra were recorded at $I = 100$ pA and $V = -2.5$ V during $t = 60$ s. **(b)** STML spectrum recorded in close proximity to the molecule normalized by the plasmonic background. **(c)** STM image of an ZnPc - HPc^- molecular dimer. The ZnPc molecule is positioned in such a way that it nearly "touches" the HPc^- molecule. For the STML experiment, the excitation is performed on the ZnPc molecule, on top of the molecular lobe that lies on the axis of the dimer (marked with x). **(d)** STML spectra obtained on the molecular dimer by direct excitation of the ZnPc molecule with $I = 60$ pA and $V = -2.5$ V during $t = 120$ s.

To record the fluorescence of this molecule, we adopted a different strategy, which rely on an indirect excitation of the molecule.

A first approach consists in exciting the HPc^- molecule via energy transfer from the plasmonic cavity of the STM junction. Fig.3.5(a) shows two spectra: the red one was acquired on NaCl far away from any molecule and is characteristic of the plasmonic emission of the cavity. The black one was acquired on NaCl in close proximity to HPc^-. Normalizing the black spectra by the plasmonic background leads to the spectrum presented in Fig.3.5(b). Here, one can see a dip in intensity around 1.86 eV. This spectral feature can be associated to the interaction of the molecular exciton with the plasmonic field of

the STM junction. The energy of the dip minimum in this spectrum indicates the HPc^- exciton energy.

A second approach is based on an energy transfer from a neighbouring donor molecule having a higher exciton energy. Similar STML experiments were performed in the past to transfer energy between donor and acceptor chromophores [8, 85]. Here, a single zinc phthalocyanine (ZnPc) molecule was chosen as donor. The molecular dimer (Fig.3.5(c)) was arranged in-situ by STM tip manipulations. Next, an STML spectrum was recorded by positioning the tip on top of ZnPc molecule with $I = 60$ pA and $V = -2.5$ V during $t = 120$ s. The resulting light emission spectrum is given in Fig.3.5(d) and contains two emission peaks. Since the ZnPc molecule was thoroughly studied before, it is possible to assign the emission line at 1.9 eV to be main emission peak of ZnPc(labeled Q_{Zn}). The second peak at 1.86 eV is then associated to the main emission line of HPc^- molecule (labeled Q_x). This value is further supported by the excellent agreement with the data reported in Fig.3.5(b). Due to the low intensity of the emission, no vibronic fingerprint was resolved. The resulting spectra will be used later in the manuscript for comparison with the other molecules.

3.1.4 Electronic and fluorescence properties of Pc^{2-} molecule.

By performing a deprotonation procedure for a second time, it is possible to remove the remaining central proton of the molecule. In Fig.3.6a the recorded procedure is presented. The sudden change of the tip height occurs approximately at the same value of bias ($V =$ 3.2 V) during the sweep, modifying a molecule into a new species, further addressed to as Pc^{2-}. Consecutive imaging of the molecule reveals the 8 lobe configuration of the molecule similar to H_2Pc. However, the noisy appearance caused by intense tautomerization is not present anymore. In Fig.3.6b the STM images of Pc^{2-} molecule are shown. PIR image is recorded at $I = 10$ pA and $V = -2$ V. The imaging reveals an 8 lobe structure that strongly resembles a HOMO orbital of H_2Pc and is in a good agreement with DFT calculations of the HOMO orbital of a doubly deprotonated H_2Pc (right to PIR image). The image recorded at $I = 10$ pA and bias $V = 1.65$ V that corresponds to the NIR is shown below as well as the corresponding calculation of a LUMO orbital (right to NIR image). In contrast with the two previously described species, the tautomerization was not revealed in the imaging. It is confirmed by recording of tip height time trace by positioning the tip on top of one of the axis (marked with x) of the molecule (Fig.3.4b). The plot shows no variation in the tip height, indicating the abscence of tautomerization.

The $\frac{dI}{dV}$ spectra recorded on top of one of the lobes of the molecule (marked with x) are shown in Fig.3.6c. The spectrum reveals two peaks that correspond to PIR and NIR for the negative and positive bias respectively. The onset of the PIR is at $V = -1.1$ V and of the NIR is at $V = 1.6$ V.

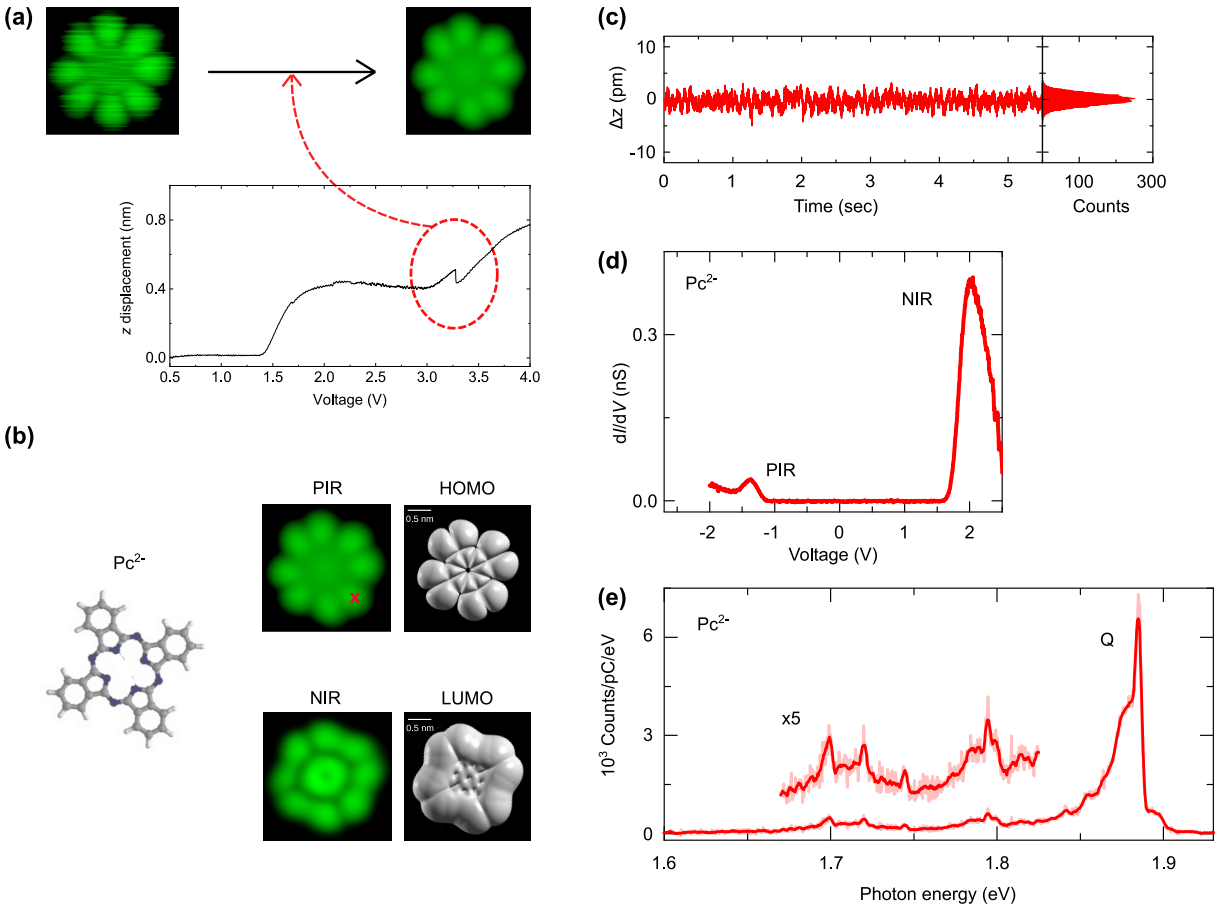

Figure 3.6: **Electronic and fluorescence properties of Pc^{2-} molecule.** **(a)** A deprotonation procedure performed on HPc^- molecule. **(b)** Ball-and-stick sketch of the molecule (white - H, grey - C, blue - N atoms), STM images recorded with $I = 10$ pA and corresponding calculated orbitals. The PIR image was recorded at $V = -2$ V, the NIR image was recorded at $V = 1.65$ V. Right to the images the DFT calculations of HOMO and LUMO orbitals are shown. **(c)** Tip height time trace recorded at constant current ($I = 5$ pA) revealing the abscence of tautomerization. **(d)** $\frac{dI}{dV}$ spectrum recorded on top of one of the axis of the molecule (marked with x in the PIR image). The bias is sweeped from -2 V to 2.5 V at constant height. The $\frac{dI}{dV}$ spectrum reveals two peaks, one for negative and one for positive bias. The peak at negative bias corresponds to the PIR, the peak at positive bias corresponds to the NIR. **(e)** STML spectra obtained on the molecule. The light emission spectra was recorded during $t = 120$ s with $I = 100$ pA and $V = 2.5$ V. The magnified inset spectra reveals vibronic peaks of the molecule.

Fig.3.6e shows an STML spectra obtained on the molecule. The experiment was performed on top of one of the lobes of the molecule (marked with x) with $I = 100$ pA and $V = 2.5$ V over $t = 120$ seconds. The light emission spectrum contains one main emission peak at 1.88 eV (labeled Q). This peak is assigned to the main emission line of a two-times modified molecule. The vibronic fingerprint is very low in intensity compared to the main emission peak, therefore it is additionally plotted with a 5 times magnification on top of the actual spectra for a better resolution.

3.2 Deprotonation or dehydrogenation

The results demonstrate that the induced modifications influence the properties of the molecule: changes in the STM images, in the ion resonances positions and in the emission energies were reported. The time traces indicate that the central hydrogens were affected, however, it is unclear if the molecule was deprotonated or dehydrogenated. To clarify this point, it useful to discuss our data in the light of recent results from the literature.

3.2.1 Dehydrogenation

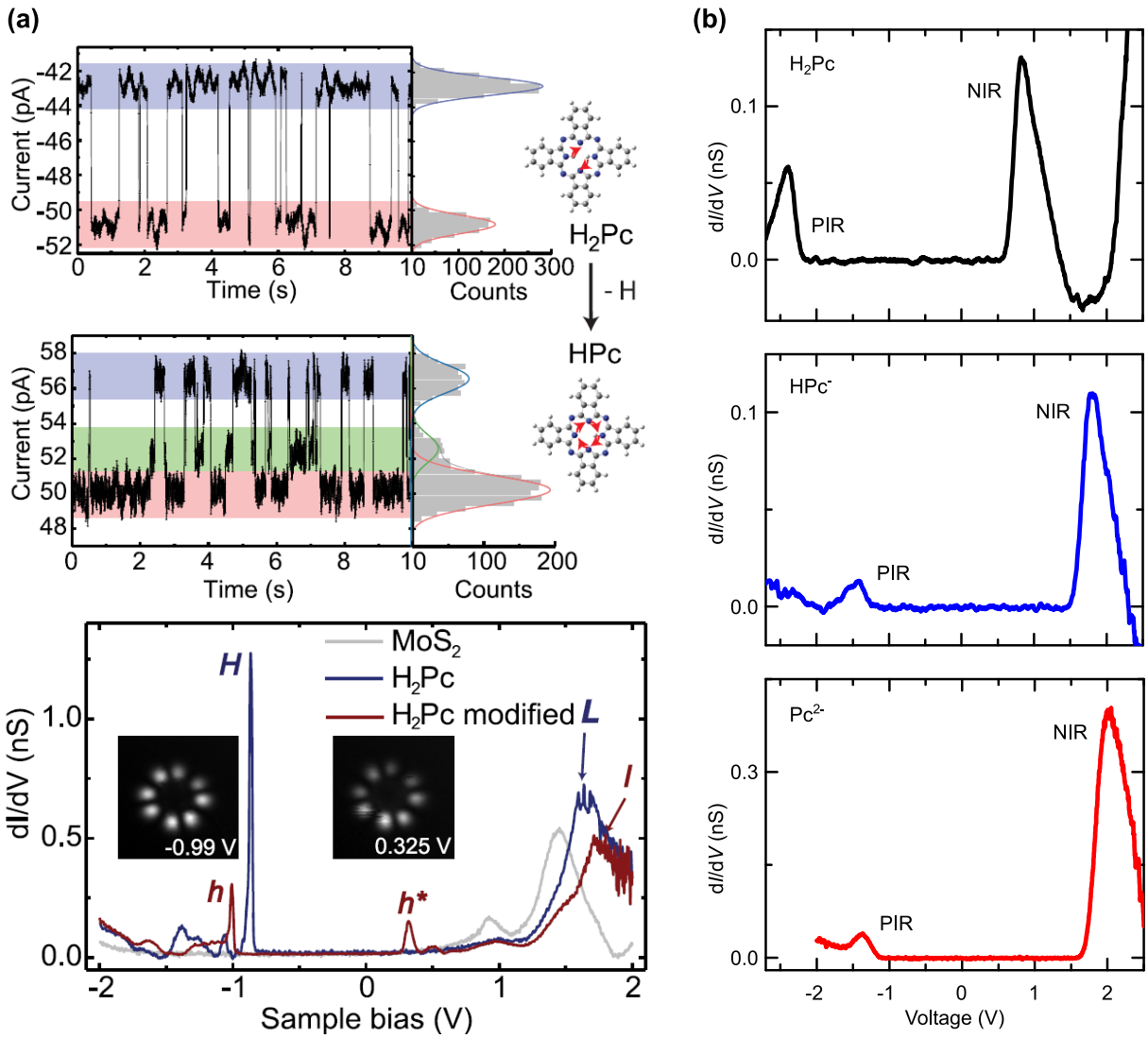

Figure 3.7: **Comparison of STS experiment results.** **(a)** Tautomerization traces recorded on top of H_2Pc (top) and HPc (middle) deposited on MoS_2/Au(111) substrate. The bottom spectra shows the $\frac{dI}{dV}$ spectra recorded on the substrate (grey), H_2Pc (blue) and HPc (red). Adapted from [27] **(b)** $\frac{dI}{dV}$ spectra recorded on H_2Pc (black), one-time modified molecule (blue) and two-times modified molecule (red) deposited on NaCl/Ag(111) substrate in our experiment.

In the work of Reecht et al. [27] an STM experiment on a $H_2Pc/MoS_2/Au(111)$ is conducted. With a single voltage pulse of 3.5 V the authors were able to remove a full single hydrogen atom. The adaptation of their results is given in Fig.3.7(a).

In this figure, the authors present a tautomerization process for both the unmodified and the modified molecule by positioning the tip on top of the molecule and recording a current time trace. The first plot shows that the free-base phthalocyanine molecule exhibits a two-position tautomerization. The second plot recorded on top of the molecule after hydrogen removal returns a three-position time trace, with the lowest current position being twice as probable as the other two, as deduced from the histogram on the right of the plot. The figure on the bottom show a $\frac{dI}{dV}$ spectra obtained on the original molecule (in blue) and on the modified molecule (in red). One can see that after removal of the hydrogen, the conductance spectrum changes drastically: particularly, HOMO of the molecule splits into two different orbitals: a semi-occupied (SOMO) and semi-unoccupied (SUMO) molecular orbitals [86]. In this experiment, the whole hydrogen atom (proton + electron) are removed from the molecule, leaving the molecule in a neutral state with a singly occupied molecular orbital.

For comparison, in Fig.3.7(b) the STS results for our experiment are shown. Plotting the spectra in the same x scale allows to easily observe the shift of the energy positions of the ion resonances for the molecule along the modifications. However, the shift that occurs in our case is completely rigid and the HOMO orbital of the molecule does not experience any splitting.

If the modifications of the molecule affect the central hydrogen atoms and simultaneously do not affect the π electron system, it hints towards the deprotonation rather than dehydrogenation.

3.2.2 Deprotonation

If this assumption is correct, an excess electron should remain in the system, hence leaving the molecule in a charged state. To confirm the presence of a charge, another article from the literature is used. A study of the neutral and charged states of a same molecule on NaCl were conducted by Swart et al. [87]. An adaptation of their results is given in Fig.3.8a. In this paper, the authors were able to charge a copper phthalocyanine (CuPc) molecule in a controllable manner. The charged molecule, deposited on a NaCl/Cu(111) substrate, scatters the surface state of the copper metallic surface. However, when the molecule is charged ($CuPc^-$), the electric field generated by the molecule scatters the surface state much stronger. With STM it is possible to access the scattering pattern of the surface state by performing a differential conductance mapping. For that, one needs to record an STM image in a constant current regime while simultaneously modulating the bias around a value of $\sim$400 mV, such that one can tunnel into interface state between the

NaCl layer and Cu(111) surface. To resolve the difference between scattering on neutral and on charged molecule, Swart et al. subtracted two consecutive images acquired on the neutral and the charged molecules respectively. The resulting scattering pattern is associated to the charge-induced electric field.

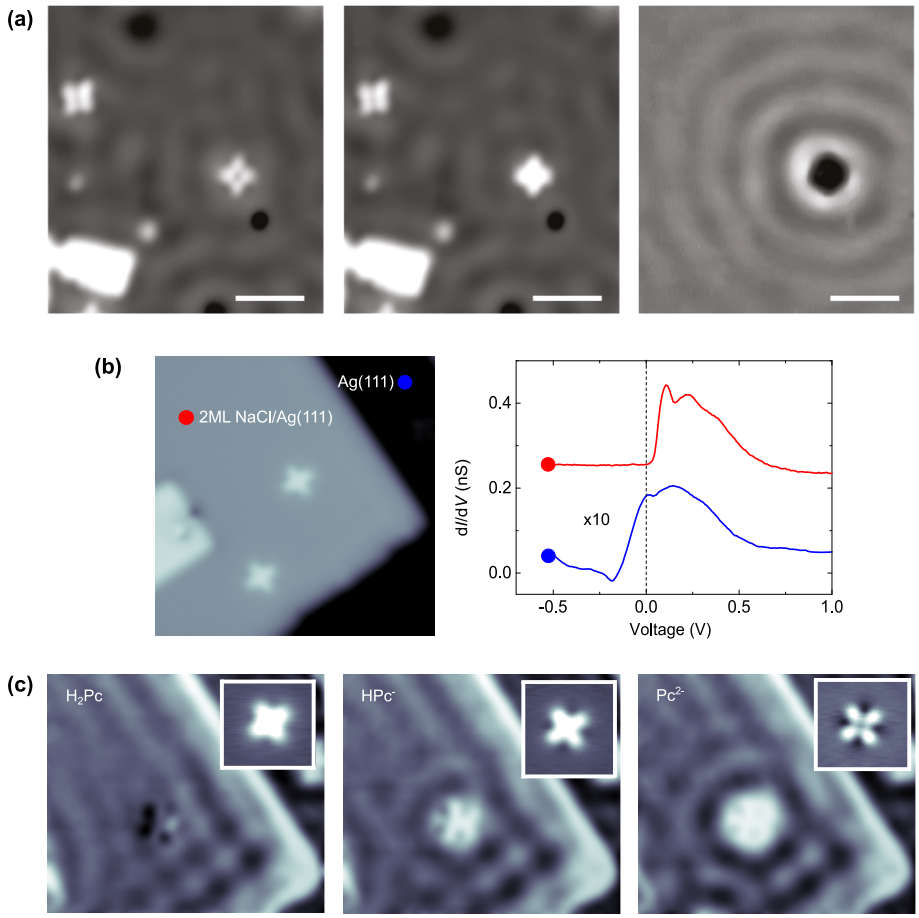

Figure 3.8: **Comparison of differential conductance maps.** **(a)** Differential conductance maps recorded on neutral CuPc (left) and charged CuPc (center) deposited on NaCl/Cu(111). Subtraction of one image from another reveal a scattering pattern centered on the molecule (right). Adapted from [87]. **(b)** STM image of the area of interest of our experiment on H_2Pc and deprotonated molecules deposited on NaCl/Ag(111). In order to obtain the value of bias to access the interface state of NaCl/Ag(111), $\frac{dI}{dV}$ was recorded at two point of the area. The resulting $\frac{dI}{dV}$ spectra are given in the plot (right to the STM image). The red plot shows the conductance spectrum of 2ML of NaC/Ag(111). The blue plot shows the $\frac{dI}{dV}$ spectrum of bare Ag(111). **(c)** Differential conductance maps recorded on H_2Pc (left), one-time modified molecule (center) and two-times modified molecule (right).

In order to reproduce this experiment, a particular area of the sample was chosen (left in Fig.3.8(b)). In this area, a single molecule experiences two consecutive modifications. For each molecule, differential conductance maps are recorded. The bias for the map was chosen based on the $\frac{dI}{dV}$ spectrum obtained on the 2ML NaCl/Ag(111) substrate (right in Fig.3.8(b)). The maps were recorded in a constant current regime ($I = 30$ pA) with

a bias equal to $V = 400$ mV and with bias modulation equal to 50 mV. The resulting differential conductance maps are given in Fig.3.8(c). The first image is the map of the neutral H_2Pc molecule. Comparing to the results of Swart et al., no scattering on the molecule is observed. The only pattern that can be seen is related to the scattering on the borders of NaCl. The map taken on the one-time modified molecule is given in the second image in Fig.3.8(c). The modified molecule not only appear brighter in the image, but also very clearly induces interface state scattering. The second modification (last image in Fig.3.8(c)) appears to scatter the Fermi gas even stronger. The insets of the maps show topographic STM images recorded simultaneously. One can see how a dark area appears and gets more intense around the modified molecules. This behaviour is characteristic of charged molecules on NaCl [87].

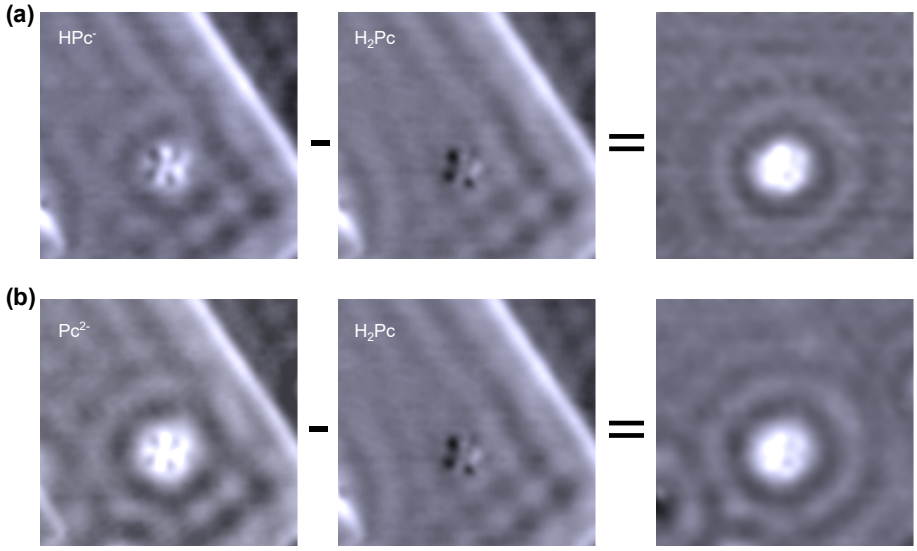

Figure 3.9: **Evidencing the interface state scattering by charged molecules.** Subtraction of the differential conductance map of the neutral H_2Pc molecule from the **(a)** singly deprotonated HPc^- and **(b)** doubly deprotonated Pc^{2-} reveals circular scattering patterns of the interface state between the Ag(111) sample and 2ML NaCl

For a better visualisation, as the one of Swart et al., the subtracted images of the scattering are represented in Fig.3.9. In this figure, the first row (Fig.3.9a) demonstrates the subtraction of the scattering map of a neutral H_2Pc from a map of a singly charged HPc^-. Such a substraction allows to remove the interference from the scattering on the NaCl edges and return only a scattering caused by the charge in the molecule. One can see a scattering around the molecule, which strongly resembles the data reported by Swart *et al.* The second row of images in the figure (Fig.3.9b) shows the result of substraction of the H_2Pc map from the doubly deprotonated Pc^{2-} map. The result shows a more intense scattering around the same molecule, which indicates that the number of charge affects the interaction with the environment.

With the "given evidence", it is possible to confirm that the modification performed on the molecule corresponds to the removal of protons from the central hydrogen atoms. After

deprotonation, a leftover electron remains in the molecule, thus generating an electric field. We have therefore three different molecules, the neutral H_2Pc, HPc^- corresponding to the singly deprotonated and Pc^{2-} corresponding to the doubly deprotonated molecule.

3.2.3 Localization of the excess electrons

Now that we know that the deprotonation procedure leaves the molecule in a charged (or doubly charged) state, the question of where does the charge localize in the molecule remains to be clarified. For that, a series of simulations of the chromophores was performed by the theory collaborators of the team: Herve Bulou, Alex Boeglin and Tomas Neuman. First, density functional theory (DFT) simulations were performed for three molecules in order to calculate the electronic structure of the frontier orbitals as well as their iso-surface representations. For the modified molecule, the proton was artificially removed from the hydrogen atom, whereas the associated electron is left in the molecule. The results of the calculations are given in Fig.3.10 for H_2Pc (a), HPc^- (b) and Pc^{2-} (c).

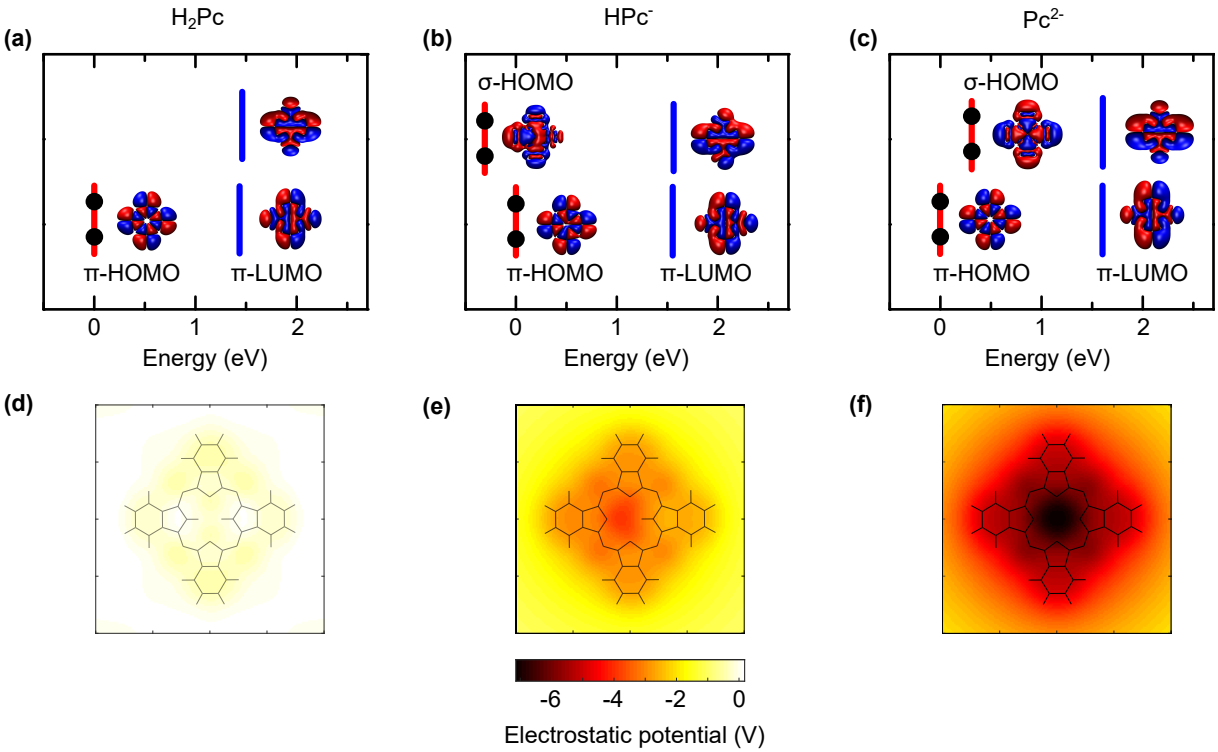

Figure 3.10: **DFT calculations of the frontier orbitals and numerical analysis of the total electrostatic potential.** Top: Density functional theory (DFT) calculations of the frontier orbitals electronic structure of **(a)** H_2Pc **(b)** HPc^- **(c)** Pc^{2-}. HOMO state is chosen at the origin of the energy scale in each case. Inset images correspond to the iso-surface representations of the calculated orbitals. Bottom: Visualisation of calculated electrostatic potential of **(d)** H_2Pc **(e)** HPc^- **(f)** Pc^{2-}

One can see that the gap between the frontier orbitals (π-HOMO and π-LUMO)

does not change upon deprotonation, a result that is in agreement with the experiment (Fig.3.10b). That means that the π-orbitals system remains essentially unchanged. However the simulation return an interesting behaviour for the σ-orbitals system. A σ-orbital that was located 1.7 eV below the π-HOMO for the neutral H_2Pc molecule experiences a large shift towards higher energy upon the deprotonation. For HPc^- this orbital is now located 0.3 eV below the π-HOMO, thus becoming the highest occupied σ-orbital of the molecule. After the second deprotonation, this σ-HOMO is shifted even higher and now positioned 0.4 eV above the π-HOMO. These observations confirm that the leftover electron is not located in the π-orbitals and has a strong influence on the energy of σ-orbital.

To support this assumption, calculations of the electrostatic potential of the molecules generated jointly by the nuclei and the distributed electron density of the singlet ground state of the molecule were performed. The resulting images are given in Fig.3.10 for H_2Pc (d), HPc^- (e) and Pc^{2-} (f). The potential is displayed in a horizontal plane 0.21 nm above the molecule. For the H_2Pc, the potential is very close to zero as expected for a neutral molecule. The one-time deprotonated molecule, HPc^-, exhibits a different behaviour, with a much higher negative potential in the molecule, with a minimum localized in the center of the molecule, close to the deprotonation site. In addition, the electrostatic potential now extends beyond the molecular skeleton. Upon the second deprotonation, the negative potential becomes much stronger and the distribution outside the molecule increases. Again, the minimum of the potential is observed at the center of the molecule, now confirming that the leftover electrons remain localized at the deprotonation site. The similar deprotonation effects were reported for porphycene compounds which were identified as σ–type anions and dianions [88].

Combining the results of the experiment and the simulations, it is clear that the electrons that are left after deprotonation remain in the molecule. They are localized in the deprotonation sites within the σ-orbitals of the previous N-H bonds while preserving the π-structure of the molecule. The rigid shift of the orbitals, that was discussed before in Fig.3.7 and is confirmed by calculations in Fig.3.10, is attributed to the change of the molecular ionization energy due to the presence of the electric field generated by the excessive charge.

3.3 Influence of the localized internal charge on STML spectra

3.3.1 Comparison of the fluorescence spectra

In the previous sections it was concluded that the excess charges remain in the molecule where they generate an electric field. It is of interest now to discuss whether this field

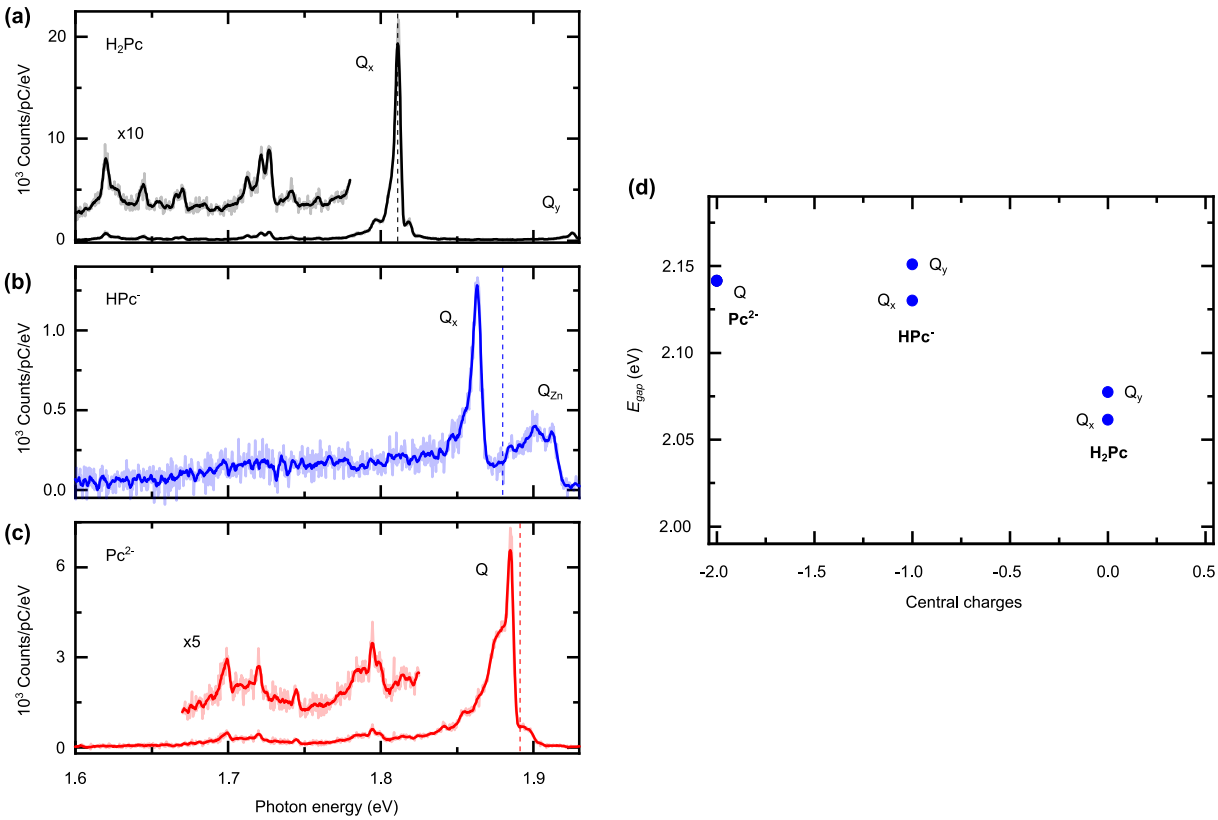

Figure 3.11: **Comparison of the fluorescence spectra.** STML spectra (acquisition time t = 120 s) of **(a)** H_2Pc (I = 100 pA, V = -2.5 V), **(b)** HPc^- (I = 60 pA, V = -2.5 V), and **(c)** a Pc^{2-} (I = 100 pA, V = 2.5 V) on 3ML NaCl/Ag(111). The spectrum of HPc^- was obtained by resonant energy transfer from a neighbouring ZnPc. **(d)** TD-DFT absorption energies calculated for H_2Pc, HPc^-, and Pc^{2-}. For convenience, the same energies are plotted in **(a)-(c)** as dashed lines. A rigid shift is applied to TD-DFT calculations in such a way that the calculated value of absorption energy of H_2Pc is aligned with experimentally recorded peak.

affects the fluorescent properties of the chromophore. In Fig.3.11 the STML spectra of the three molecules are presented. One can see the spectrum of H_2Pc in Fig.3.11a, the spectrum of HPc^- excited via energy transfer from ZnPc in Fig.3.11b and the spectrum of Pc^{2-} in Fig.3.11c. All three spectra were presented previously in the chapter. Plotting the spectra in the same axis allows to see how the 0-0 emission line shifts upon the deprotonation of the molecule. After the first deprotonation, the emission energy of H_2Pc shifts by 50 meV to higher energy. The second deprotonation shifts the main peak even further, by 20 meV.

In order to determine the origin of the non-linear blue shifts of the emission, TD-DFT absorption energies were calculated by our theoretician collaborators for the three molecules. In the calculations of the deprotonated species, the proton of the hydrogen atoms were removed and the geometries were not relaxed. The results of the calculations are given in Fig.3.14 in blue dots. The same results are plotted as the dashed line for each molecule in Fig.3.11 with a rigid shift of -250 meV to align the calculated absorption

energy of H_2Pc with experiment. The calculated absorption energy of Pc^{2-} is in a good agreement with experiment, which can be seen from an almost coincident position of the main peak and the dashed line. One can see, however, that the calculations of HPc^- has a certain disagreement with experiment, which might be caused by the presence of the nearby molecule during experimental spectra acquisition. Nevertheless, the non-linear dependency of the shifts of experimental peaks is well reproduced by calculations.

From the above comparison one can see that the energy of the main transition experiences a non-linear blue shift with the deprotonation. Since the deprotonated molecules contain an excess charge, it is logical to compare with previous studies performed on charged chromophores as π-type phthalocyanine anions and cations [11, 12, 26, 89]. These π-charged molecules are systematically characterized by a strongly red-shifted emission ($\approx$ 400 meV) compared to the neutral compounds, reflecting important modifications of the π-orbitals involved in the optical transition. This is inconsistent with the 50-70 meV shifts reported in the spectra in Fig.3.11. In addition, the DFT calculations of the deprotonated compounds, HPc^- and Pc^{2-}, reveal an unchanged occupancy of the π-orbitals compared to H_2Pc (Fig.3.10), explaining why the fluorescence characteristics of these three "iso-electronic" compounds do not change drastically. Therefore, the shifts observed in the case of deprotonated molecules are caused either by environmental changes upon deprotonation, by changes of the internal structure or by the Stark effect induced by the excess σ-electrons.

3.3.2 Possible origins of the blue shift

Presence of STM tip and neighbouring molecule

Several studies reported that the STM tip generates external static and dynamic electrical fields that induces emission lines shifts due to two effects known as the Stark and photonic Lamb effects [10, 29–32]. However, the reported values of those shifts are in the range of a few meV for H_2Pc, which is an order of magnitude lower than the shifts reported in Fig.3.11. Additionally, the experiments were conducted consistently with exactly the same tip, definitely excluding any tip-related effects on the observed shifts.

The presence of the ZnPc molecule in the STML experiment on HPc^- may also cause a small shift of the emission energy, as was reported in previous studies of the energy transfer between the single molecules [8]. However, the reported values yet again are much smaller than the shifts experienced by the molecule upon deprotonation.

Changes of adsorption site of the molecule on NaCl

In the experiment, the molecules are adsorbed on decoupling NaCl layers. In this configuration, the molecule can be adsorbed on either of the atoms of the crystalline lattice and is mobile enough to move from one adsorption site to another with the aid of STM tip

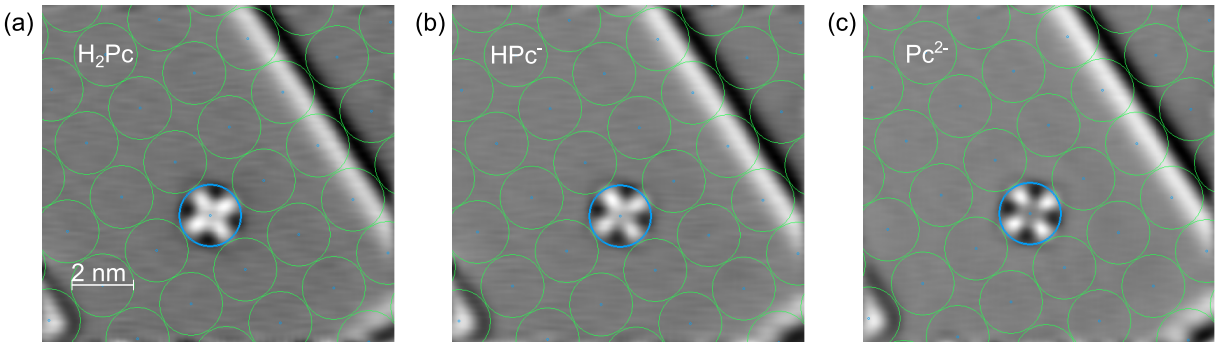

Figure 3.12: **Adsorption site of the molecules on 2ML NaCl layer** The square lattice consisting of 2 nm diameter circles is artificially plotted in the center of **(a)**H_2Pc, **(b)** HPc^-, and **(c)** Pc^{2-} molecules on the topographical STM images in order to evaluate the position of the molecule with respect to the NaCl lattice.

manipulation. To exclude the adsorption site factor, a comparison of the adsorption site of all three molecule is given in Fig.3.12.The square lattice consisting of 2 nm diameter circles is artificially plotted in the three consecutive images of the molecule before and after deprotonation. The lattices are plotted with the center of the circle aligned on the center of the molecules. These maps show that the position of the molecule is unchanged before and after deprotonation. Therefore the adsorption site influence on the emission energy can be ruled out.

Static screening of NaCl substrate

To verify that the spectral shifts observed for the H_2Pc, HPc^-, and Pc^{2-} molecules do not originate from a modified interaction with the NaCl substrate, study of the influence of the static screening due to the NaCl substrate on the optical properties of the molecules (the energy of the lower excited state) should be conducted [90]. To that end a series of combined DFT and TD-DFT calculations is performed by theoretician collaborators. The following four scenarios are considered:

1. Relaxation of the structures of the different species adsorbed on the Na site of the NaCl layer using Quantum Espresso, as shown in Fig.3.14a-c. Subsequently, a TD-DFT study of the vertical excitation energies is conducted for these molecules relaxed on the substrate and include the Na (Cl) atoms as external positive (negative) static point charges. The results are shown as full red dots connected by a full red line in Fig.3.14g.

2. The geometries of the molecules relaxed on the substrate are used to perform TD-DFT calculations, but the NaCl substrate is not included (shown as full red diamonds connected by red dashed line in Fig.3.14g).

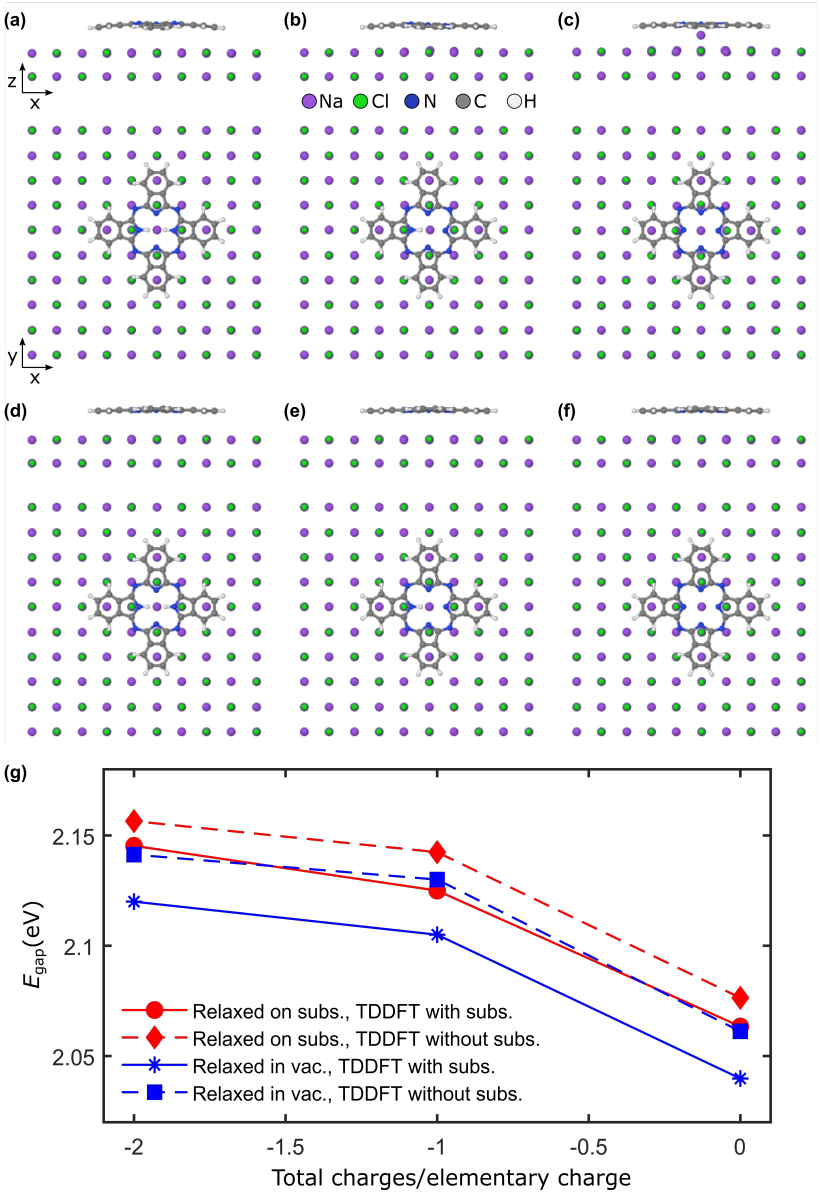

Figure 3.13: **Geometry of H_2Pc, HPc^-, and Pc^{2-} on two monolayers of salt and corresponding TD-DFT vertical transition energy gaps.** **(a)** H_2Pc, **(b)** HPc^-, and **(c)** Pc^{2-} whose geometries have been relaxed together with the top monolayer of NaCl using Quantum Espresso. **(d)** H_2Pc, **(e)** HPc^-, and **(f)** Pc^{2-} relaxed in the vacuum phase and inserted 0.6 nm above the top NaCl layer. The geometry of the NaCl substrate in **(d)-(f)** was not relaxed together with the respective molecules and is identical to the one shown in **(a)**. **(g)** Molecular geometry relaxed on the NaCl substrate, combined with TD-DFT considering the substrate (red circles) and not considering the substrate (red diamonds); molecular geometry relaxed in vacuum, combined with TD-DFT considering the substrate (blue stars) and not considering the substrate (blue squares).

3. Next, the molecular geometries are relaxed in gas phase and in TD-DFT calculations the substrate is included as external point charges considering the geometry shown in Fig.3.14d-f. In this geometry, the molecule is 0.6 nm above the surface of the NaCl substrate. The substrate geometry for all adsorbed molecules (H_2Pc, HPc^-,

and Pc^{2-}) is considered identical to the NaCl geometry obtained for H_2Pc adsorbed on NaCl in scenario 1. The results are shown as blue stars connected by a full blue line in Fig.3.14g.

4. Finally the TD-DFT calculations of the molecules are performed considering their geometries fully relaxed in gas phase and not considering the substrate. The result is presented as full blue squares connected by blue dashed line in Fig.3.14g.

One can see that the presence of the substrate in the calculations of the excitation energies induces not blue, but red shifts. This is true for both cases of molecules relaxed either on substrate or in vacuum. In addition, the overall non-linear dependency is consistent in each of the considered scenario. With that it is possible to conclude that the substrate induces only a minor red shift of the vertical optical transition energy of the molecules, but does not explain the non-linear blue shifts observed in the experiment.

Structural reorganization of the molecule after deprotonation

In the calculations of Fig.3.13, the molecules were relaxed each time after deprotonation. The structural reorganizations that occur during relaxation might be the source of the observed blue shifts. To address this issue, another series of calculations is conducted by our collaborators. The fully symmetric Pc^{2-} molecule is progressively neutralized by artificially adding partial positive charges in its center (shown as a red dot in the inset of Fig.3.14). For each partial charge added, the molecule is not relaxed and the geometry is unchanged. The evolution of the optical gap is then calculated as a function of the molecular charge. The results of the calculations are given in Fig.3.14 as white dots.

These simulations show that the optical gaps of HPc^- and H_2Pc scale extremely well with those of Pc^{2-} with one and two central positive charges, respectively. The non-linear dependency, similar to the one of TD-DFT calculations, appears to be a parabola. The absorption energy is at its maximum when the molecule has -1.5 partial central charge. The results of the calculations are fitted well with a parabolic function with parameters given in the inset of Fig.3.14. The reported calculations eventually demonstrate that the observed shifts are not caused by structural reorganizations of the molecule upon deprotonation, but by the leftover charge itself.

3.4 Internal Stark effect

Since the external sources and structural reorganizations were ruled out, the only remaining cause for the observed blue shifts lies in the excess σ-electrons that remain in the molecule upon deprotonation. The shifts of the absorption energies due to the presence of external electric field is known as Stark effect.

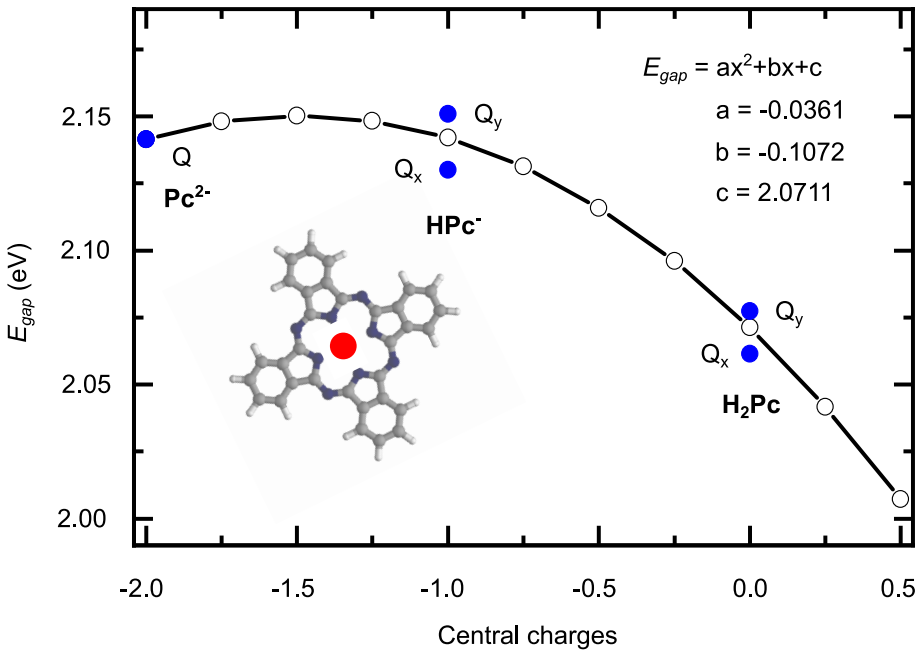

Figure 3.14: **ISE of fluorescence of neutral and charged phthalocyanines.** Comparison between TD-DFT absorption energies calculated for H_2Pc, HPc^-, and Pc^{2-} (blue dots) and TD-DFT absorption energies calculated for a Pc^{2-} as a function of partial positive charges added artificially in its center (white dots). The line through the white dots is a parabolic fit with the parameters given in inset. The position of the artificial point charge is shown as a red dot in the inset.

In the usual case of a chromophores with non-degenerated electronic states placed in a homogeneous external electrical field, the linear and quadratic Stark effects reflect the respective changes in the permanent dipole moment, $\Delta\vec{\mu}$, and in the polarizability, $\Delta\alpha$, experienced by the ground and excited states of the chromophore[28]. However, ground and excited states of the H_2Pc do not exhibit permanent dipole moments ($\vec{\mu}_{S_0} = \vec{\mu}_{S_1} = \vec{0}$). In this case, the energy shifts caused by the Stark effect are expected to be only of a quadratic character. This is not consistent with the reported presence of a non-vanishing linear term in the calculations of Pc^{2-} (see inset of Fig.3.14 for fit parameters). Additionally, it may appear surprising to observe a much smaller relative shift (+20 meV) upon removal of the second proton compared to the first deprotonation (+50 meV).

Unlike the model case of a chromophore in a homogeneous external electrical field, in the case of the deprotonated molecules the excess electrons are localized in the σ-orbitals close to the "center" of the molecule. This constitutes a specific system where central charges generate a strongly non-homogeneous electric field with respect to the molecular scale. This non-homogeneity eventually results in a linear contribution to the Stark shift of the spectral line. This effect is referred to as the Internal Stark effect (ISE). Clearly evidenced in our model system, this "local" effect is inherent to any ISE configuration, including the most complex biological ones, and constitutes the main difference with the usual Stark effect generated by an external electric field.

Influence of charge on vibronic behaviour of the molecules

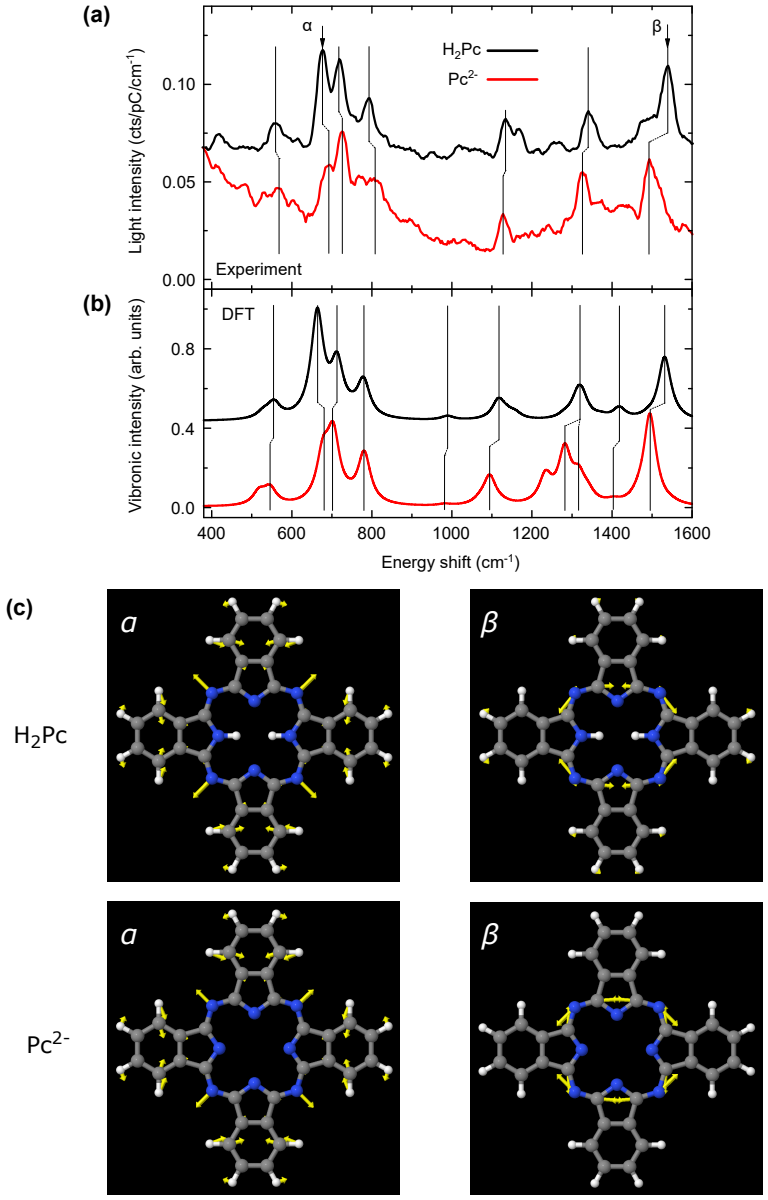

Figure 3.15: **Effect of the deprotonation on the vibronic signature of the phtahlocyanine molecule. (a)** STML vibronic spectrum (I = 100 pA, acquisition time t = 120 s) of H_2Pc (V = -2.5 V) and Pc^{2-} (V = 2.5 V) molecules on 3ML of NaCl compared with **(b)** theoretical vibronic intensities calculated for the molecules in vacuum. The Q_x-line of H_2Pc and Q-line of Pc^{2-} are used as the origin of the experimental energy scale. α and β indicate vibronic modes for which the four nitrogen atoms of the pyrrole cycles stand nearly still. **(c)** Modes of interest of H_2Pc and Pc^{2-} species, labeled as α and β, simulated to see the exact atom movements. Yellow arrows indicate movements of atoms, that take part in those particular vibrational modes. This clearly indicates that the four central N atoms, bonded with H atoms participating in deprotonation, are not moving.

In the fluorescent spectra of the studied chromophores, vibronic emission lines were observed (see Fig.3.11). Even though they are not resolved for HPc^- due to low intensity

of the overall spectra, H_2Pc and Pc^{2-} spectra display several vibronic emission lines that can be compared. Those lines, similar to tip-enhanced Raman spectra, can be used as accurate chemical fingerprints of the probed compounds, and provide detailed information regarding their chemical bond structures [6]. The spectra of those vibrations are presented in Fig.3.15a. One can see that several vibronic peaks of H_2Pc experience subtle changes of their intensity and energy for its doubly deprotonated counterpart. These changes can indicate either a shift of the mode frequency or the appearance/disappearance of vibronic peaks. To investigate these changes, DFT calculations of the vibronic active modes for the two compounds were performed by our theoretician collaborators. The results of the calculations are given in Fig.3.15(b). One can see that the calculations reproduce the experimental frequencies and peak intensities remarkably well. The use of atomic-coordinate displacements provided by DFT allows to identify the prominent modes of H_2Pc and of Pc^{2-}. The black vertical lines in Fig.3.15b indicate the modes that have a nearly perfect one to one correspondence. Experimentally, while the modes below 900 cm^{-1} all shift to higher wavenumbers upon double deprotonation of H_2Pc, those above 900 cm^{-1} display the opposite behavior. Numerically, only one of the low wavenumber modes (α) clearly blue shifts, while the experimental trend in the high wavenumber modes is better accounted for.

The two shifts that are well reproduced by the numerical simulations, both in amplitude and sign, are those of the strongest peak close to 700 cm^{-1} (α in Fig.3.15) and the highest wavenumber mode around 1500 cm^{-1} (β in Fig.3.15). Fig.3.15c demonstrates the real-space representation of the two corresponding modes. One can see that, for both modes, the four nitrogen atoms of the pyrrole cycles stand nearly still. That means that the central hydrogens, as well as the central protons, do stay still as well. This real-space representation shows that the frequency shifts of these two modes cannot be explained by an isotopic-like effect associated to deprotonation. Their shifts must therefore be attributed to a polarization of the π-electron system upon removal of the inner proton.

To conclude, these two modes may be considered as undergoing pure vibrational ISE. Most of the other modes entail radial motions of the nitrogen of the isoindoles. Therefore, the respective influence of the vibrational ISE and of isotopic effects induced by the removal of the central protons cannot be disentangled.

Conclusion

The chapter reports a successful $in-situ$ chemical modification of the H_2Pc/NaCl/Ag(111). The proposed procedure allows to deprotonate a single H_2Pc molecule in a controllable fashion by simultaneously preserving the π-orbital structure of H_2Pc and leaving an excess σ-electron within the chromophore. The investigation of the deprotonated species reveals several important changes in the molecule. First, the deprotonation causes a change of

tautomerization of the central hydrogens. For the same values of bias and current, the switching rate of tautomerization of HPc^- is much higher. Second, the deprotonation causes shifts of the electronic gap of the molecule. Because an excess electrons remain in the system, the electronic gap shifts in rigid manner for each species. Finally, the emission energy observed in STML spectra of the molecules experiences a non-linear blue shift with each deprotonation step. With the help of theory, the corresponding absorption energies are calculated and return a good agreement with the experimental observations. The influence of the environment and the structural reorganizations was ruled out as the cause of the emission energy shifts. The DFT calculations performed on a relaxed Pc^{2-} molecule with fixed geometry return a parabolic dependency with the number of extra charges localized in its center. The presence of quadratic term, characteristic of the Stark effect in homogeneous external electric field, is expected. However, H_2Pc molecule does not possess a permanent dipole moment, hence the presence of a linear term attributed to the non-homogeneity of the electric field generated by the localized excess charges in the center of the molecule. Consequently, the observed energy shifts are attributed to an Internal Stark effect (ISE). The influence of ISE on certain vibrational peaks is also evident and confirmed with TD-DFT calculations.

Charged states of single molecules have been recently probed in a wide range of experimental schemes involving scanning probe approaches [11, 12, 24–26, 87, 89]. The experiment proposed here constitutes a new biomimetic strategy, based on the control of the local electrostatic environment, to tune and optimise future artificial molecular optoelectronic devices. This strategy provides a unique opportunity to study the Stark effect generated by an internal charge on the fluorescence emission of an individual chromophore. The resulting σ-type anionic and dianionic molecules constitute model systems allowing to identify the role played by the proximity between a chromophore and a point-like electrostatic field source. This proximity is responsible for the combined linear and quadratic dependency of the emission energy, a behaviour that should occur in any biological systems subject to ISE.

Chapter 4

Excitation mechanism in STML of single molecules

Introduction

In the previous chapter, we reported that the singly-deprotonated molecule HPc^- cannot be excited by injecting carriers directly in the molecular orbitals. For any value of the bias the molecule remained "dark". Making use of the energy transfer mechanism from a neighbouring molecule or from plasmons (see Fig.3.5), was the only way to record the fluorescence of this molecule. However, we could not provide an explanation of the absence of luminescence by direct carrier injection. In the present chapter, an attempt is made to discuss the carrier injection mechanism from another point of view - in the framework of a many-body picture - and figure out the nature of the "dark" behaviour of the HPc^- molecules. This many-body picture of the carrier injection mechanism is then used to re-explain different STML experiments from single molecules reported in the literature.

The chapter begins with a description of the system when the tunneling process takes place on top of H_2Pc molecule in a tunneling junction. The description is made according to a carrier injection mechanism in the framework of a one-particle picture (as was explained in Chapter 2). However, including the precise energy alignment of the molecular orbitals in the diagram reveals a discrepancy between the model and the experimental data.

The chapter continues with a description of the carrier injection mechanism in the framework of a many-body picture. Such a model allows to precisely describe the transport through ion resonances of the molecule, leading to molecular charging. More importantly, this model perfectly explains the excitation of H_2Pc molecule as well as the reason behind the non-luminescent behaviour of HPc^-.

The chapter concludes with a "revision" of two different STML experiments on ZnPc molecules. This part shows the benefits of the many-body picture for the explanation and the understanding of STML experiments.

4.1 Mechanism of excitation of H_2Pc

4.1.1 One-particle model

Excitation with negative bias

Let us consider the STML experiment for H_2Pc molecule deposited on NaCl/Ag(111).

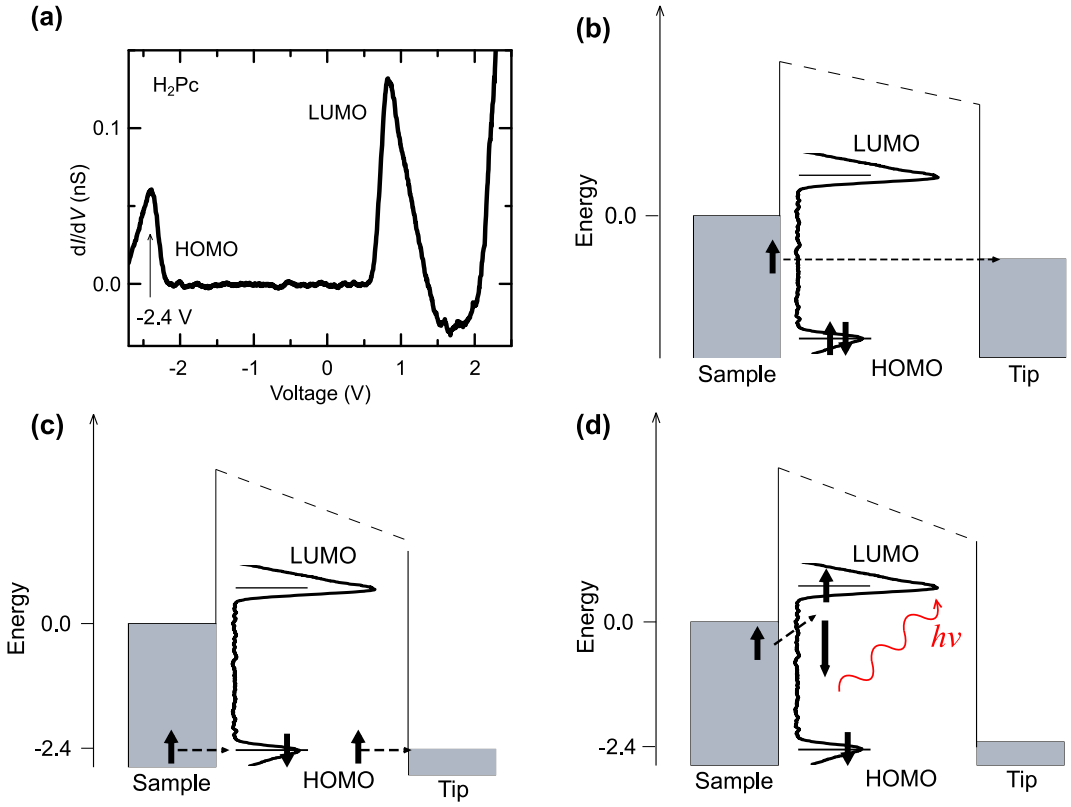

Figure 4.1: **One-particle picture of H_2Pc/NaCl/Ag(111) at negative bias. (a)** $\frac{dI}{dV}$ spectrum acquired on H_2Pc. The arrow indicates the HOMO position at -2.4 V. **(b)** One-particle picture of the STM experiment on top of the molecule. When the Fermi level of the tip is not aligned with the HOMO, the tunneling process takes place in one step. Upon alignment, the tunneling is sequential. The electron from the HOMO leaves the orbital and tunnels to the tip. Sequentially, either **(c)** the HOMO is repopulated with the electron from the substrate, or**(d)** a higher energy tunneling electron populates LUMO, therefore exciting the molecule.

It is possible to schematically describe this system in a one-particle picture (as it was done in chapter 2, Fig.2.10(a)). To be precise, the HOMO/LUMO alignment in the framework of this picture would be deduced directly from the $\frac{dI}{dV}$ spectrum of the molecule (see Fig.4.1(a)). The position of the orbitals with respect to the Fermi level would correspond to position of peaks detected in the $\frac{dI}{dV}$ spectrum. Tunneling events without alignment of the Fermi level of the tip/sample with the HOMO/LUMO of the molecule occur in one step, like shown schematically in Fig.4.1(b).

Next, let us consider the tunneling through the molecule with negative bias corre-

sponding to the alignment of the Fermi level of the tip with HOMO ($V \approx -2.4$ V). The tunneling process in this case is directed from the sample to the tip. Firstly, the electron of HOMO tunnels from the orbital to the tip. Then, HOMO is repopulated by an electron from the sample. The scheme of that process is given in Fig.4.1(c). This is a sequential tunneling process through HOMO of the molecule, however in this process the molecule does not go into an excited state. For that, the higher energy electron has to tunnel into the LUMO, as shown in Fig.4.1(d). However, even with the "HOMO alignment" condition met, one can see that a rigid one-particle picture cannot explain and represent the population of LUMO (hence molecule excitation) at negative bias.

Excitation with positive bias

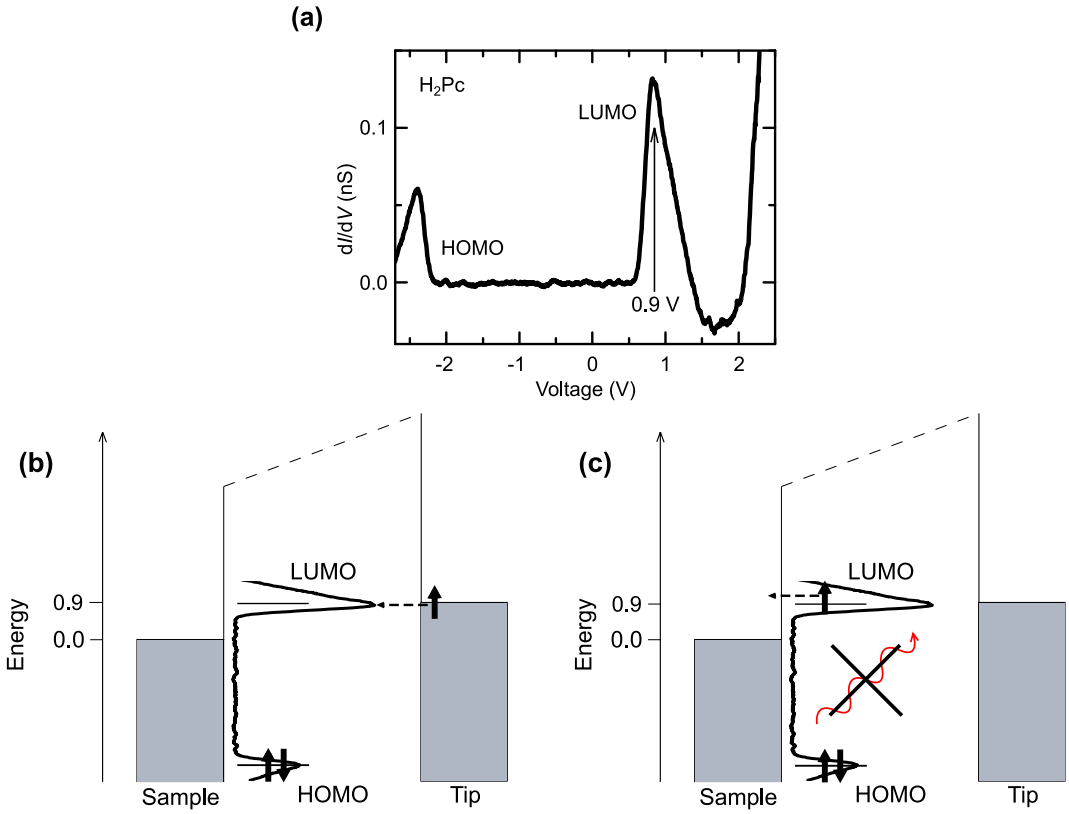

Figure 4.2: **One-particle picture of H_2Pc/NaCl/Ag(111) at positive bias. (a)** $\frac{dI}{dV}$ spectrum acquired on H_2Pc. The arrow indicates the position of LUMO at 0.9 V. **(b)** One-particle picture of the STM experiment on top of the molecule. First, the electron from the tip populates the LUMO of the molecule. **(c)** Second, the electron from the LUMO tunnels to the substrate.

Now, let us consider tunneling through the molecule at positive bias, when the Fermi level of the tip is aligned with LUMO ($V \approx 0.9$ V). In this case, the sequential tunneling process is directed from the tip to the sample. First, the electron from the tip populates the LUMO of the molecule (Fig.4.1(b)). Then, the electron from the LUMO tunnels to the sample (Fig.4.1(c)). Even though the orbital alignment condition is met, the light

emission is not observed while tunneling through the LUMO of H_2Pc.

At this point, discrepancy between one-particle picture and the data is clear. The energy alignment condition at negative bias leads to STML of the molecule, however, representation of the LUMO population, leading to the excitation of the molecule, in the framework of one-particle picture is impossible. Meeting the alignment conditions with LUMO at positive bias also does not lead to STML. These two points demonstrate that the one-particle model does not allow to explain the excitation process leading to fluorescence of H_2Pc/NaCl/Ag(111). Therefore, another approach is needed, and we propose a mechanism based on a many-body picture [91–93].

4.1.2 Many-body model

Excitation with positive bias

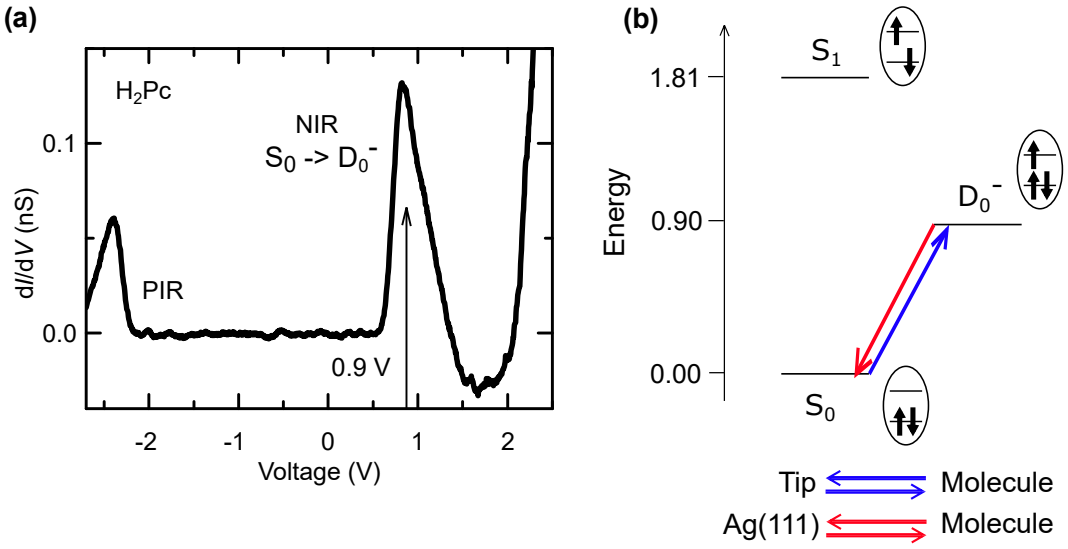

Figure 4.3: **Many-body picture of H_2Pc excitation with positive bias. (a)** The $\frac{dI}{dV}$ spectrum acquired on H_2Pc/NaCl/Ag(111). The energy alignment of the charged states is based on the position of the peaks in the spectrum. **(b)** Many-body picture of the molecular states. At bias corresponding to the NIR ($V = 0.9$V) a transition $S_0 \rightarrow D_0^-$ can occur. The electron tunnels from the tip to the LUMO, bringing the molecule to a negatively charged state (blue arrow). As can be seen from the energy alignment, the only neutralization path for this state is by tunneling of electron from the LUMO to the substrate (red arrow $D_0^- \rightarrow S_0$).

To correctly address the excitation mechanism, the model focuses on the accessible molecular states rather than on the energy diagram of the tunneling junction. Besides, the detailed electronic configuration of each many-body state of the molecule is provided.

In Fig.4.3(a) a $\frac{dI}{dV}$ spectrum acquired on H_2Pc is presented. In the framework of the many-body picture, we interpret the $\frac{dI}{dV}$ peaks as a positive and a negative ion resonances (PIR and NIR). For the positive bias, the resonance is located around 0.9 V. The many-body diagram shown in Fig.4.3(b) shows how the molecule can be driven from a neutral

state S_0 into a negatively charged state D_0^- at a positive voltage $V = 0.9$V (blue arrow $S_0 \rightarrow D_0^-$). The charged state is negative due to the excess electron tunneling from the tip to the LUMO of the molecule, as can be seen from the many-body state representation of D_0^-.

The excited state of the molecule S_1 is also represented in Fig.4.3(b). Bringing the molecule to the excited state would result into an exciton formation and consequent decay into a plasmonic mode of the cavity ($S_1 \rightarrow S_0$). Knowing that, the energy of this excited state can be assigned to 1.81 eV, which corresponds to the detected far-field photon energy. However, the energy alignment of the negatively charged state D_0^- with respect to the excited state S_1 indicates that this path is impossible. The only neutralization path of this charged state is back to a neutral state of the molecule S_0 by the excess LUMO electron tunneling to the sample (red arrow $D_0^- \rightarrow S_0$).

Excitation with negative bias

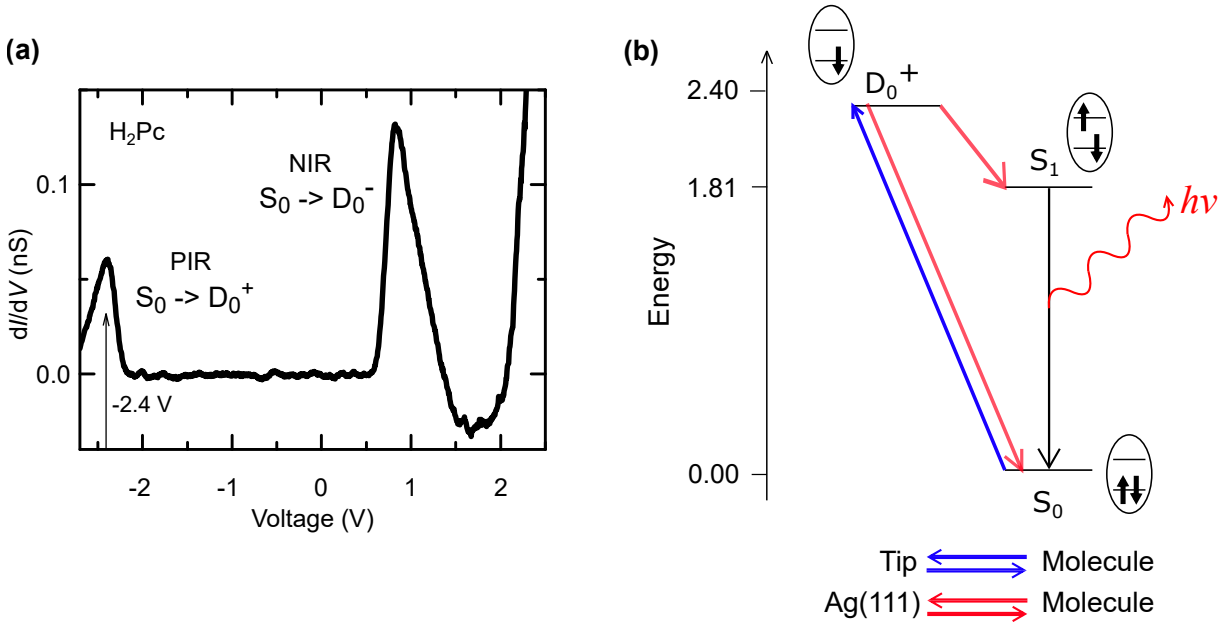

Figure 4.4: **Many-body picture of H_2Pc excitation with negative bias. (a)** $\frac{dI}{dV}$ spectrum acquired on H_2Pc/NaCl/Ag(111). **(b)** Many-body picture of the molecular states. At bias corresponding to PIR, the HOMO of the molecule is depopulated by electron tunneling to the tip. The molecule becomes positively charged (D_0^+). The first possible neutralization path for the molecule is to receive an electron from the substrate to repopulate the HOMO, bringing back the molecule to the ground neutral state. The second path correspond to tunneling of an electron from the substrate to the LUMO, hence exciting the neutral molecule. The energy scale is based on the experimental values of the resonances obtained from $\frac{dI}{dV}$ spectrum.

For the negative bias around -2.4 V (as can be seen from Fig.4.4(a)), the previously assigned HOMO corresponds to a positive ion resonance. At a bias $V = -2.4$V an electron can tunnel from the HOMO of the molecule to the tip, leaving the orbital unfilled and

bringing the molecule to a positively charged state D_0^+. This process is schematically represented in Fig.4.4(b) as a blue arrow $S_0 \rightarrow D_0^+$.

From this point, one can see two neutralization paths of the positively charged state. One path corresponds to repopulation of HOMO by a tunneling electron from the sample (red arrow $D_0^+ \rightarrow S_0$). This path is non-radiative. A second neutralization path corresponds to an injection of charge into the LUMO, leaving the molecule to a neutral excited state (red arrow $D_0^+ \rightarrow S_1$). The molecule can now radiatively decay to the ground neutral state $S_1 \rightarrow S_0$ by emitting a photon of the energy of the excited state (see inset image adapted from Fig.3.2).

4.2 Mechanism of excitation of HPc^- and Pc^{2-}

4.2.1 Excitation of HPc^-

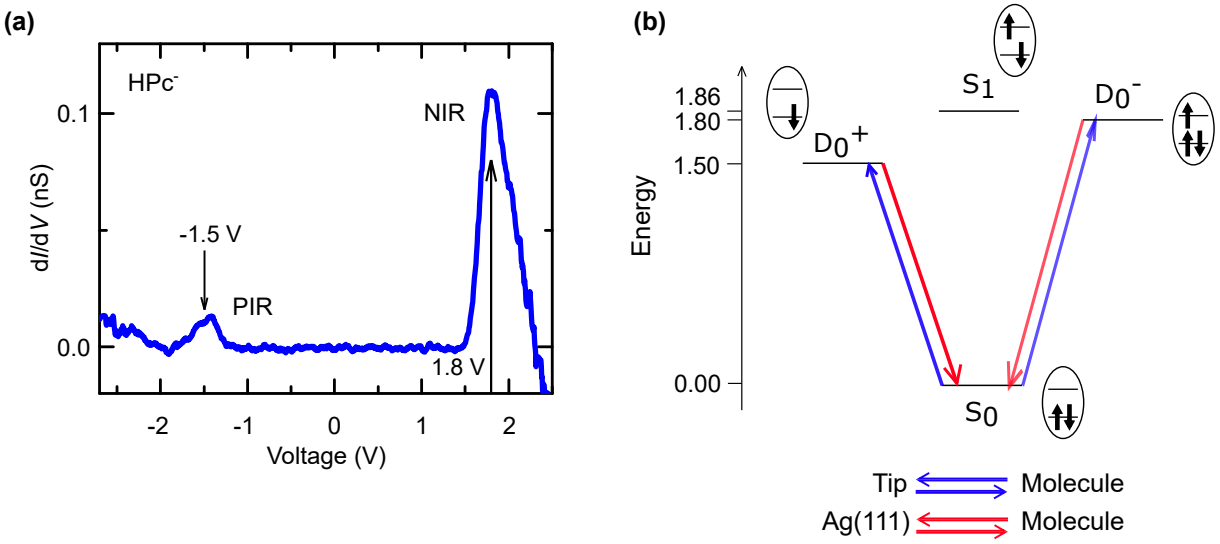

Figure 4.5: **Many-body picture of HPc^- excitation. (a)** $\frac{dI}{dV}$ spectrum acquired on HPc^-. **(b)** Many-body picture of the molecular states. The negatively charged state D_0^- is accessible at positive bias of 1.8 V (blue arrow $S_0 \rightarrow D_0^-$) by an electron injection in LUMO. The positively charged state D_0^+ is accessible at negative bias of -1.5 V (blue arrow $S_0 \rightarrow D_0^+$) by an electron extraction from HOMO. However, both charged states have only one neutralization path to S_0 (red arrows). The energy scale is based on the experimental values of the resonances obtained from the $\frac{dI}{dV}$ spectrum.

The previous section showed that the many-body picture of the molecular states allows to efficiently describe the sequential tunneling processes and indicate the state of the molecule at each step. Additionally, this model clarifies which states are responsible for the molecule excitation and if the excitation is possible at all.

With that being said, it is possible now to address the "dark" HPc^- molecule. In Fig.4.5(a) a $\frac{dI}{dV}$ spectrum acquired on HPc^- is presented. Using the position of the resonances from this spectrum, it is possible to sketch a many-body picture of the molecule.

This picture is shown in Fig.4.5(b). One can see that the two charged states of the molecule have a nearly identical absolute energy in this case.

The negatively charged state D_0^- is accessible at positive bias of 1.8 V, corresponding to the injection of an electron from the tip into the LUMO (blue arrow $S_0 \rightarrow D_0^-$). The positively charged state D_0^+ is accessible at negative bias of -1.5 V, corresponding to the extraction of an electron from the HOMO to the tip (blue arrow $S_0 \rightarrow D_0^+$). However, the sketch shows that both of the charged states have no neutralization paths into S_1, which is located at a higher energy than the charged states (1.86 eV, see Fig.3.11(b)). The only path is back to S_0, by electron tunneling from the LUMO to the sample for the negatively charged state (red arrow $D_0^- \rightarrow S_0$) and from the sample to the HOMO for positively charged state (red arrow $D_0^+ \rightarrow S_0$). This absence of a neutralization path into the excited state S_1, now evident within this many-body picture, explains the "dark" behaviour of HPc^-, reported in the previous chapter.

4.2.2 Excitation of Pc^{2-}

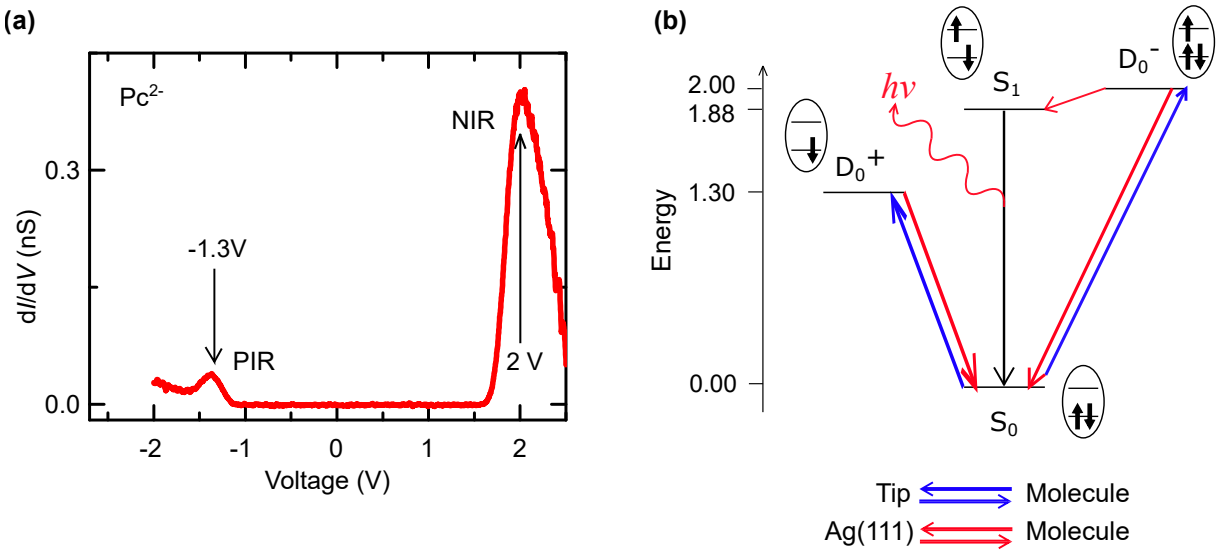

Figure 4.6: **Many-body picture of Pc^{2-} excitation. (a)** $\frac{dI}{dV}$ spectrum acquired on Pc^{2-}. **(b)** Many-body picture of the molecular states. The negatively charged state is accessible at a positive bias of 2 V (blue arrow $S_0 \rightarrow D_0^-$). The positively charged state is accessible at a negative bias of -1.3 V (blue arrow $S_0 \rightarrow D_0^+$). While the positively charged state has only one neutralization path (red arrow $D_0^+ \rightarrow S_0$), the negatively charged state has two paths: into the ground state (red arrow $D_0^- \rightarrow S_0$) or into the excited state (red arrow $D_0^- \rightarrow S_1$) of the molecule.

The last molecule of the series, Pc^{2-}, is reported to have an emission energy $S_1 \rightarrow S_0$ equal to 1.88 eV (see Fig.3.11(c)). The luminescence is recorded at positive bias $V = 2$ V. Knowing that, it is of interest to see if the many-body model can picture the excitation path through D_0^- state.

To extract the energy positions of the charged states, the $\frac{dI}{dV}$ spectrum acquired on Pc^{2-} is used (see Fig.4.6(a)). The PIR is located at -1.3 V and the NIR is located at 2 V. Those two charged states are schematically presented with respect to the excited state of the molecule in Fig.4.6(b). The positively charged state is located at 1.3 eV and evidently cannot be neutralized into an excited state of the molecule (hence, no fluorescence at a negative bias). However, the negatively charged state is located at a higher energy (at 2 eV) than the neutral excited state of the molecule ($S_1 \rightarrow S_0 = 1.88$ eV). This leads to a possibility to excite the molecule by neutralization of the negatively charged state (blue arrow $D_0^- \rightarrow S_1$ in Fig.4.6(b)).

4.2.3 Summary

A side-by-side comparison of this many-body representation for the three molecules is given in Fig.4.7. Using this model, it is possible to evidently describe the carrier injection

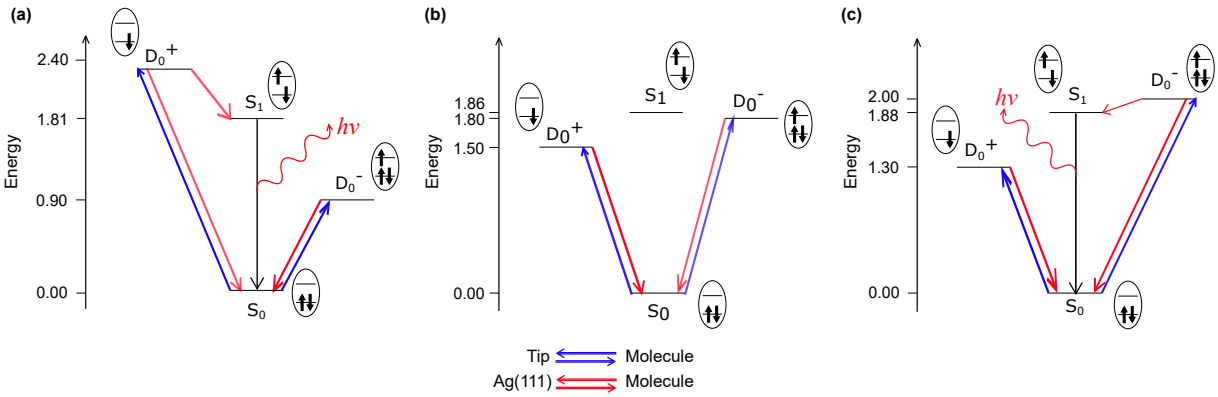

Figure 4.7: **Comparison of many-body picture diagrams.** Energy diagrams of **(a)** H_2Pc, **(b)** HPc^- and **(c)** Pc^{2-}.

processes that brings the molecules into different charged states. More importantly, the many-body picture allows to identify the possible transitions that will lead to a radiative decay, hence fluorescence. In the case of H_2Pc, HPc^- and Pc^{2-} the established model allows to confirm that, for STML to occur by carrier injection, the relative position of the excited state in the energy scale must be lower than the position of the charged states ($h\nu \leq |E_{resonance}|$). In other words, the excited state of the molecule must be reachable by a neutralization process from the charged state.

Uncertainty of the resonance energy

One important point that has to be addressed is the uncertainty in the determination of the exact energy of the resonances obtained experimentally. This uncertainty is due to the very broad character of the PIR and NIR in $\frac{dI}{dV}$ spectra.

For example, the exciton energy of HPc^- equals to 1.86 eV and it is confirmed that the molecule cannot be excited by a carrier injection mechanism. However, the $\frac{dI}{dV}$ spec-

trum of the molecule (see Fig.4.5(a)) shows that the experimentally recorded negative ion resonance of the molecule "covers" this energy, because the broad peak spans from approximately 1.5 V to 2.3 V. A similar issue can be observed for Pc^{2-}. Even though the molecule can be excited by tunneling electrons at a positive bias, the onset of the negative ion resonance is located at 1.6 V. This value is significantly lower than the exciton energy of Pc^{2-} that is equal to 1.88 eV.

To conclude on this point, the topic of uncertainty of an energy position of resonances (or charged states) should be addressed in the future. Here, the energy position of a resonance is considered at voltage corresponding to the maximum of peaks in the experimental $\frac{dI}{dV}$ spectrum.

4.3 Mechanism of excitation of ZnPc

Now that the mechanism of excitation of H_2Pc and its deprotonated subspecies was described in details, it is of interest to use the same model to explain STML data obtained on different molecules and address the influence of a choice of substrate for STML experiments. For that, two separate literature examples are chosen. The first example will cover neutral and charged emission of ZnPc/NaCl/Au(111) [11]. The second example reports the same ZnPc molecule, but on a different substrate NaCl/Ag(111) [12]. Explanation of those two results in the framework of our many-body picture provides some insight on the charged and neutral emission processes and on the role of the metal substrate.

4.3.1 Excitation of ZnPc/NaCl/Au(111) substrate

The first example that is revisited is a work of Doppagne *et al.* published in 2018 [11]. The authors reported STML results obtained on ZnPc/NaCl/Au(111) and interpreted them in the framework of a one-particle picture. The reported STML spectrum, adapted in Fig.4.8(a), was recorded at positive bias $V = 2$ V, which corresponds to the NIR observed in the $\frac{dI}{dV}$ spectrum. The main peak of the spectrum is located at 1.89 eV and labeled X^0. Its energy is characteristic of the single neutral ZnPc fluorescence [5, 6, 29]. However, switching the bias to the negative side ($V = -2.5$ V) changes the STML behaviour as can be seen in Fig.4.8(b). The neutral emission peak X^0 is much less intense then at positive bias. Additionally, a second peak appears at 1.52 eV. This peak is labeled X^+ and is associated by the authors to the emission of a positively charged molecule. Presence of X^+ indicates that an excited charged state must be populated. Here, an important point is the choice of voltage at negative polarity. As one can see from the $\frac{dI}{dV}$ spectrum acquired on ZnPc molecule (see Fig.4.8(c)), the PIR is located at approximately $V = -1$ V which is much higher than the value used to record the STML spectrum. The value $V = -2.5$ V chosen by the authors corresponds to the next positive ion resonance that is seen in the

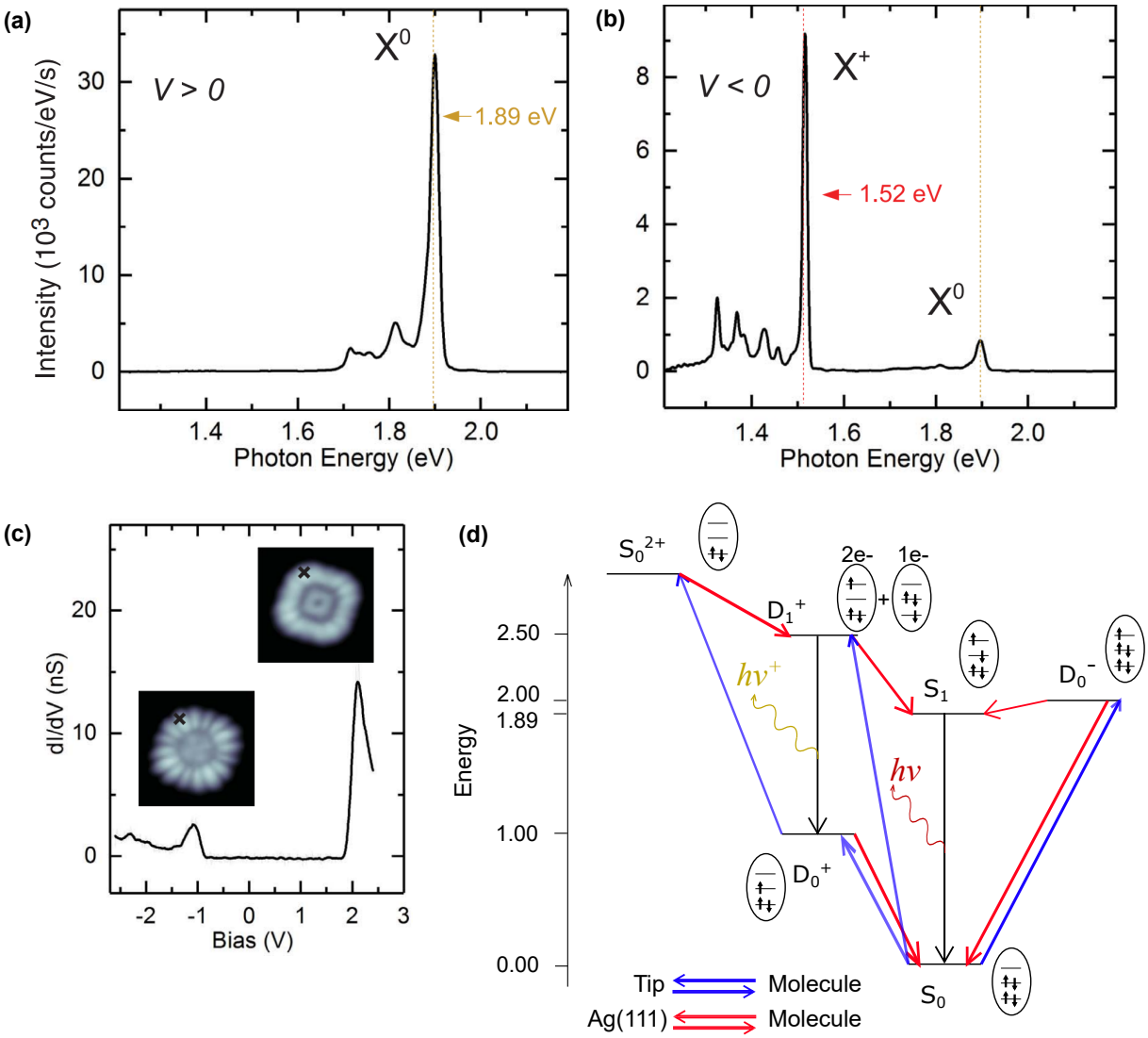

Figure 4.8: **Many-body description of a single ZnPc molecule adsorbed on 3ML NaCl/Au(111). (a)** STML spectrum of a single ZnPc molecule on 3ML NaCl/Au(111) acquired with $V = 2$ V and $I = 300$ pA over $t = 300$ seconds. The peak labeled X^0 located at 1.89 eV corresponds to the neutral emission of the molecule. **(b)** STML spectrum of a single ZnPc molecule on 3ML NaCl/Au(111) acquired with $V = -2.5$ V and $I = 300$ pA over $t = 300$ seconds. The peak labeled X^+ located at 1.52 eV corresponds to the emission of a positively charged molecule. **(c)** A $\frac{dI}{dV}$ spectrum acquired on ZnPc/3ML NaCl/Au(111). The onset of the PIR is positioned at ∼-1 V with resonance maximum at -1.1 V. The onset of NIR is positioned at ∼2 V with resonance maximum at 2.1 V. Figures adapted from [11] **(d)** Many-body description of transport and luminescence for ZnPc/NaCl/Au(111). Red wave-like arrow corresponds to emission of the neutral molecule, yellow wave-like arrow corresponds to emission of the positively charged molecule.

$\frac{dI}{dV}$ spectrum. This indicates that there is another charged state involved in this particular STML process.

The many-body model for ZnPc/NaCl/Au(111) is shown in Fig.4.8(d). The diagram shows the states involved in STML process of both neutral and charged emission. Let us

start with a description of what occurs at positive bias ($V > 0$), which, as reported, leads only to emission of the neutral molecule. The negatively charged state D_0^- is located at 2 eV on the energy scale. This position is higher than that of the neutral excited state S_1. Therefore, D_0^- can be neutralized into a neutral excited state S_1. This many-body description is in agreement with the STML results reported by the authors.

Excitation with a negative bias occurs for negative voltages ($V < 0$) that are much lower than the first ion resonance. The first PIR located at -1 V corresponds to a transition $S_0 \rightarrow D_0^+$. One can see from our many-body diagram that, due to the energy alignment of the states, the only neutralization path for D_0^+ is back to a neutral ground state S_0. However, the presence of "another" resonance in the $\frac{dI}{dV}$ spectrum around -2.5 V and the presence of X^+ hint towards the presence of another state - an excited charged state of the molecule. This state is required for the radiative decay leading to a charged emission. Such excited charged state is labeled as D_1^+ in Fig.4.8(d). Bringing the molecule into an excited charged state is possible in two paths: a one-electron process and a two-electron process. The many-body orbital population indicated nearby depicts those two different ways.

The one-electron process is depicted by a blue arrow connecting $S_0 \rightarrow D_1^+$. Physically this process consists of an electron extraction from the HOMO-1 orbital to the tip. The two electron process, as comes from the name, takes place in two steps. First, a molecule is brought to a charge state D_0^+ by an electron extraction from HOMO. Then, before this state decays, a second electron of HOMO is extracted to the tip as well, leaving the molecule in a doubly positive charged state S_0^{2+} and an empty HOMO. This two-electron process is depicted by two blue arrows $S_0 \rightarrow D_0^+$ and $D_0^+ \rightarrow S_0^{2+}$. The doubly positive charged state has a decay path into a single positive charged state D_1^+ by population of LUMO with an electron from the sample.

When the molecule is in a singly negative charge excited state, there are two decay paths. One is a radiative decay into a singly charged ground state D_0^+. This process is responsible for the emission of the positively charged molecule observed in the STML spectrum of ZnPc/NaCl/Au(111). Second path is a neutralization towards the neutral excited state S_1, which consequently radiatively decays, thus being responsible for the fluorescence of the neutral molecule. The presence of two decay paths for the excited state of the positively charged molecule explains the presence of both X^+ and X^0 in STML spectrum and the origin of their common voltage onset.

4.3.2 Excitation of ZnPc on Ag(111) substrate

The second example we considered is a work of Dolezal *et al.* published in 2021 [12]. The authors investigate the transport and fluorescence dynamics of neutral and charged ZnPc molecule on NaCl/Ag(111) substrate. They also propose a simple many-body picture to

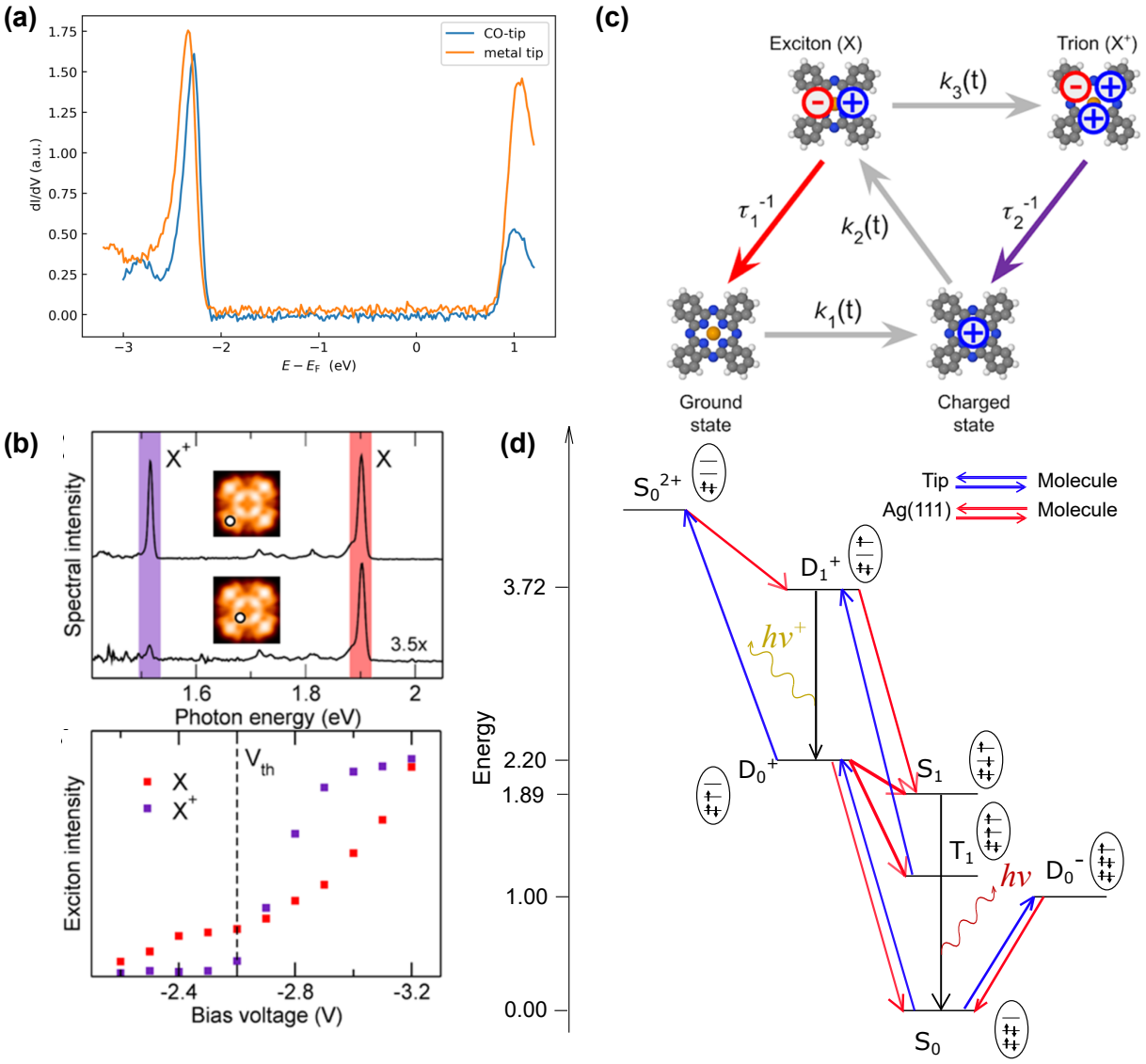

Figure 4.9: **Many-body description of a single ZnPc molecule adsorbed on NaCl/Ag(111). (a)** The $\frac{dI}{dV}$ spectrum acquired on ZnPc molecule. The onset of PIR is positioned at -2.2 V with resonance maximum at -2.4 V. The onset of NIR is positioned at 0.7 V with resonance maximum at 1 V. **(b)** STML spectrum of a single ZnPc molecule on NaCl/Ag(111) acquired with $V = -3$ V and $I = 100$ pA over $t = 180$ seconds. The peak labeled X located at 1.89 eV corresponds to a neutral emission of the molecule. The peak labeled X^+ located at 1.52 eV corresponds to a charged emission of the molecule. Below the STML spectra, a bias dependence of the intensity of two main emission peaks is plotted. **(c)** A many-body description of ZnPc/NaCl/Ag(111) proposed by Dolezal *et al.*. Figures adapted from [12] **(d)** A many-body description of ZnPc/NaCl/Ag(111). Red wave-like arrow corresponds to a neutral emission, yellow wave-like arrow corresponds to a charged emission.

describe the system. The reported STML experiment was performed at negative bias $V = -3$ V (corresponding to a second peak observed in the $\frac{dI}{dV}$ spectrum, see Fig.4.9(a)) with $I = 100$ pA over $t = 180$ seconds. The reported STML spectrum is adapted in Fig.4.9(b). The main peak of the spectrum, labeled X, is located at 1.89 eV and

corresponds to emission of a neutral molecule. The second peak, labeled X^+, is located at 1.52 eV and corresponds to emission of a charged molecule. The authors also report an investigation of the bias dependence of the emission intensity of X and X^+. X has a bias onset at $V = -2.2$ V, which corresponds to the onset of the PIR in the $\frac{dI}{dV}$ spectrum. X^+ has a bias onset at $V = -2.6$ V, only 0.4 V lower than for X. At this voltage a dip between resonance peaks is observed in the $\frac{dI}{dV}$ spectrum. In Fig.4.9(c) the authors propose their explanation of these observations based on a simple many-body picture. The proposed mechanism of a charged exciton formation is based on a two-electron process: first, a molecule is brought to a positively charged state that consequently decays into an excited state of a neutral molecule. Second electron then brings this excited neutral state into an excited charged state.

In Fig.4.9(d) we propose a slightly different many-body interpretation where the energy of the respective states are deduced from $\frac{dI}{dV}$ and fluorescence data. The energy alignment of the negatively charged state D_0^-, accessible at $V \sim 1$ V, clearly has only one neutralization path back to the ground neutral state S_0. At a negative bias, the first resonance that is encountered (located at $V = -2.2$ V) corresponds to the positively charged ground state D_0^+. This state has a neutralization path to the neutral excited state $D_0^+ \rightarrow S_1$, which consequently will radiatively decay by X emission, which is in a good agreement with the investigation of the bias dependence of X performed by Dolezal *et al.*.

The reported energy of X^+ is 1.52 eV, hence this value must represent the energy gap between the ground D_0^+ and excited D_1^+ positively charged states. However, the voltage onset of X^+ occurs at mere 400 mV below the $S_0 \rightarrow D_0^+$ transition, at $V = -2.6$ V. This contradiction together with reported bias dependency of STML hint towards a two electron process of a positively charged state excitation.

From a many-body picture one can see two different paths to bring the molecule to an excited charged state D_1^+ in a two-electron process. Both paths start with a $S_0 \rightarrow D_0^+$ transition. After that, there are two possible options. First, another electron is extracted from the HOMO bringing the molecule to a doubly positively charged state $D_0^+ \rightarrow S_0^{2+}$. Second, the ground charged state D_0^+ decays to a triplet state $D_0^+ \rightarrow T_1$ by extracting an electron from the substrate and populating the LUMO. As T_1 is a long-lived state, this may allow another electron extraction from the HOMO, bringing the molecule into an excited charged state $T_1 \rightarrow D_1^+$.

Upon excitation, the charged state has two decay paths as well - a radiative decay into a ground state $D_1^+ \rightarrow D_0^+$, emitting an X^+ photon, or a much less likely non-radiative neutralization into an excited state of a neutral molecule $D_1^+ \rightarrow S_1$.

Conclusion

An open question left in the previous chapter leads to an improved understanding of the excitation mechanism of single molecules in STML experiments. The many-body model reported here allows to understand the changes in excitation and luminescence behaviour of the deprotonated molecules. Moreover, the model allows to revisit different cases of the literature and reinterpret previously puzzling luminescent features in the framework of different charged states of a molecule. The use of this many-body model allows to visualize how the charged states shift depending on substrate and how this shift affects STML experiments. Successful reinterpretation of the literature reports demonstrates that the proposed model can be readily applied to various STML experiments. This model has been recently applied to other molecules and more complex systems [13, 33, 34].

Eventually, the proposed many-body representation could be further improved by accounting for molecular vibrations and substrate reorganisations that are known to play an important role in the energy of the allowed electronic transitions [24, 94]. Another possible improvement is addressing the exact resonance positions of molecular $\frac{dI}{dV}$ spectrum.

Chapter 5

Relationship between the symmetry of molecules and vibronic emission

Introduction

STM studies conducted on zinc phthalocyanine (ZnPc) molecules, demonstrating various distinctive features of the molecule, including the rotation upon adsorbtion, neutral and charged emission and vibrational spectroscopy, were reported before [5–7, 11, 12, 95]. Unlike H_2Pc molecule discussed in chapter 3, the emission spectra of ZnPc reveal a single main neutral emission peak. This comes from the degeneracy of excited states caused by equivalent (or symmetrical, as it would be addressed in this chapter) axis of the molecule, hence identical dipoles. It is of high interest to lift this degeneracy in order to observe more fine and intense emission lines.

In the current chapter, a study of an *ex-situ* chemically synthesized powder of ZnPc subspecies is reported. The powder was synthesized by our chemistry collaborator Frédéric Cherioux from FEMTO-ST in Besançon. The powder consists of ZnPc molecules with additional benzene rings, resulting into a systematic series that contains molecules ranging from the original ZnPc to ZnPc with four additional rings, also known as zinc naphthalocyanine (ZnNc). The notation for the series is chosen to be ZnPc+n, with n being the number of additional benzene rings. In Fig.5.1(a) a mass spectrum is provided, showing the ratio of the molecules that are present in the powder. One can see that the powder contains a prevailing amount of ZnPc+2 molecules. This is convenient, because ZnPc+2 of $D2_h$ symmetry group is of the most interest for our investigation, since its chemical structure provides the biggest difference between the dipoles oriented along the two molecular axis.

For the experiment, the molecules were thermally evaporated on the 3ML NaCl/Ag(111) substrate as shown in Fig.5.1. Since the powder contains several types of molecules with different mass, a higher temperature of evaporation is required to deposit the "heavier" molecules (molecules with more additional benzene rings). This consequently leads to a very high evaporation rate of the "lighter" molecules and makes experimentally difficult to image and characterize the "heavier" molecules. Nevertheless, a thorough electronic and fluorescence investigation of the full series of molecules is reported here. Taking the model

system of ZnPc as a reference, these results demonstrate changes in electronic structure and emission energies with the successive addition of benzene rings. The symmetry breaking of molecular dipoles degeneracy for asymmetric species induces strong changes in the STML behaviour. The results demonstrate that, with the help of the sub-nanometer precision of the STM, it is possible to selectively excite a desired dipole of the molecule, opening the path to investigate the effect of the tip position on the emission spectra.

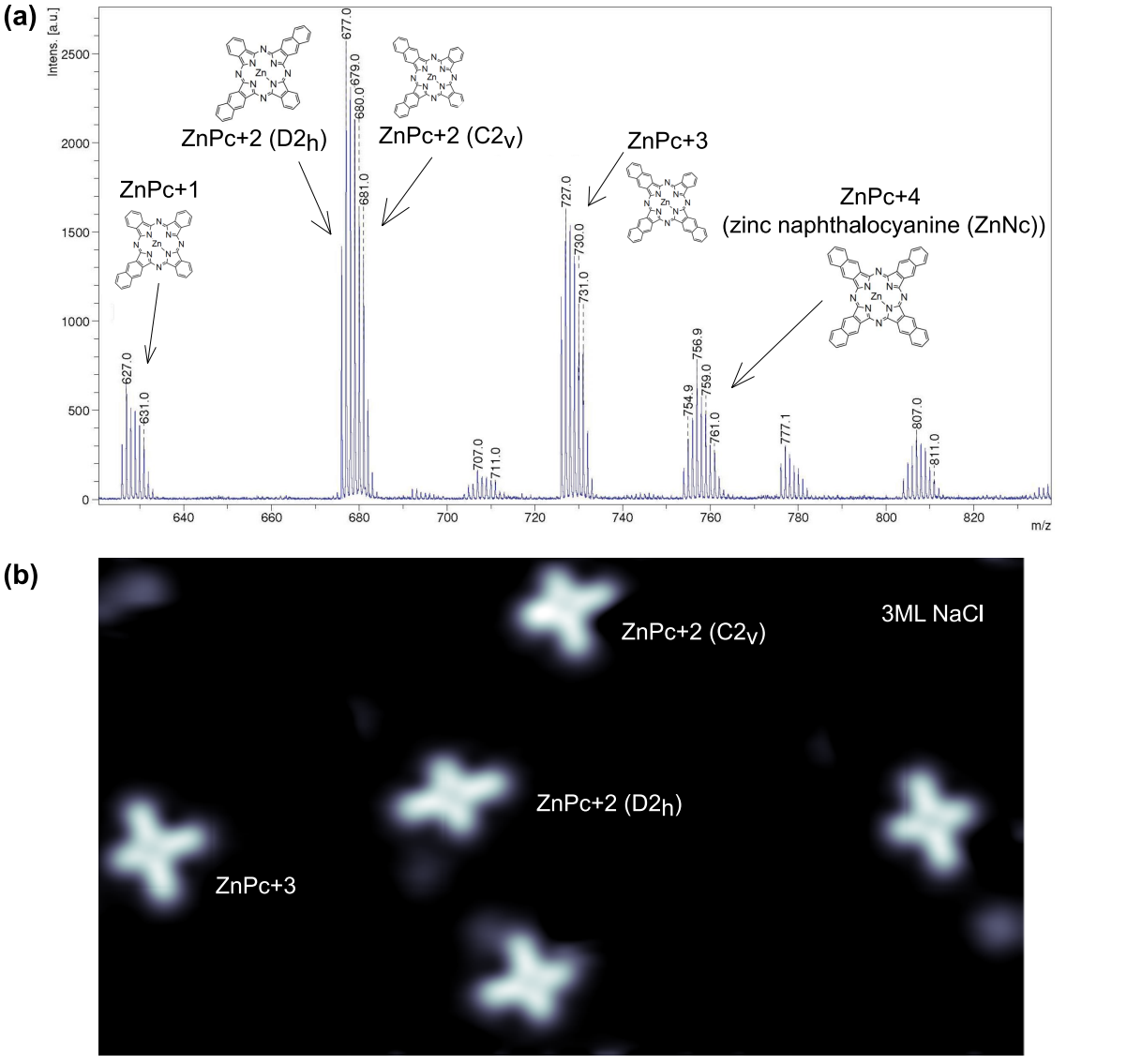

Figure 5.1: **Overview of the system of ZnPc+(1-4)/3ML NaCl/Ag(111). (a)** Mass-spectrum of the original molecular powder. The arrows connecting the mass-spectrum peaks with the chemical sketches of the modified molecules indicate the contribution of the respective molecules. **(b)** 20×7 nm^2 STM image of ZnPc+(1-4)/3ML NaCl/Ag(111).

5.1 Experimental results

5.1.1 Electronic and fluorescence properties of ZnPc molecule

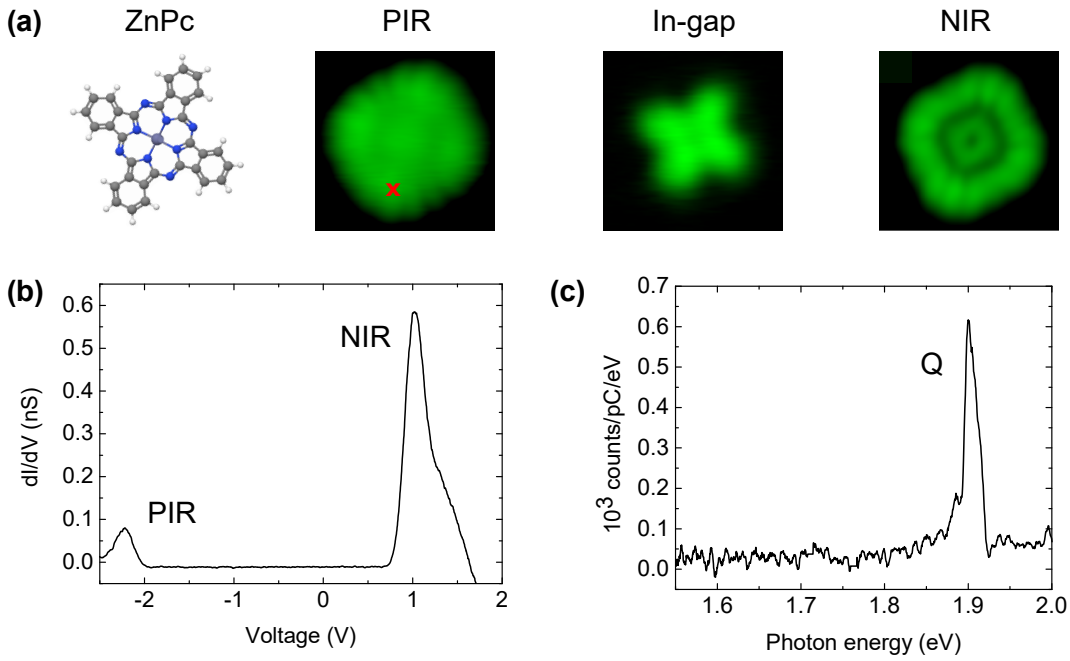

Figure 5.2: **Electronic and fluorescence properties of a single ZnPc molecule.** **(a)** Ball-and-stick model of a ZnPc molecule (white - H, grey - C, blue - N, dark blue - Zn atoms) and 3×3 nm^2 STM images recorded at $I = 10$ pA. The PIR image was recorded at a bias $V = -2.5$ V, the in-gap image was recorded at a bias $V = 0.5$ V and the NIR image was recorded at a bias $V = 1$ V. The red "x" in the PIR image corresponds to the tip position for the $\frac{dI}{dV}$ and the STML spectra acquisition. **(b)** $\frac{dI}{dV}$ spectrum recorded on top of one of the axis of the molecule. The bias is sweeped from -2.5 V to 2 V at constant height. The $\frac{dI}{dV}$ spectra reveals two peaks, one for negative and one for positive bias. The peak at negative bias corresponds to the PIR, the peak at positive bias corresponds to the NIR. **(c)** STML spectrum obtained on the lobe of the molecule. The light emission spectrum was recorded for $t = 180$ s with $I = 100$ pA and $V = -2.5$ V.

In Fig.5.2(a) the ball-and-stick model and STM images of a ZnPc/NaCl/Ag(111) are shown. The first image is recorded at $I = 10$ pA and $V = -2.5$ V, the bias that corresponds to the PIR of the molecule observed in $\frac{dI}{dV}$ spectrum (see Fig.5.2(b)) recorded on top of one of the lobes of the molecule (marked with x in the PIR image). The image reveals a typical 16 lobe structure due to a 22° degree lateral oscillation of the molecule [95]. The middle image is recorded at $I = 10$ pA and $V = 0.5$ V, which corresponds to a non-resonant in-gap regime. It reveals a cross-like pattern that resemble the ball-and-stick model of the molecule. The last image recorded at $I = 10$ pA and $V = 1$ V (corresponding to NIR, see Fig.5.2(b)) reveals the structure of the NIR.

Fig.5.2(c) shows STML spectrum obtained on the molecule. The experiment was performed on top of one of the lobes of the molecule (marked with x in the PIR image)

with $I = 100$ pA and $V = -2.5$ V during $t = 180$ seconds. The light emission spectrum contains a single emission peaks at 1.9 eV (labeled Q). Due to a low intensity of an overall spectrum, the vibronic peaks of ZnPc are not resolved.

For convenience, the dataset obtained on the modified ZnPc molecules will be presented briefly, mentioning only the distinguishing features.

5.1.2 Electronic and fluorescence properties of ZnPc+1 molecule

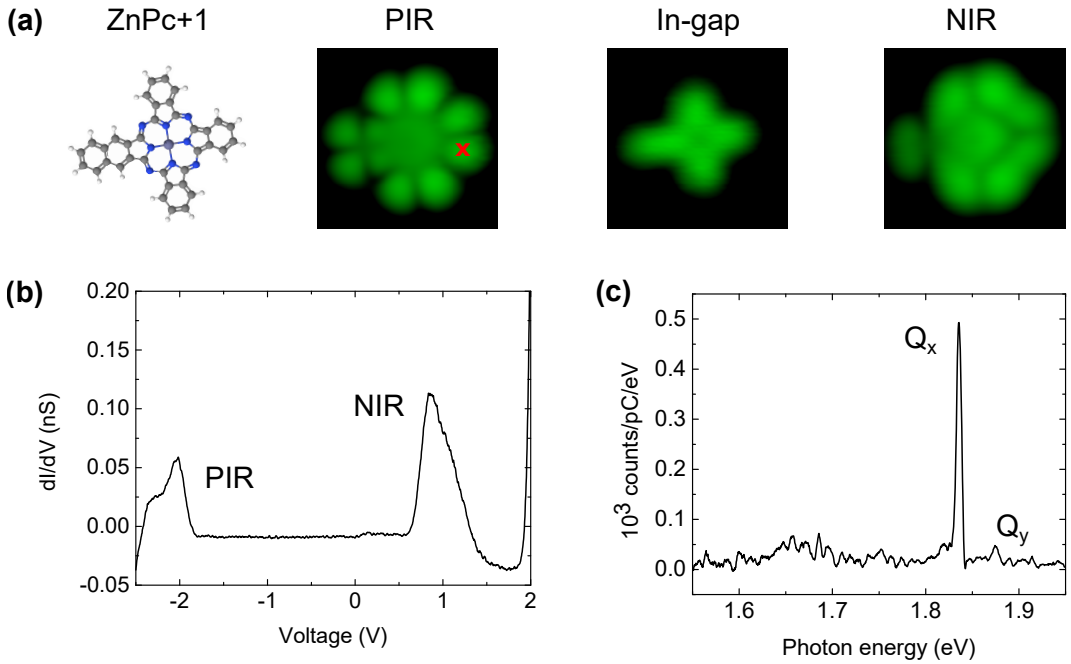

Figure 5.3: **Electronic and fluorescence properties of a single ZnPc+1 molecule.** **(a)** Ball-and-stick model of a ZnPc+1 molecule and 3×3 nm^2 STM PIR($V = -2.3$ V), in-gap ($V = 0.5$ V) and NIR ($V = 1.5$ V) images recorded at $I = 10$ pA. **(b)** $\frac{dI}{dV}$ spectrum of the molecule. **(c)** STML spectrum of the molecule recorded for $t = 180$ s with $I = 200$ pA and $V = -2.2$ V.

Fig.5.3 presents (a) the ball-and-stick model and STM images,(b) a $\frac{dI}{dV}$ spectrum and (c) a STML spectra of a ZnPc+1 molecule. The images reveal that indeed one of the "legs" of the molecule is longer than the rest, confirming the benzene ring addition. The STML spectrum of ZnPc+1, in contrast to that of ZnPc, contains two main emission peaks, a behaviour similar to light emission of H_2Pc. The intense peak at 1.84 eV (labeled Q_x) corresponds to the lowest energy excited state. The weak peak at 1.87 eV (labeled Q_y) corresponds to a higher energy excited state.

5.1.3 Electronic and fluorescence properties of ZnPc+2 ($D2_h$) molecule

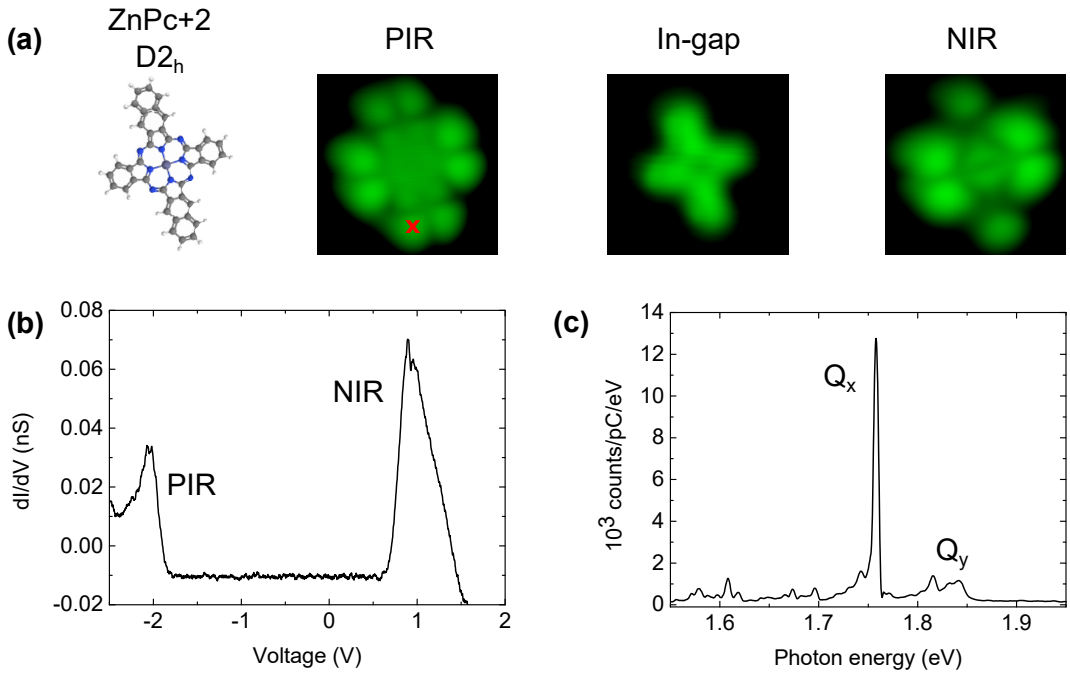

Figure 5.4: **Electronic and fluorescence properties of a single ZnPc+2 ($D2_h$) molecule. (a)** Ball-and-stick model of a ZnPc+2 ($D2_h$) molecule and 3×3 nm^2 STM PIR ($V = -2.5$ V), in-gap ($V = 0.5$ V) and NIR ($V = 0.9$ V) images recorded at $I = 10$ pA. **(b)** The $\frac{dI}{dV}$ spectrum of the molecule. **(c)** STML spectrum of the molecule recorded for $t = 120$ s with $I = 300$ pA and $V = -2.5$ V.

Fig.5.4 presents (a) the ball-and-stick model and STM images,(b) a $\frac{dI}{dV}$ spectrum and (c) a STML spectra of ZnPc+2 ($D2_h$) molecule. The light emission spectrum contains two emission peaks at 1.755 eV (lower excited state emission, labeled Q_x) and at 1.83 eV (higher excited state emission, labeled Q_y). The vibrations of this molecule are finely resolved and will be addressed in details further in the chapter.

5.1.4 Electronic and fluorescence properties of ZnPc+2 ($C2_v$) molecule

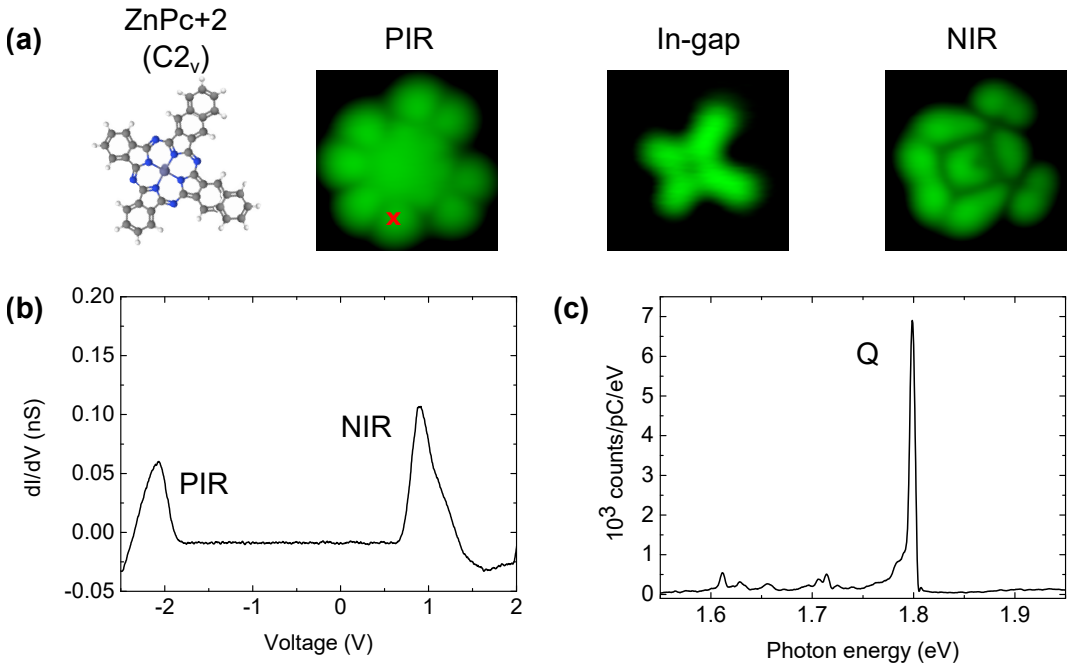

Figure 5.5: **Electronic and fluorescence properties of a single ZnPc+2 ($C2_v$) molecule. (a)** Ball-and-stick model of a ZnPc+2 ($D2_h$) molecule and 3×3 nm^2 STM PIR($V = -2.1$ V), in-gap ($V = 0.5$ V) and NIR ($V = 1.5$ V) images recorded at $I = 10$ pA. **(b)** $\frac{dI}{dV}$ spectrum of the molecule. **(c)** STML spectrum of the molecule recorded for $t = 180$ s with $I = 200$ pA and $V = -2.4$ V.

Fig.5.5 presents (a) the ball-and-stick model and STM images,(b) a $\frac{dI}{dV}$ spectrum and (c) a STML spectra of ZnPc+2 ($C2_v$) molecule. The light emission spectrum contains one main emission peak at 1.8 eV (labeled Q) and vibronic peaks at lower energy that will be discussed later in the chapter.

5.1.5 Electronic and fluorescence properties of ZnPc3 molecule

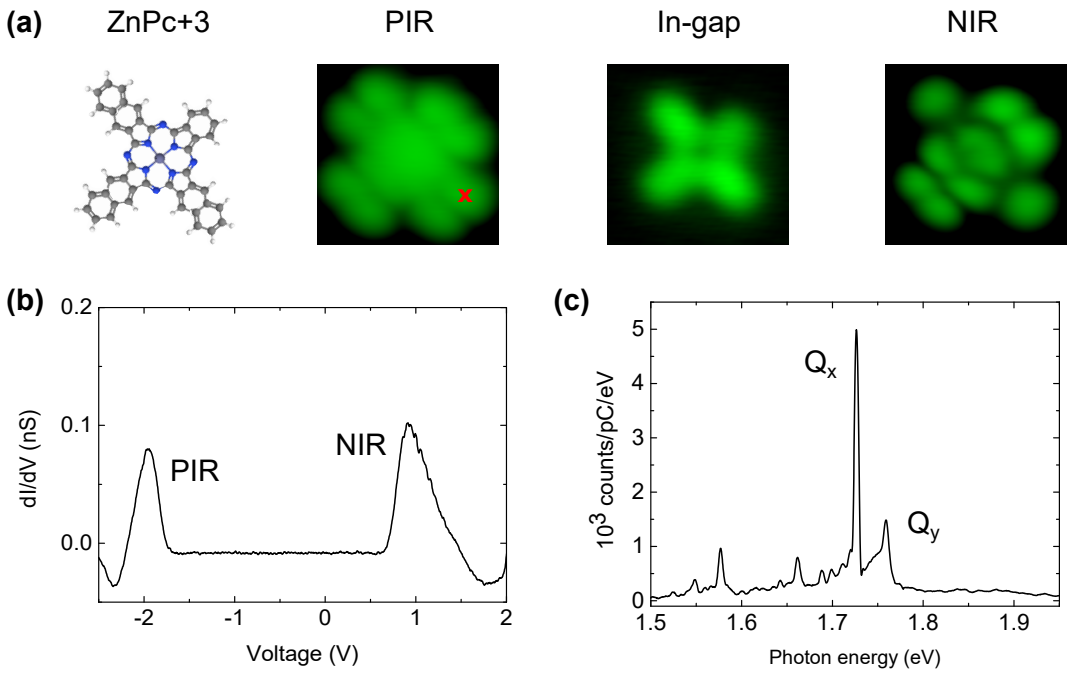

Figure 5.6: **Electronic and fluorescence properties of a single ZnPc+3 molecule.** **(a)** Ball-and-stick model of a ZnPc+3 molecule and 3×3 nm^2 STM PIR($V = -2.3$ V), in-gap ($V = 0.5$ V) and NIR ($V = 1.5$ V) images recorded at $I = 10$ pA. **(b)** $\frac{dI}{dV}$ spectrum of the molecule. **(c)** STML spectrum of the molecule recorded for $t = 180$ s with $I = 100$ pA and $V = -2.3$ V.

Fig.5.6 presents (a) the ball-and-stick model and STM images,(b) $\frac{dI}{dV}$ spectrum and (c) STML spectra of ZnPc+3 molecule. The light emission spectrum contains two main emission peaks, one at 1.725 eV (labeled Q_x) and one at 1.76 eV (labeled Q_y), and vibronic peaks at lower energy that will be discussed later in the chapter.

5.1.6 Electronic and fluorescence properties of ZnPc+4 (ZnNc) molecule

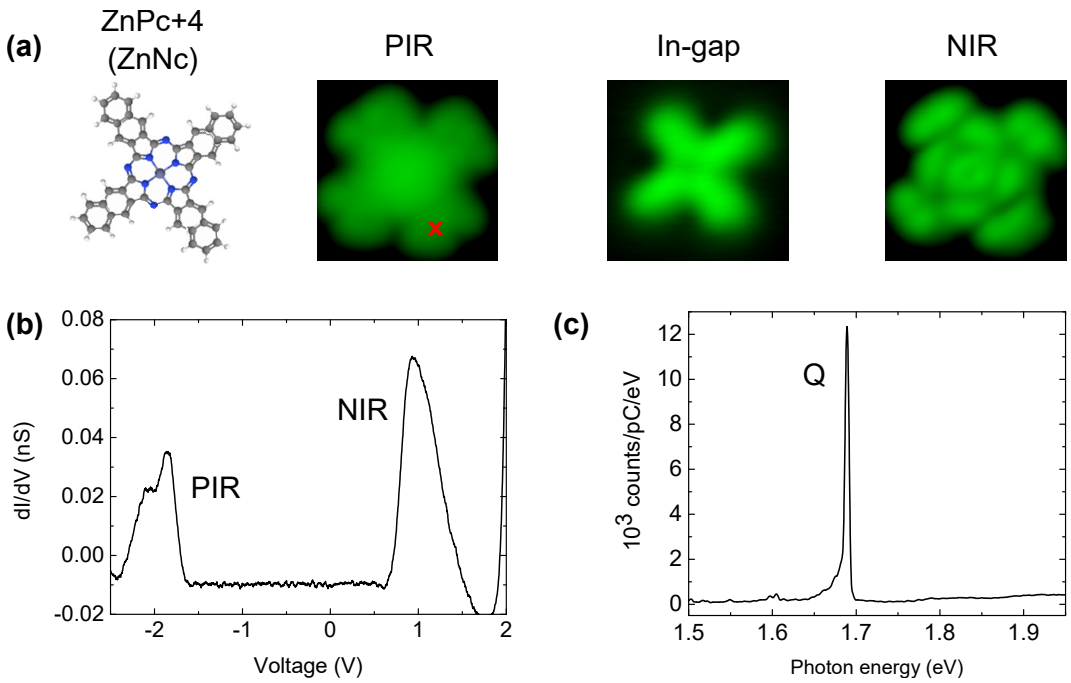

Figure 5.7: **Electronic and fluorescence properties of a single ZnPc+4 (ZnNc) molecule. (a)** Ball-and-stick model of a ZnPc+4 molecule and 3×3 nm^2 STM PIR($V = -2.5$ V), in-gap ($V = 0.5$ V) and NIR ($V = 0.9$ V) images recorded at $I = 10$ pA. **(b)** The $\frac{dI}{dV}$ spectrum of the molecule. **(c)** STML spectrum of the molecule recorded for $t = 120$ s with $I = 200$ pA and $V = -2.5$ V.

Fig.5.6 presents (a) the ball-and-stick model and the STM images,(b) $\frac{dI}{dV}$ spectrum and (c) STML spectra of ZnPc+4 (ZnNc) molecule. The resonant images are in agreement with the previously reported studies of naphthalocyanines [96]. The light emission spectrum contains one main emission peak at 1.68 eV (labeled Q) and vibronic peaks at lower energy that will be discussed later in the chapter.

5.2 Discussion

5.2.1 Comparison of the experimental results

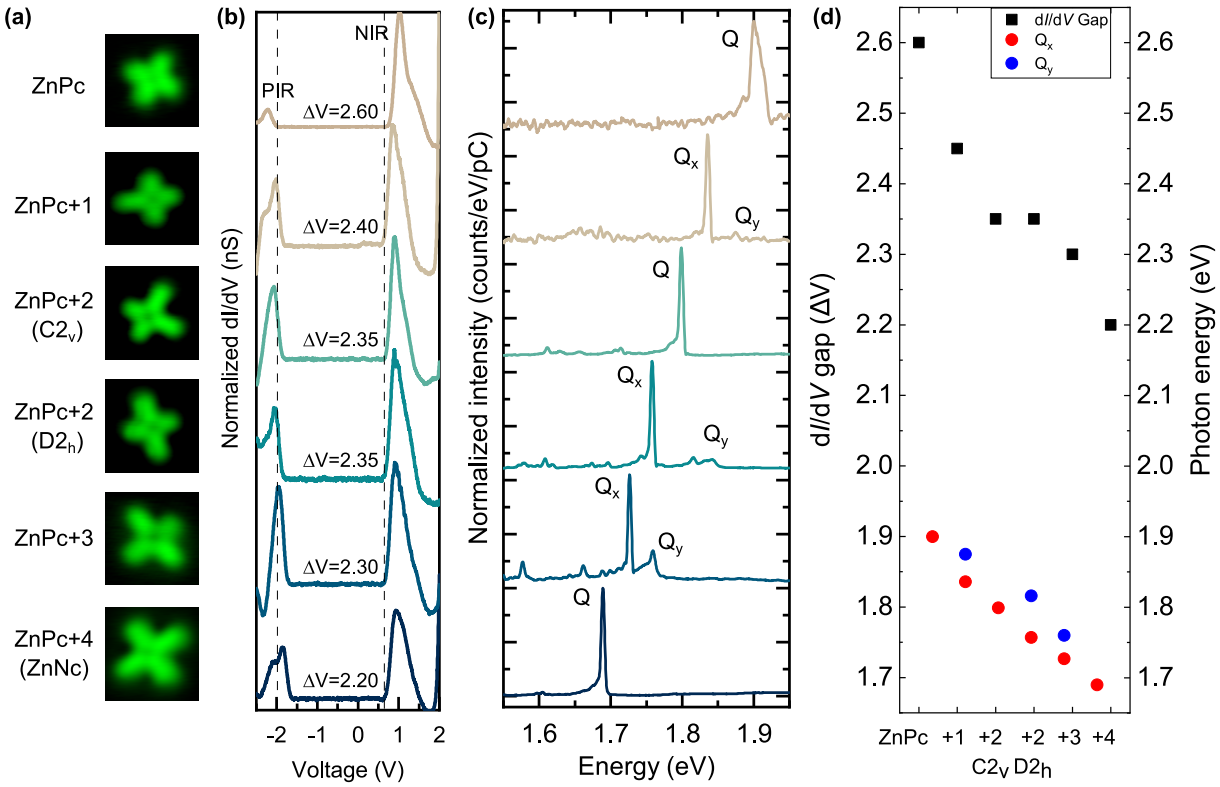

Figure 5.8: **Comparison of the results for the series of modified ZnPc molecules.** A side by side comparison of **(a)** in-gap topographical images of the studied molecules together with the corresponding **(b)** $\frac{dI}{dV}$ spectra and **(c)** STML spectra of each molecule. Dashed lines in (b) indicate the onsets of the PIR and the NIR of ZnPc. ΔV gives the size of electronic gap between the onsets. Labels Q_x and Q_y indicate the first and the second excited states, label Q indicates the degenerated excited state. **(d)** Electronic and optical gaps as a function of the size of the molecules.

In Fig.5.8 the comparison of the experimental results is given. The in-gap images of the studied molecules, shown in Fig.5.8(a), vividly demonstrate the appearance of additional benzene rings for each molecule. The dashed line in Fig.5.8(b) are aligned with onsets of PIR and NIR in the $\frac{dI}{dV}$ spectrum of ZnPc (top spectrum). One can see that, with each additional benzene ring, the gap between the resonances decreases (from ≈2.60 V for ZnPc to ≈2.20 V for ZnNc). The modification also changes the light emission energies. In Fig.5.8(c) a clear red shift can be observed, from 1.9 eV for ZnPc to 1.68 eV for ZnNc. In Fig.5.8(d) we plot the evolution of the $\frac{dI}{dV}$ gap and both Q_x and Q_y emission energies as a function of the studied molecule. One can see that the $\frac{dI}{dV}$ gap decreases faster than the optical gaps. The relationship between the emission energy and delocalization length of the electrons is here valid.

ZnPc+2 ($C2_v$) and ZnPc+2 ($D2_h$) display the same $\frac{dI}{dV}$ gap, which is expected con-

sidering that the delocalization length of the electrons is essentially the same. However, the optical gap of these molecules is different. That can be explained by the different dipoles of the molecules. Indeed, the energy of the ZnPc+2 ($C2_v$) main emission peak is located between the energies of the Q_x and the Q_y of ZnPc+2 ($D2_h$), as one may intuit from different size of the molecular axis of the ZnPc+2 ($D2_h$) molecule.

5.2.2 Appearance of Q_y lines

One important phenomenon that can be observed in Fig.5.8(c) is the appearance (for some of the molecules) of a second emission peak that is higher in energy than the main emission peak of the molecule. The two peaks are labeled as Q_x for the lower energy peak and Q_y for the higher energy peak. One can see that the Q_y peak appears only for the modified species where the two axis of the molecule are not equivalent, namely ZnPc+1, ZnPc+2 ($D2_h$) and ZnPc+3 (as can be deduced from in-gap images shown in Fig.5.8(a)). This "asymmetry" caused by the additional benzene rings induces a degeneracy lift of the excited states of the molecule. Since the degeneracy is lifted for the "asymmetric" molecules, the emission of both excited states is observed. For the in-depth discussion and comparison of the STML results, the molecules are divided in two groups based on the axis symmetry.

"Symmetric" molecules

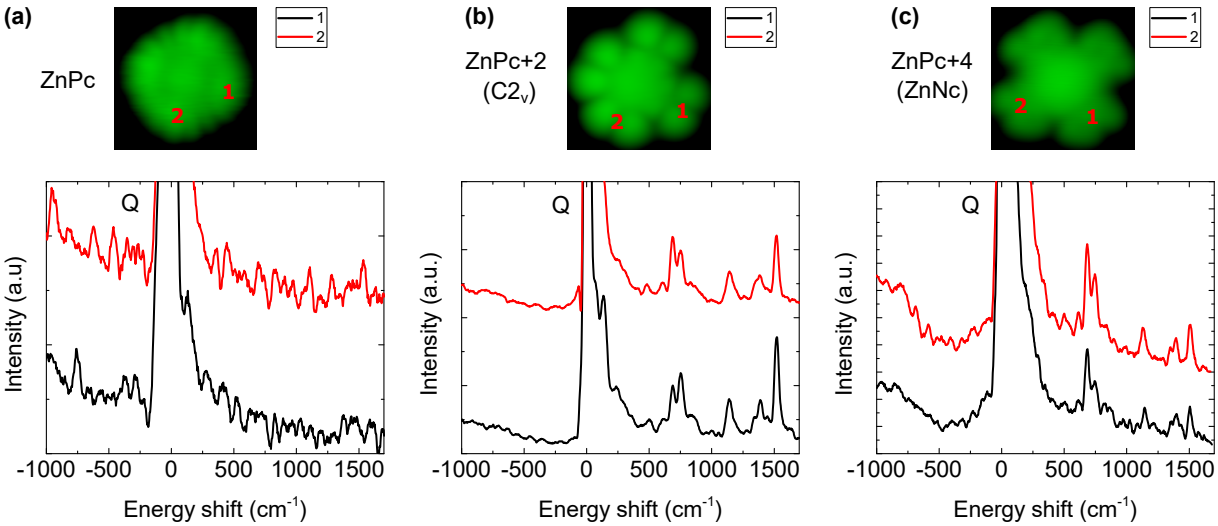

Figure 5.9: **Comparison of STML spectra of symmetric species.** STML spectra of the symmetric molecules recorded at two positions indicated by red numbers in the PIR images to the left. **(a)**STML spectra of ZnPc acquired for $t = 180$ s with $I = 200$ pA and $V = -2.4$ V. **(b)** STML spectra of ZnPc+2 ($C2_v$) acquired for $t = 180$ s with $I = 200$ pA and $V = -2.4$ V. **(c)** STML spectra of ZnPc+4 (ZnNc) acquired for $t = 120$ s with $I = 200$ pA and $V = -2.5$ V.

In Fig.5.9 magnified spectra of the "symmetric" (i.e. molecules which have equivalent

dipole axis) molecules are presented. Fig.5.9(a) shows two spectra of ZnPc acquired on the molecule at the two different positions marked with red numbers on PIR image. Fig.5.9(b) and (c) shows the two spectra of ZnPc+2 ($C2_v$) and ZnPc+4 (ZnNc) respectively. The STML data is magnified in order to achieve a better visualisation of the vibronic peaks. All the spectra are plotted in energy shift from the center of the 0-0 peak. One can see that the excitation of the molecule at two orthogonal axis results in the same STML spectra. The position of the vibronic peaks is equivalent for both axis and resembles the typical signature of phthalocyanine molecules [6].

"Asymmetric" molecules

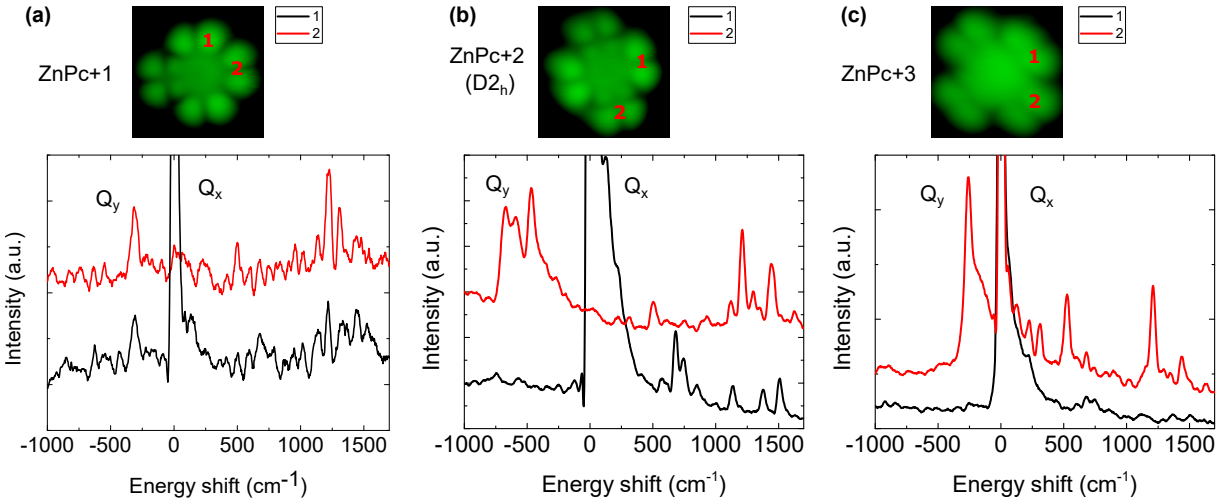

Figure 5.10: **Comparison of STML spectra of asymmetric species.** STML spectra of the symmetric molecules recorded at two positions indicated by red numbers in the PIR images to the left. **(a)**STML spectra of ZnPc+1 acquired for $t = 180$ s with $I = 200$ pA and $V = -2.4$ V. **(b)** STML spectra ofZnPc+2 ($D2_h$) acquired for $t = 120$ s with $I = 300$ pA and $V = -2.5$ V. **(c)** STML spectra of ZnPc+3 acquired for $t = 180$ s with $I = 100$ pA and $V = -2.3$ V.

In Fig.5.10 a magnified spectra of the asymmetric (where the axis are not equivalent) molecules are presented: (a) shows the two spectra of ZnPc+1, (b) shows the two spectra of ZnPc+2 ($D2_h$) and (c) shows the two spectra of ZnPc+3. In contrast with the "symmetric" molecules, one can see that excitation at the two orthogonal axis leads to the strong changes in the STML spectra. In particular, excitation on the "longer" axis results in the appearance of the higher energy peak Q_y and in the disappearance of Q_x.

The comparison of the STML spectra of the symmetric and the asymmetric molecules confirms the degeneracy lift of the excited states of the molecule due to changes of the symmetry of the two molecular axis.

Additionally, one can see that the vibronic spectra changes drastically depending on the excitation axis for the "asymmetric" molecules. As one can see from Fig.5.10(b), even though Q_x is not present in spectra 2 for the "asymmetric" molecules, the intense

vibronic peaks are observed between 1000→1500 cm^{-1}. Note that those peaks cannot be associated to the Q_y, as it would result into a too large $\sim 2000 cm^{-1}$ energy shift for those vibrations.

5.3 Vibrational spectroscopy of ZnPc+2 (D2h)

5.3.1 Hyper-resolved fluorescence map (HRFM) of ZnPc+2(D2h) molecule

To investigate the spatial dependency of the vibronic peaks of the "asymmetric" molecules, hyper-resolved fluorescence map (HRFM) [6] is recorded for ZnPc+2(D2h)/NaCl/Ag(111). Fig.5.11 presents 28×26 HRFM of ZnPc+2(D2h)/NaCl/Ag(111) recorded at constant

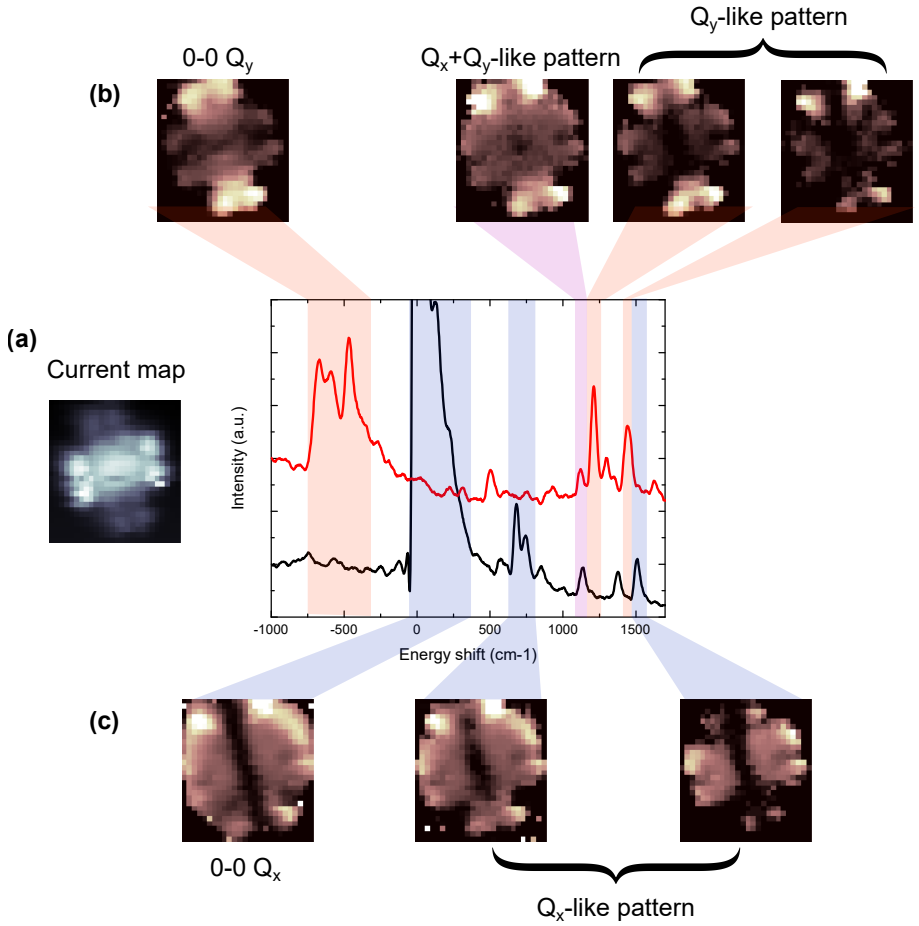

Figure 5.11: **Hyper-resolved fluorescence map of ZnPc+2(D2h) molecule. (a)** A 2.8×2.6 nm^2 current map of ZnPc+2(D2h)/NaCl/Ag(111) recorded at constant height (I = 1 nA, V = −2.5 V). The map is recorded simultaneously with STML acquisition over t = 60 s at each pixel of a 28×26 grid. The STML intensity was integrated within colored areas in the spectra for **(b)** Q_y peak and Q_y-induced vibrations (red area) and **(c)** Q_x peak and Q_x-induced vibrations (blue area). The integration over purple area around $1200 cm^{-1}$ demonstrates a $Q_x + Q_y$ map.

height with $I = 1$ nA and $V = -2.5$ V for $t = 60$ s per pixel. A higher number of pixels may provide a better resolution, however this would result into a very long measuring time (exceeds 12 hours for HRFM presented in Fig.5.11). The current map of the single ZnPc+2 ($D2_h$) molecule recorded at constant height regime is shown in Fig.5.11(a). Since the HRFM is recorded at constant height (to avoid distance-related effects), the current varies a lot during the acquisition. To compensate for these variations, the current map is recorded simultaneously and is used to normalize the resulting STML maps.

In Fig.5.11(b) and (c) HRFMs calculated in selected ranges corresponding to specific peaks in the STML spectra are shown. One can see that the normalized intensities of two main peaks, Q_x and Q_y, are spatially distributed in different fashions. Q_x is distributed at almost whole molecule. The normalized intensity is the highest at the edges of the molecule and gradually decreases towards the center of the molecule. These two halves of the molecules are separated by a node where the Q_x emission is absent. Q_y demonstrates a similar behaviour, but tilted by 90°. The highest STML intensity is at the termini of the longer molecular axis with a gradual decreases towards the center.

Investigation of several selected vibronic peaks returns very peculiar results. First, we focus on the STML spectra of ZnPc+2 ($D2_h$) acquired on the short axis (black spectrum in Fig.5.11). As an example, two vibronic peaks were chosen, the first and the last ones (blue area). STML maps of the two peaks shown in Fig.5.11(c) return a pattern that is similar the map of Q_x. Shifting the focus to the red spectra (acquired on the long axis of ZnPc+2 ($D2_h$)), the maps of the two most intense vibrations (red area) return a pattern similar to the HRFM of Q_y, with a high intensity at the long axis termini and absence of emission at the center.

Finally, HRFM of a vibration peak present in both spectra (purple area) is shown in Fig.5.11(b). The map is similar to the map of Q_x, however still conserves the intensity in the center of a long axis (behaviour attributed to Q_y).

5.3.2 Vibronic coupling of excited states

From the HRFM reported in the previous section, it is clear that a spatial variation of the two 0-0 peaks as well as of the corresponding vibrations is present, indicating that the excitation and emission of molecular dipoles are sensitive to the tip position. In order to understand the physical reason behind this sensitivity, the expression of the transition dipole moment should be derived [97, 98].

Schrodinger equation and total molecular hamiltonian

The derivation starts with a time-independent Schrodinger equation for molecular system

$$H(\mathbf{r_i}, \mathbf{Q_j})\Psi(\mathbf{r_i}, \mathbf{Q_j}) = E\Psi(\mathbf{r_i}, \mathbf{Q_j}),$$

where $\Psi(r_i, Q_j)$ is a vibronic wavefunction, E is an energy of a vibronic state, H is a total molecular hamiltonian, $\mathbf{r_i}$ and $\mathbf{Q_j}$ are collective coordinates of electrons and nuclei respectively.

A molecular state Ψ from Schrodinger equation is expressed as a tensorial product of an electronic state ϕ and a vibrational state χ. For a n-th vibrational state of an electronic ground state g the molecular state $\Psi_{g,n}$ is written as:

$$\Psi_{g,n}(\mathbf{r_i}, \mathbf{Q_j}) = \phi_g(\mathbf{r_i}, \mathbf{Q_j})\chi_n^g(\mathbf{Q_j})$$

The corresponding hamiltonian is given by

$$H(\mathbf{r_i}, \mathbf{Q_j}) = T_e(\mathbf{r_i}) + T_N(\mathbf{Q_j}) + U(\mathbf{r_i}, \mathbf{Q_j}) + V(\mathbf{Q_j}),$$

where the kinetic energies are given by

$$T_e(\mathbf{r_i}) = -\frac{\hbar^2}{2m} + \sum_i \nabla^2_{\mathbf{r_i}}$$

for electronic kinetic energy, and

$$T_N(\mathbf{Q_j}) = -\frac{\hbar^2}{2} + \sum_j \frac{1}{M_j}\nabla^2_{\mathbf{Q_j}}$$

for nuclear kinetic energy. The term $U(\mathbf{r_i}, \mathbf{Q_j})$ is the total Coulomb potential energy, including the interaction between the electrons and between the electrons and nuclei. The term $V(\mathbf{Q_j})$ is the potential energy of interactions between the nuclei.

Born-Oppenheimer approximation

At this point, the Born-Oppenheimer(BO) approximation is applied. BO approximation is the assumption that the wave functions of atomic nuclei and electrons in a molecule can be treated separately, based on the fact that the nuclei are much heavier than the electrons ($M \gg m$). Due to the larger relative mass of a nucleus compared to an electron, the coordinates of the nuclei in a system are approximated as fixed $\mathbf{Q_j^0}$, while the coordinates of the electrons are dynamic [97, 99, 100]:

$$H_{el}(\mathbf{r_i}, \mathbf{Q_j^0})\Psi(\mathbf{r_i}, \mathbf{Q_j^0}) = E\Psi(\mathbf{r_i}, \mathbf{Q_j^0}),$$

$$\Psi_{g,n}(\mathbf{r_i}, \mathbf{Q_j^0}) = \phi_g(\mathbf{r_i}, \mathbf{Q_j^0})\chi_n^g(\mathbf{Q_j^0})$$

Transition dipole moment

A transition dipole moment from the n-th state of the ground state g to m-th state of the excited state e is given by

$$M_{gn,em} = \langle \Psi_{g,n}(\{\mathbf{r_i}\}, \{\mathbf{Q_j^0}\}) | \hat{\mu} | \Psi_{e,m}(\{\mathbf{r_i}\}, \{\mathbf{Q_j^0}\}) \rangle,$$

where μ is the electric dipole-moment operator.

Franck–Condon (FC) principle states that, in the approximated system with fixed coordinates of nuclei, an electronic transition occurs without changes δQ_j in the positions of the nuclei. The intensity of a vibronic transition is then proportional to the square of the overlap integral between the vibrational wavefunctions of the states involved in the transition. The transition dipole moment in that case writes [101, 102]:

$$M_{gn,em} = \left[\langle \phi_g | \hat{\mu} | \phi_e \rangle_{\mathbf{r_i}} \right]_{\{\mathbf{Q_j^0}\}} \langle \chi_n^g | \chi_m^e \rangle_{\mathbf{Q_j}}$$

However, the vibrations of atoms in the molecule put the coordinate system out of equilibrium position. To the first order in the displacement of nuclei coordinates δQ_j from the equilibrium position $\{\mathbf{Q_j^0}\}$, one can shows that the molecular transition dipole moment is given by the Taylor series expansion of the electronic transition dipole moment in the nuclear coordinates $\mathbf{Q_j}$ (limited to the first two terms) [98]:

$$M_{gn,em} = \left[\langle \phi_g | \hat{\mu} | \phi_e \rangle_{\mathbf{r_i}} \right]_{\{\mathbf{Q_j^0}\}} \langle \chi_n^g | \chi_m^e \rangle_{\mathbf{Q_j}} + \sum_j \sum_h \left[\langle \phi_g | \hat{\mu} | \phi_h \rangle_{\mathbf{r_i}} \left\langle \phi_h \middle| \frac{\partial \phi_e}{\partial Q_j} \right\rangle_{\mathbf{r_i}} + \left\langle \frac{\partial \phi_g}{\partial Q_j} \middle| \phi_h \right\rangle_{\mathbf{r_i}} \langle \phi_h | \hat{\mu} | \phi_e \rangle_{\mathbf{r_i}} \right]_{\{\mathbf{Q_j^0}\}} \times \langle \chi_n^g | \delta \hat{Q}_j | \chi_m^e \rangle_{\mathbf{Q_j}}$$

The first term correspond to the Franck-Condon transition dipole moment (neglecting the terms linked to displacement δQ), while the second term is known as the Herzberg-Teller (HT) vibronic coupling term. This equation demonstrates that the dipole moment associated to a vibronic emission is described as a superposition of dipole moments associated to transitions from higher excited states of the molecule. In this case, the pattern observed in the Q_y HRFMs will be characteristic of this superposition, and thus will be different of the pattern observed for the Q_x.

5.3.3 Comparison with theoretical calculations

Fig.5.12 displays the comparison between experimentally recorded and theoretically calculated vibronic spectra. In Fig.5.12(a) the experimental spectrum (black) recorded on

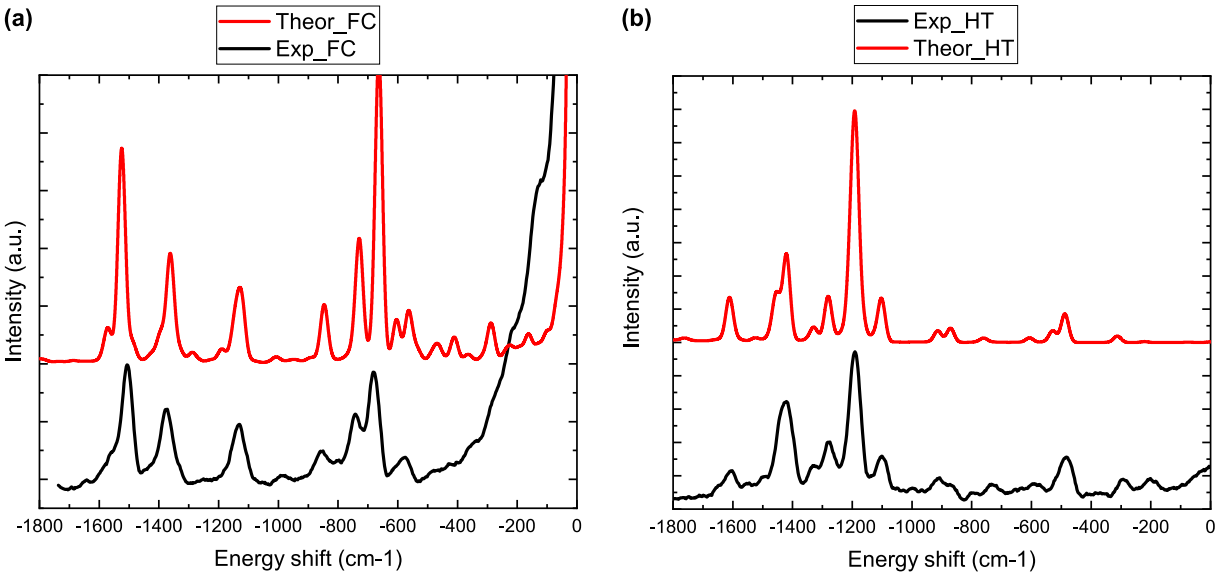

Figure 5.12: **Comparison of experimental and calculated vibronic spectra. (a)** Comparison of Franck-Condon (FC) contribution in vibronic fingerprint of ZnPc+2 ($D2_h$) acquired experimentally (black) and calculated theoretically (red). **(b)** Comparison of Herzberg-Teller (HT) contribution in vibronic fingerprint of ZnPc+2 ($D2_h$) acquired experimentally (black) and calculated theoretically (red).

a short molecular axis is compared with calculated vibronic transition intensities of only Franck-Condon term. Despite few differences in intensities (for example, the peak at -700 cm^{-1}), the STML spectra is in a great agreement with the calculated vibronic fingerprint. The agreement is even better for the comparison between the spectra recorded on a long axis of the molecule and the calculated vibronic transition intensities of only Herzberg-Teller contribution shown in Fig.5.12(b). This comparison demonstrates that, on the long axis, emission of Q_x is forbidden and vibronic emission can only come from the Herzberg-Teller contributions that "borrow" intensity to the Q_y (allowed) dipole, hence the resemblance of these vibronic maps with those of Q_y.

Conclusion

In this chapter, a STML study of a series of chemically modified ZnPc molecules is reported. The reference ZnPc molecule and every modification were studied for the electronic and fluorescence properties. The results demonstrate a $\frac{dI}{dV}$ gap reduction and a red shift of the STML peaks with the addition of benzene rings. In-depth STML investigation shown that breaking the symmetry of the molecular axis (hence, molecular dipoles) allows to lift the degeneracy of the excited states and enable independent Q_x and Q_y contributions. Due to the sub-nanometer precision of STML, it is possible to precisely select an emission dipole without contribution of another, demonstrating both Franck-Condon and Herzberg-Teller terms of vibrational emission. This claim is supported by recorded

HRFMs on ZnPc+2 ($D2_h$) molecule and confirmed by calculations of both FC and HT terms.

Conclusion and perspectives

The motivation at the heart of the present manuscript was to better understand the mechanisms underlying STML experiments. In order to do so, we need to go beyond simple model systems. For that, we relied on the ability of molecular chemistry to provide sets of molecules with systematic chemical modifications. To that end, we performed *in situ* and *ex situ* systematic minute changes of the structure of phthalocyanine molecules. This allows us to tune with precision their electronic and the optical properties.

In chapter 1 we presented the basic STM principles and the setup used in our experiments. In Chapter 2 we introduced the light generation and emission in an STM junction and discussed a single-molecule light emission generation and enhancement with the pico-cavity. The measures one need to take to sufficiently decouple molecules from samples and tips were presented and state-of-art excitation mechanism explanations were described.

In chapter 3 we reported a sequential *in situ* deprotonation of the central hydrogen atoms of a free-base phthalocyanine molecule H_2Pc thermally evaporated on NaCl/Ag(111) substrate. The reference model molecule H_2Pc as well as deprotonated species were studied for their electronic and optical properties. The investigation of the deprotonated species revealed systematic changes to tautomerization of the central hydrogens and position of the electronic gap of the molecule. The study of the excess charge localization demonstrates that deprotonation procedure lead to an excess electrons remaining in σ-orbital of the chromophore. The excess electrons remaining in the system generates a highly localized electric field which influences the emission energy observed in STML spectra of the molecules. The emission experiences a non-linear blue shift with each deprotonation, a phenomenon attributed only to the internal Stark effect from the electric field. This was confirmed with the help of theory collaborators who calculated the absorption energies of the deprotonated species. The influence of ISE on vibronic peaks was also discussed and confirmed with TD-DFT calculations.

Chapter 4 discussed the STML excitation mechanism of a single molecule. The motivation for this chapter comes from the unexplainable STML behaviour of HPc^- reported in chapter 3. An attempt to explain this behaviour within the framework of a state-of-art one-particle carrier injection mechanism revealed the discrepancy in the energy alignment and $\frac{dI}{dV}$ peaks interpretation. The example of HPc^- allowed us to report a many-body model of a single-molecule excitation that helps to understand the changes in the excitation and luminescence behaviour of the deprotonated molecules. Moreover, the model allowed to revisit different cases of the literature and reinterpret previously

puzzling luminescent features in the framework of different charged states of a molecule. Our many-body model allowed to reinterpret the reported literature cases of STML experiments on single ZnPc molecule on two different substrates (Au(111) and Ag(111)) and describe in details the excitation mechanism. Successful reinterpretation of the literature reports demonstrated that the proposed model can be readily applied to various STML experiments.

The final chapter reports on an STML study of a series of ZnPc subspecies which were chemically *ex situ* modified by systematic addition of benzene rings. The reference ZnPc molecule and every modification were studied for the electronic and fluorescence properties. The results of the $\frac{dI}{dV}$ spectrocopy experiments demonstrated the reduction of the electronic gap with addition of benzene rings. In-depth STML investigation demonstrated a red shift of the emission of the molecules, hence the shrinkage of the optical gap, with increase of number of the benzene rings. Based on the symmetry of the dipoles, the molecules were divided in two groups and the STML experiment results were compared in more details. This comparison confirmed that symmetry breaking of molecular axis (hence, molecular dipoles) induced by additional benzene rings allowed to lift the degeneracy of the excited states and enable independent Q_x and Q_y contributions. Due to a sub-nanometer precision of STM, it was possible to precisely excite a selected dipole without contribution of another in order to study the vibronic spectra in more detailed fashion. For that, a hyper-resolved fluorescence map (HRFM) was recorded on a single ZnPc ($D2_h$) molecule. The recorded spatial dependence of the vibrations was explained by the coupling of the excited states, which is confirmed by calculations of pure Franck-Condon and Herzberg-Teller contributions.

The results presented in the manuscript demonstrate the benefits of a systematic chemical control applied to model systems. In addition to highly interesting phenomena by itself, the results reported here had helped us to better understand the excitation mechanism of single molecules underlying the STML. However, there are still some experiments that can be performed even on the modified molecules reported here. For example, aligning two ZnPc+2 ($D2_h$) molecules in a dimer and couple different dipoles of the molecule will enhance the luminescence and may reveal new vibronic features. The proposed many-body representation could be further improved by accounting for molecular vibrations and substrate reorganisations and addressing the exact resonance positions in the molecular $\frac{dI}{dV}$ spectrum.

Bibliography

[1] G. Binnig et al., "Surface Studies by Scanning Tunneling Microscopy", *in*: *Physical Review Letters* 49.*1* (July 1982), pp. 57–61, DOI: 10.1103/physrevlett.49.57.

[2] X. H. Qiu, G. V. Nazin, and W. Ho, "Vibrationally Resolved Fluorescence Excited with Submolecular Precision", *in*: *Science* 299.*5606* (2003), pp. 542–546, DOI: 10.1126/science.1078675, eprint: http://www.sciencemag.org/content/299/5606/542.full.pdf, URL: http://www.sciencemag.org/content/299/5606/542.abstract.

[3] Z.-C. Dong et al., "Tunneling electron induced photon emission from monolayered H2TBP porphyrin molecules on Cu(100)", *in*: *Surface Science* 532-535 (June 2003), pp. 237–243, DOI: 10.1016/s0039-6028(03)00162-6.

[4] Michael C. Chong et al., "Narrow-Line Single-Molecule Transducer between Electronic Circuits and Surface Plasmons", *in*: *Phys. Rev. Lett.* 116 (3 Jan. 2016), p. 036802, DOI: 10.1103/PhysRevLett.116.036802, URL: http://link.aps.org/doi/10.1103/PhysRevLett.116.036802.

[5] Y Zhang et al., "Visualizing coherent intermolecular dipole-dipole coupling in real space", *in*: *Nature* 531 (2016), p. 623.

[6] Benjamin Doppagne et al., "Vibronic Spectroscopy with Submolecular Resolution from STM-Induced Electroluminescence", *in*: *Phys. Rev. Lett.* 118 (12 Mar. 2017), p. 127401, DOI: 10.1103/PhysRevLett.118.127401, URL: https://link.aps.org/doi/10.1103/PhysRevLett.118.127401.

[7] Hiroshi Imada et al., "Real-space investigation of energy transfer in heterogeneous molecular dimers", *in*: *Nature* 538 (2016), pp. 364–367.

[8] Shuiyan Cao et al., "Energy funneling within multi-chromophore architectures monitored with sub-nanometer resolution", *in*: *Nat. Chemistry* (2021), DOI: 10.1038/s41557-021-00697-z.

[9] Yang Luo et al., "Electrically Driven Single-Photon Superradiance from Molecular Chains in a Plasmonic Nanocavity", *in*: *Physical Review Letters* 122.*23* (June 2019), p. 233901, DOI: 10.1103/physrevlett.122.233901.

[10] Anna Roslawska et al., "Mapping Lamb, Stark and Purcell effects at a chromophore-picocavity junction with hyper-resolved fluorescence microscopy", *in*: *arXiv:2107.01072* (2021), arXiv: 2107.01072 [cond-mat.mes-hall].

[11] Benjamin Doppagne et al., "Electrofluorochromism at the single-molecule level", *in*: *Science* 361 (2018), p. 251.

[12] Jiří Doležal et al., "Exciton-Trion Conversion Dynamics in a Single Molecule", *in*: *ACS Nano* 15.*4* (2021), pp. 7694–7699, DOI: 10.1021/acsnano.1c01318.

[13] Song Jiang et al., *Many-body description of STM-induced fluorescence of charged molecules*, 2022, DOI: 10.48550/ARXIV.2210.00126.

[14] Kirill Vasilev et al., "Internal Stark effect of single-molecule fluorescence", *in*: *Nature Communications* 13.*1* (Feb. 2022), DOI: 10.1038/s41467-022-28241-8.

[15] J. Tersoff and D. R. Hamann, "Theory and Application for the Scanning Tunneling Microscope", *in*: *Physical Review Letters* 50.*25* (June 1983), pp. 1998–2001, DOI: 10.1103/physrevlett.50.1998.

[16] J. Tersoff and D. R. Hamann, "Theory of the scanning tunneling microscope", *in*: *Physical Review B* 31.*2* (Jan. 1985), pp. 805–813, DOI: 10.1103/physrevb.31.805.

[17] Jiutao Li, Wolf-Dieter Schneider, and Richard Berndt, "Local density of states from spectroscopic scanning-tunneling-microscope images: Ag(111)", *in*: *Physical Review B* 56.*12* (Sept. 1997), pp. 7656–7659, DOI: 10.1103/physrevb.56.7656.

[18] John Lambe and S. L. McCarthy, "Light Emission from Inelastic Electron Tunneling", *in*: *Physical Review Letters* 37.*14* (Oct. 1976), pp. 923–925, DOI: 10.1103/physrevlett.37.923.

[19] Anatoly V. Zayats, Igor I. Smolyaninov, and Alexei A. Maradudin, "Nano-optics of surface plasmon polaritons", *in*: *Physics Reports* 408.*3-4* (Mar. 2005), pp. 131–314, DOI: 10.1016/j.physrep.2004.11.001.

[20] Ludovic Douillard and Fabrice Charra, "High-resolution mapping of plasmonic modes: photoemission and scanning tunnelling luminescence microscopies", *in*: *Journal of Physics D: Applied Physics* 44.*46* (Nov. 2011), p. 464002, DOI: 10.1088/0022-3727/44/46/464002.

[21] Kensuke Kimura et al., "Selective triplet exciton formation in a single molecule", *in*: *Nature* 570.*7760* (June 2019), pp. 210–213, DOI: 10.1038/s41586-019-1284-2.

[22] Z. C. Dong et al., "Generation of molecular hot electroluminescence by resonant nanocavity plasmons", *in*: *Nature Phot.* 4 (2010), pp. 50–54.

[23] Natalia L. Schneider and Richard Berndt, "Plasmonic excitation of light emission and absorption by porphyrine molecules in a scanning tunneling microscope", *in*: *Phys. Rev. B* 86 (3 July 2012), p. 035445, DOI: 10.1103/PhysRevB.86.035445, URL: http://link.aps.org/doi/10.1103/PhysRevB.86.035445.

[24] Shadi Fatayer et al., "Reorganization energy upon charging a single molecule on an insulator measured by atomic force microscopy", *in*: *Nat. Nanotechnol.* 13.*5* (2018), pp. 376–380, DOI: 10.1038/s41565-018-0087-1, URL: https://doi.org/10.1038/s41565-018-0087-1.

[25] Laerte L. Patera et al., "Mapping orbital changes upon electron transfer with tunnelling microscopy on insulators", *in*: *Nature* 566.*7743* (2019), pp. 245–248, DOI: 10.1038/s41586-019-0910-3, URL: https://doi.org/10.1038/s41586-019-0910-3.

[26] Vibhuti Rai et al., "Boosting Light Emission from Single Hydrogen Phthalocyanine Molecules by Charging", *in*: *Nano Lett.* 20.*10* (2020), pp. 7600–7605, DOI: 10.1021/acs.nanolett.0c03121, eprint: https://doi.org/10.1021/acs.nanolett.0c03121, URL: https://doi.org/10.1021/acs.nanolett.0c03121.

[27] Gaël Reecht et al., "π-Radical Formation by Pyrrolic H Abstraction of Phthalocyanine Molecules on Molybdenum Disulfide", *in*: *ACS Nano* 13.*6* (2019), pp. 7031–7035, DOI: 10.1021/acsnano.9b02117, eprint: https://doi.org/10.1021/acsnano.9b02117, URL: https://doi.org/10.1021/acsnano.9b02117.

[28] David M. Bishop, "The vibrational Stark effect", *in*: *J. Chem. Phys.* 98.*4* (1993), pp. 3179–3184, DOI: 10.1063/1.464090, eprint: https://doi.org/10.1063/1.464090, URL: https://doi.org/10.1063/1.464090.

[29] Y. Zhang, "Sub-Nanometre Control of the Coherent Interaction between a Single Molecule and a Plasmonic Nanocavity", *in*: *Nature Commun.* 8.*15225* (2017), DOI: 10.1038/ncomms15225.

[30] Klaus Kuhnke et al., "Pentacene Excitons in Strong Electric Fields", *in*: *Chem. Phys. Chem.* 19.*3* (Dec. 2018), pp. 277–283, ISSN: 1439-4235, DOI: 10.1002/cphc.201701174.

[31] Ben Yang et al., "Sub-nanometre resolution in single-molecule photoluminescence imaging", *in*: *Nature Photonics* 14.*11* (Aug. 2020), pp. 693–699, DOI: 10.1038/s41566-020-0677-y.

[32] Hiroshi Imada et al., "Single-molecule laser nanospectroscopy with micro–electron volt energy resolution", *in*: *Science* 373.*6550* (2021), pp. 95–98, ISSN: 0036-8075, DOI: 10.1126/science.abg8790, URL: https://science.sciencemag.org/content/373/6550/95.

[33] Luis E. Parra López et al., *Tip-induced excitonic luminescence nanoscopy of an atomically-resolved van der Waals heterostructure*, 2022, DOI: 10.48550/ARXIV.2204.14022.

[34] Song Jiang et al., *Topologically localized excitons in single graphene nanoribbons*, 2022, DOI: 10.48550/ARXIV.2209.01471.

[35] G. Binnig et al., "7 × 7 Reconstruction on Si(111) Resolved in Real Space", *in*: *Physical Review Letters* 50.*2* (Jan. 1983), pp. 120–123, DOI: 10.1103/physrevlett.50.120.

[36] C. Julian Chen, *Introduction to Scanning Tunneling Microscopy*, Oxford University PressOxford, Sept. 2007, DOI: 10.1093/acprof:oso/9780199211500.001.0001.

[37] M Chelvayohan and C H B Mee, "Work function measurements on (110), (100) and (111) surfaces of silver", *in*: *Journal of Physics C: Solid State Physics* 15.*10* (Apr. 1982), pp. 2305–2312, DOI: 10.1088/0022-3719/15/10/029.

[38] J. Bardeen, "Tunnelling from a Many-Particle Point of View", *in*: *Physical Review Letters* 6.*2* (Jan. 1961), pp. 57–59, DOI: 10.1103/physrevlett.6.57.

[39] Vladimir A. Ukraintsev, "Data evaluation technique for electron-tunneling spectroscopy", *in*: *Physical Review B* 53.*16* (Apr. 1996), pp. 11176–11185, DOI: 10.1103/physrevb.53.11176.

[40] C. Julian Chen, "Tunneling matrix elements in three-dimensional space: The derivative rule and the sum rule", *in*: *Physical Review B* 42.*14* (Nov. 1990), pp. 8841–8857, DOI: 10.1103/physrevb.42.8841.

[41] C. Julian Chen, "Effects of m≠0 tip states in scanning tunneling microscopy: The explanations of corrugation reversal", *in*: *Physical Review Letters* 69.*11* (Sept. 1992), pp. 1656–1659, DOI: 10.1103/physrevlett.69.1656.

[42] Richard Berndt, "Photon Emission From the Scanning Tunneling Microscope", PhD thesis, University of Basel, 1992.

[43] Michael Chong, "Electrically driven fluorescence of single molecule junctions", PhD thesis, University of Strasbourg, 2016.

[44] I. Horcas et al., "WSXM: A software for scanning probe microscopy and a tool for nanotechnology", *in*: *Review of Scientific Instruments* 78.*1* (Jan. 2007), p. 013705, DOI: 10.1063/1.2432410.

[45] J. K. Gimzewski et al., "Photon emission with the scanning tunneling microscope", *in*: *Zeitschrift fur Physik B Condensed Matter* 72.*4* (Dec. 1988), pp. 497–501, DOI: 10.1007/bf01314531.

[46] Richard Berndt, James K. Gimzewski, and Peter Johansson, "Inelastic tunneling excitation of tip-induced plasmon modes on noble-metal surfaces", *in*: *Phys. Rev. Lett.* 67 (27 Dec. 1991), pp. 3796–3799, DOI: 10.1103/PhysRevLett.67.3796, URL: http://link.aps.org/doi/10.1103/PhysRevLett.67.3796.

[47] Kazuyuki Meguro et al., "Origin of multiple peaks in the light emission spectra of a Au(111) surface induced by the scanning tunneling microscope", *in*: *Phys. Rev. B* 65 (16 Apr. 2002), p. 165405, DOI: 10.1103/PhysRevB.65.165405, URL: http://link.aps.org/doi/10.1103/PhysRevB.65.165405.

[48] Heinz Raether, *Surface Plasmons on Smooth and Rough Surfaces and on Gratings*, Springer Berlin Heidelberg, 1988, DOI: 10.1007/bfb0048317.

[49] Frédéric Rossel, Marina Pivetta, and Wolf-Dieter Schneider, "Luminescence experiments on supported molecules with the scanning tunneling microscope", *in*: *Surface Science Reports* 65.*5* (May 2010), pp. 129–144, DOI: 10.1016/j.surfrep.2010.06.001.

[50] William L. Barnes, Alain Dereux, and Thomas W. Ebbesen, "Surface plasmon subwavelength optics", *in*: *Nature* 424.*6950* (Aug. 2003), pp. 824–830, DOI: 10.1038/nature01937.

[51] Katherine A. Willets and Richard P. Van Duyne, "Localized Surface Plasmon Resonance Spectroscopy and Sensing", *in*: *Annual Review of Physical Chemistry* 58.*1* (May 2007), pp. 267–297, DOI: 10.1146/annurev.physchem.58.032806.104607.

[52] E. Prodan et al., "A Hybridization Model for the Plasmon Response of Complex Nanostructures", *in*: *Science* 302.*5644* (Oct. 2003), pp. 419–422, DOI: 10.1126/science.1089171.

[53] San-E Zhu et al., "Self-Decoupled Porphyrin with a Tripodal Anchor for Molecular-Scale Electroluminescence", *in*: *J. Am. Chem. Soc.* 135.*42* (2013), pp. 15794–15800, DOI: 10.1021/ja4048569, eprint: http://dx.doi.org/10.1021/ja4048569, URL: http://dx.doi.org/10.1021/ja4048569.

[54] Kevin J. Savage et al., "Revealing the quantum regime in tunnelling plasmonics", *in*: *Nature* 491.*7425* (Nov. 2012), pp. 574–577, DOI: 10.1038/nature11653.

[55] M. Barbry et al., "Atomistic Near-Field Nanoplasmonics: Reaching Atomic-Scale Resolution in Nanooptics", *in*: *Nano Letters* 15.*5* (May 2015), pp. 3410–3419, DOI: 10.1021/acs.nanolett.5b00759.

[56] Felix Benz et al., "Single-molecule optomechanics in "picocavities"", *in*: *Science* 354.*6313* (Nov. 2016), pp. 726–729, DOI: 10.1126/science.aah5243.

[57] Benjamin Doppagne, "Hyper-Resolved Fluorescence Microscopy with STM", Theses, Université de Strasbourg, Feb. 2020, URL: https://tel.archives-ouvertes.fr/tel-03039417.

[58] R. Zhang et al., "Chemical mapping of a single molecule by plasmon-enhanced Raman scattering", *in*: *Nature* 498 (2013), p. 82.

[59] E. M. Purcell, H. C. Torrey, and R. V. Pound, "Resonance Absorption by Nuclear Magnetic Moments in a Solid", *in*: *Physical Review* 69.*1-2* (Jan. 1946), pp. 37–38, DOI: 10.1103/physrev.69.37.

[60] R. Berndt et al., "Photon Emission at Molecular Resolution Induced by a Scanning Tunneling Microscope", *in*: *Science* 262.*5138* (1993), pp. 1425–1427, DOI: 10.1126/science.262.5138.1425, eprint: http://www.sciencemag.org/content/262/5138/1425.full.pdf, URL: http://www.sciencemag.org/content/262/5138/1425.abstract.

[61] I.I. Smolyaninov, "Photon emission from a layer of copper phthalocyanine molecules on a gold (111) film surface induced by STM", *in*: *Surface Science* 364.*1* (Aug. 1996), pp. 79–88, DOI: 10.1016/0039-6028(96)00581-x.

[62] W. Deng et al., "STM-induced photon emission from self-assembled porphyrin molecules on a Cu(100) surface", *in*: *The Journal of Chemical Physics* 117.*10* (Sept. 2002), pp. 4995–5000, DOI: 10.1063/1.1498471.

[63] K. Sakamoto et al., "Light emission spectra of the monolayer-island of C60 molecules on Au(111) induced by scanning tunneling microscope", *in*: *Surface Science* 502-503 (Apr. 2002), pp. 149–155, DOI: 10.1016/s0039-6028(01)01924-0.

[64] Z.-C. Dong et al., "Vibrationally Resolved Fluorescence from Organic Molecules near Metal Surfaces in a Scanning Tunneling Microscope", *in*: *Phys. Rev. Lett.* 92 (8 Feb. 2004), p. 086801, DOI: 10.1103/PhysRevLett.92.086801, URL: http://link.aps.org/doi/10.1103/PhysRevLett.92.086801.

[65] Christoph Große et al., "Submolecular Electroluminescence Mapping of Organic Semiconductors", *in*: *ACS Nano* 11.*2* (Jan. 2017), pp. 1230–1237, DOI: 10.1021/acsnano.6b08471.

[66] P. Merino et al., "Exciton dynamics of C60-based single-photon emitters explored by Hanbury Brown–Twiss scanning tunnelling microscopy", *in*: *Nature Communications* 6.*1* (Sept. 2015), DOI: 10.1038/ncomms9461.

[67] Gaël Reecht et al., "Electroluminescence of a Polythiophene Molecular Wire Suspended between a Metallic Surface and the Tip of a Scanning Tunneling Microscope", *in*: *Physical Review Letters* 112.*4* (Jan. 2014), p. 047403, DOI: 10.1103/physrevlett.112.047403.

[68] Michael C. Chong et al., "Ordinary and Hot Electroluminescence from Single-Molecule Devices: Controlling the Emission Color by Chemical Engineering", *in*: *Nano Letters* 16.*10* (Sept. 2016), pp. 6480–6484, DOI: 10.1021/acs.nanolett.6b02997.

[69] S. W. Wu, G. V. Nazin, and W. Ho, "Intramolecular photon emission from a single molecule in a scanning tunneling microscope", *in*: *Phys. Rev. B* 77 (20 May 2008), p. 205430, DOI: 10.1103/PhysRevB.77.205430, URL: http://link.aps.org/doi/10.1103/PhysRevB.77.205430.

[70] Chi Chen et al., "Viewing the Interior of a Single Molecule: Vibronically Resolved Photon Imaging at Submolecular Resolution", *in*: *Physical Review Letters* 105.*21* (Nov. 2010), p. 217402, DOI: 10.1103/physrevlett.105.217402.

[71] Joonhee Lee et al., "Vibronic Motion with Joint Angstrom-Femtosecond Resolution Observed through Fano Progressions Recorded within One Molecule", *in*: *ACS Nano* 8.*1* (2014), pp. 54–63, DOI: 10.1021/nn405335h, eprint: http://dx.doi.org/10.1021/nn405335h, URL: http://dx.doi.org/10.1021/nn405335h.

[72] Vibhuti Rai et al., "Boosting Light Emission from Single Hydrogen Phthalocyanine Molecules by Charging", *in*: *Nano Lett.* 20.*10* (Sept. 2020), pp. 7600–7605, ISSN: 1530-6984, DOI: 10.1021/acs.nanolett.0c03121.

[73] Hiroshi Imada et al., "Single-Molecule Investigation of Energy Dynamics in a Coupled Plasmon-Exciton System", *in*: *Phys. Rev. Lett.* 119 (1 July 2017), p. 013901, DOI: 10.1103/PhysRevLett.119.013901, URL: https://link.aps.org/doi/10.1103/PhysRevLett.119.013901.

[74] Gong Chen et al., "Spin-Triplet-Mediated Up-Conversion and Crossover Behavior in Single-Molecule Electroluminescence", *in*: *Physical Review Letters* 122.*17* (May 2019), p. 177401, DOI: 10.1103/physrevlett.122.177401.

[75] Barry Honig et al., "An external point-charge model for wavelength regulation in visual pigments", *in*: *J. Am. Chem. Soc.* 101.*23* (1979), pp. 7084–7086, DOI: 10.1021/ja00517a060, eprint: https://doi.org/10.1021/ja00517a060, URL: https://doi.org/10.1021/ja00517a060.

[76] DS Gottfried, MA Steffen, and SG Boxer, "Large protein-induced dipoles for a symmetric carotenoid in a photosynthetic antenna complex", *in*: *Science* 251.*4994* (1991), pp. 662–665, ISSN: 0036-8075, DOI: 10.1126/science.1992518, eprint: https://science.sciencemag.org/content/251/4994/662.full.pdf, URL: https://science.sciencemag.org/content/251/4994/662.

[77] DJ Lockhart and PS Kim, "Internal stark effect measurement of the electric field at the amino terminus of an alpha helix", *in*: *Science* 257.*5072* (1992), pp. 947–951, ISSN: 0036-8075, DOI: 10.1126/science.1502559, eprint: https://science.sciencemag.org/content/257/5072/947.full.pdf, URL: https://science.sciencemag.org/content/257/5072/947.

[78] Mikhail Drobizhev et al., "Color Hues in Red Fluorescent Proteins Are Due to Internal Quadratic Stark Effect", *in*: *J. Phys. Chem. B* 113.*39* (2009), pp. 12860–12864, DOI: 10.1021/jp907085p, eprint: https://doi.org/10.1021/jp907085p, URL: https://doi.org/10.1021/jp907085p.

[79] Steven G. Boxer, "Stark Realities", *in*: *J. Phys. Chem. B* 113.*10* (2009), pp. 2972–2983, DOI: 10.1021/jp8067393, eprint: https://doi.org/10.1021/jp8067393, URL: https://doi.org/10.1021/jp8067393.

[80] Urs P. Wild et al., "Single molecule spectroscopy: Stark effect of pentacene in p-terphenyl", *in*: *Chem. Phys. Lett.* 193.*6* (1992), pp. 451–455, ISSN: 0009-2614, DOI: https://doi.org/10.1016/0009-2614(92)85830-4, URL: https://www.sciencedirect.com/science/article/pii/0009261492858304.

[81] M. Orrit et al., "Stark effect on single molecules in a polymer matrix", *in*: *Chem. Phys. Lett.* 196.*6* (1992), pp. 595–600, ISSN: 0009-2614, DOI: https://doi.org/10.1016/0009-2614(92)86000-8, URL: https://www.sciencedirect.com/science/article/pii/0009261492860008.

[82] L. Limot et al., "Surface-State Stark Shift in a Scanning Tunneling Microscope", *in*: *Phys. Rev. Lett.* 91 (19 Nov. 2003), p. 196801, DOI: 10.1103/PhysRevLett.91.196801, URL: https://link.aps.org/doi/10.1103/PhysRevLett.91.196801.

[83] I. Fernández-Torrente et al., "Gating the Charge State of Single Molecules by Local Electric Fields", *in*: *Phys. Rev. Lett.* 108 (3 Jan. 2012), p. 036801, DOI: 10.1103/PhysRevLett.108.036801, URL: https://link.aps.org/doi/10.1103/PhysRevLett.108.036801.

[84] Jesús Martínez-Blanco et al., "Gating a single-molecule transistor with individual atoms", *in*: *Nat. Phys.* 11.*8* (Aug. 2015), pp. 640–644, ISSN: 1745-2481, DOI: 10.1038/nphys3385, URL: https://doi.org/10.1038/nphys3385.

[85] H. Imada et al., "Orbital-selective single molecule excitation and spectroscopy based on plasmon-exciton coupling", *in*: *ArXiv e-prints* (Sept. 2016), arXiv: 1609.02701 [physics.chem-ph].

[86] Nicolas Néel et al., "Depopulation of Single-Phthalocyanine Molecular Orbitals upon Pyrrolic-Hydrogen Abstraction on Graphene", *in*: *ACS Nano* 10.*2* (2016), pp. 2010–2016, DOI: 10.1021/acsnano.5b06153, eprint: https://doi.org/10.1021/acsnano.5b06153, URL: https://doi.org/10.1021/acsnano.5b06153.

[87] Ingmar Swart, Tobias Sonnleitner, and Jascha Repp, "Charge State Control of Molecules Reveals Modification of the Tunneling Barrier with Intramolecular Contrast", *in*: *Nano Lett.* 11.*4* (2011), pp. 1580–1584, DOI: 10.1021/nl104452x, eprint: https://doi.org/10.1021/nl104452x, URL: https://doi.org/10.1021/nl104452x.

[88] Mohammad Gulam Rabbani and Junji Teraoka, "Resonance Raman spectra of N-deprotonated σ-type dianion of porphycenes", *in*: *Spectrochim. Acta A* 76.*2* (2010), pp. 207–212, ISSN: 1386-1425, DOI: https://doi.org/10.1016/j.saa.2010.03.020, URL: https://www.sciencedirect.com/science/article/pii/S1386142510001460.

[89] Aftab Farrukh et al., "Bias-polarity dependent electroluminescence from a single platinum phthalocyanine molecule", *in*: *Chin. J. Chem. Phys.* 34.*1* (2021), pp. 87–94, DOI: 10.1063/1674-0068/cjcp2007114.

[90] Jiří Doležal et al., "Mechano-Optical Switching of a Single Molecule with Doublet Emission", *in*: *ACS Nano* 14.*7* (2020), PMID: 32539338, pp. 8931–8938, DOI: 10.1021/acsnano.0c03730, eprint: https://doi.org/10.1021/acsnano.0c03730, URL: https://doi.org/10.1021/acsnano.0c03730.

[91] Fabian Schulz et al., "Many-body transitions in a single molecule visualized by scanning tunnelling microscopy", *in*: *Nature Physics* 11.*3* (Jan. 2015), pp. 229–234, DOI: 10.1038/nphys3212.

[92] Ping Yu et al., "Apparent Reversal of Molecular Orbitals Reveals Entanglement", *in*: *Physical Review Letters* 119.*5* (Aug. 2017), p. 056801, DOI: 10.1103/physrevlett.119.056801.

[93] Shadi Fatayer et al., "Probing Molecular Excited States by Atomic Force Microscopy", *in*: *Physical Review Letters* 126.*17* (Apr. 2021), p. 176801, DOI: 10.1103/physrevlett.126.176801.

[94] Daniel Hernangómez-Pérez et al., "Reorganization energy and polaronic effects of pentacene on NaCl films", *in*: *Physical Review B* 102.*11* (Sept. 2020), p. 115419, DOI: 10.1103/physrevb.102.115419.

[95] Jiří Doležal et al., "Charge Carrier Injection Electroluminescence with CO-Functionalized Tips on Single Molecular Emitters", *in*: *Nano Letters* 19.*12* (Nov. 2019), pp. 8605–8611, DOI: 10.1021/acs.nanolett.9b03180.

[96] Peter Liljeroth, Jascha Repp, and Gerhard Meyer, "Current-Induced Hydrogen Tautomerization and Conductance Switching of Naphthalocyanine Molecules", *in*: *Science* 317 (2007), p. 1203.

[97] M. Born and R. Oppenheimer, "Zur Quantentheorie der Molekeln", *in*: *Annalen der Physik* 389.*20* (1927), pp. 457–484, DOI: 10.1002/andp.19273892002.

[98] Gerhard Herzberg and Edward Teller, "Schwingungsstruktur der Elektronenübergänge bei mehratomigen Molekülen", *in*: *Zeitschrift für Physikalische Chemie* 21B (1933), pp. 410 –446.

[99] T. Azumi and K. Matsuzaki, “WHAT DOES THE TERM ”VIBRONIC COUPLING” MEAN?”, *in*: *Photochemistry and Photobiology* 25 (1977), p. 315.

[100] G. Fischer, *Vibronic Coupling: The Interaction Between the Electronic and Nuclear Motions*, Theoretical chemistry, Academic Press, 1984, ISBN: 9780122572401, URL: https://books.google.fr/books?id=Wk5oRdBIu30C.

[101] J. Franck and E. G. Dymond, “Elementary processes of photochemical reactions”, *in*: *Transactions of the Faraday Society* 21.*February* (1926), p. 536, DOI: 10.1039/tf9262100536.

[102] Edward U. Condon, “Nuclear Motions Associated with Electron Transitions in Diatomic Molecules”, *in*: *Physical Review* 32.*6* (Dec. 1928), pp. 858–872, DOI: 10.1103/physrev.32.858.

Kirill VASILEV

Chemical control of single-molecule fluorescence

Résumé

L'étude de l'influence de l'environnement sur les propriétés de fluorescence des molécules a été menée dans divers domaines de recherche, dont celui de la microscopie à effet tunnel (STM). Dans le présent manuscrit, le point de vue est déplacé de ces effets environnementaux extrinsèques vers les effets liés aux modifications internes de la molécule. Ainsi, les résultats présentés ici démontrent comment des changements infimes de la structure chimique d'une molécule peuvent affecter sa réponse photonique. Pour cela, deux schémas différents sont considérés :

La première approche consiste à modifier "in-situ" une seule molécule de phtalocyanine à base libre (H_2Pc). Ici, le cœur de la molécule est modifié en retirant successivement des protons individuels avec la pointe STM. Les électrons qui restent dans la molécule après cette procédure sont localisés dans des orbitales moléculaires de type sigma et génèrent un champ électrique qui affecte les propriétés de fluorescence de la molécule induites par le STM, un phénomène connu sous le nom d'effet Stark. Cet effet Stark "interne" génère un déplacement de la ligne de fluorescence qui suit une dépendance parabolique avec le nombre de charges restantes dans la molécule. Les lignes d'émission vibroniques connaissent également des décalages d'énergie qui sont bien reproduits par les calculs DFT, et qui mettent en évidence un effet Stark vibrationnel.

La deuxième approche expérimentale est menée sur une série de molécules de Zinc-phthalocyanine (ZnPc). Ici, des dérivés de ZnPc contenant un nombre croissant d'unités isoindole ont été simultanément évaporées sur nos substrats. L'étude de la luminescence induite par STM de ces différentes espèces montre des changements de fluorescence très particuliers et systématiques, tels que la levée de dégénérescence des états excités de la molécule et l'apparition/disparition d'états vibroniques spécifiques.

Mots clés : STM, STS, STML, chimie, molécules uniques, phtalocyanines, effet Stark, Herzberg-Teller , spectroscopie vibronique.

Résumé en anglais

The study of the influence of the environment on the fluorescence properties of molecules has been carried out in various fields of research, including scanning tunneling microscopy (STM). In the present manuscript, the focus is shifted from these extrinsic environmental effects to effects related to internal changes in the molecule. Thus, the results presented here demonstrate how minute changes in the chemical structure of a molecule can affect its photonic response. For this, two different schemes are considered:

The first approach consists in modifying "in-situ" a single free base phthalocyanine (H_2Pc) molecule. Here, the core of the molecule is modified by successively removing individual protons with the STM tip. The electrons remaining in the molecule after this procedure are localized in sigma-like molecular orbitals and generate an electric field that affects the STM-induced fluorescence properties of the molecule, a phenomenon known as the Stark effect. This "internal" Stark effect generates a shift in the fluorescence line that follows a parabolic dependence with the number of remaining charges in the molecule. The vibronic emission lines also experience energy shifts which are well reproduced by DFT calculations, and which highlight a vibrational Stark effect.

The second experimental approach is conducted on a series of Zinc-phthalocyanine molecules (ZnPc). Here, ZnPc derivatives containing an increasing number of isoindole units were simultaneously evaporated on our substrates. The study of the STM-induced luminescence of these different species shows very particular and systematic fluorescence changes, such as the lifting of degeneracy of excited states of the molecule and the appearance/disappearance of specific vibronic states.

Keywords: STM, STS, STML, chemistry, single molecules, phthalocyanines, Stark effect, Herzberg-Teller , vibronic spectroscopy.